

Industrial

Electronics

Biomedical

Civil

Aerospace

Computer

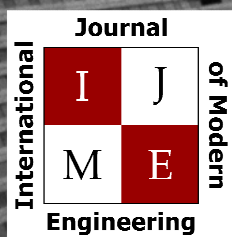
Electrical

Chemical

Mechanical



ENGINEERING



[www.ijme.us](http://www.ijme.us)

Print ISSN: 2157-8052  
Online ISSN: 1930-6628



[www.iajc.org](http://www.iajc.org)

## INTERNATIONAL JOURNAL OF MODERN ENGINEERING

### ABOUT IJME:

- IJME was established in 2000 and is the first and official flagship journal of the International Association of Journal and Conferences (IAJC).
- IJME is a high-quality, independent journal steered by a distinguished board of directors and supported by an international review board representing many well-known universities, colleges and corporations in the U.S. and abroad.
- IJME has an impact factor of **3.00**, placing it among the top 100 engineering journals worldwide, and is the #1 visited engineering journal website (according to the National Science Digital Library).

### OTHER IAJC JOURNALS:

- The International Journal of Engineering Research and Innovation (IJERI)  
For more information visit [www.ijeri.org](http://www.ijeri.org)
- The Technology Interface International Journal (TIIJ).  
For more information visit [www.tiij.org](http://www.tiij.org)

### IJME SUBMISSIONS:

- Manuscripts should be sent electronically to the manuscript editor, Dr. Philip Weinsier, at [philipw@bgsu.edu](mailto:philipw@bgsu.edu).

For submission guidelines visit  
[www.ijme.us/submissions](http://www.ijme.us/submissions)

### TO JOIN THE REVIEW BOARD:

- Contact the chair of the International Review Board, Dr. Philip Weinsier, at [philipw@bgsu.edu](mailto:philipw@bgsu.edu).

For more information visit  
[www.ijme.us/ijme\\_editorial.htm](http://www.ijme.us/ijme_editorial.htm)

### INDEXING ORGANIZATIONS:

- IJME is currently indexed by 22 agencies.  
For a complete listing, please visit us at [www.ijme.us](http://www.ijme.us).

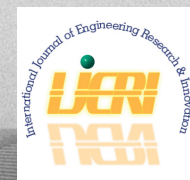
### Contact us:

**Mark Rajai, Ph.D.**

Editor-in-Chief  
California State University-Northridge  
College of Engineering and Computer Science  
Room: JD 4510  
Northridge, CA 91330  
Office: (818) 677-5003  
Email: [mrajai@csun.edu](mailto:mrajai@csun.edu)



[www.tiij.org](http://www.tiij.org)



[www.ijeri.org](http://www.ijeri.org)

---

# INTERNATIONAL JOURNAL OF MODERN ENGINEERING

The INTERNATIONAL JOURNAL OF MODERN ENGINEERING (IJME) is an independent, not-for-profit publication, which aims to provide the engineering community with a resource and forum for scholarly expression and reflection.

IJME is published twice annually (fall and spring issues) and includes peer-reviewed articles, book and software reviews, editorials, and commentary that contribute to our understanding of the issues, problems, and research associated with engineering and related fields. The journal encourages the submission of manuscripts from private, public, and academic sectors. The views expressed are those of the authors and do not necessarily reflect the opinions of the IJME editors.

## EDITORIAL OFFICE:

Mark Rajai, Ph.D.  
Editor-in-Chief  
Office: (818) 677-2167  
Email: [ijmeeditor@iajc.org](mailto:ijmeeditor@iajc.org)  
Dept. of Manufacturing Systems  
Engineering & Management  
California State University-  
Northridge  
18111 Nordhoff Street  
Northridge, CA 91330-8332

## THE INTERNATIONAL JOURNAL OF MODERN ENGINEERING EDITORS

*Editor-in-Chief*

**Mark Rajai**

California State University-Northridge

*Production Editor*

**Philip Weinsier**

Bowling Green State University-Firelands

*Manuscript Editor*

**Philip Weinsier**

Bowling Green State University-Firelands

*Subscription Editor*

**Morteza Sadat-Hossieny**

Northem Kentucky University

*Executive Editor*

**Sangram Redkar**

Arizona State University

*Publisher*

**Bowling Green State University-Firelands**

*Technical Editors*

**Andrea Ofori-Boadu**

North Carolina A&T State University

**Michelle Brodke**

Bowling Green State University-Firelands

**Marilyn Dyrud**

Oregon Institute of Technology

**Mandar Khanal**

Boise State University

**Chris Kluse**

Bowling Green State University

**Zhaochao Li**

Morehead State University

*Web Administrator*

**Saeed Namyar**

Advanced Information Systems

---

# TABLE OF CONTENTS

<i>Editor's Note: Registration is open for the 8<sup>th</sup> IAJC international conference in Orlando, Florida</i> .....	3
Philip Weinsier, IJME Manuscript Editor	
<i>Development of Ground Station Software for the Cosmic X-Ray Background Nanosat-2</i> .....	5
Marc Beck, Murray State University; Charles Conner, Capitol Technology University; Benjamin Malphrus, Morehead State University	
<i>Proof of Concept: Design Parameters for a Nanoscale Interdigitated Electrode Sensor for COVID-19 Detection</i> .....	15
Mohammed Abdallah, State University of New York Poly	
<i>Characterization of Electrical Waveforms in Transcutaneous Electrical Nerve Stimulators for Personal Use</i> .....	23
Albert Lozano-Nieto, The Pennsylvania State University, Wilkes-Barre	
<i>Steel Truss Design Optimization for Weight Minimization using a Multiple Linear Regression Data Fit</i> .....	31
Michael C. Pickett, Facilities Explosive Safety Mandatory Center of Expertise, AL; Stephen Cotton, Tumkey Processing Solutions, TN	
<i>Shear Lag in Diagrid Tall Buildings</i> .....	40
Mohammad T Bhuiyan, West Virginia State University	
<i>Instructions for Authors: Manuscript Formatting Requirements</i> .....	51



# 8<sup>TH</sup> IAJC INTERNATIONAL CONFERENCE

[www.2022.iajc.org](http://www.2022.iajc.org)

OCTOBER 13-16, 2022 – ORLANDO, FLORIDA

The leading indexed high-impact-factor conference on engineering and related technologies.

## Our Hotel—Embassy Suites



## Our Previous Tour—NASA's Kennedy Space Center



### CALL FOR CONFERENCE PROPOSALS

Conference Submission Deadlines:

- Abstract and Poster Submissions July 31, 2022
- Full-Paper Submissions (optional) July 31, 2022

Full papers may be submitted after a related abstract has been accepted for presentation. All full papers will automatically be reviewed for publication in the conference proceedings and the high-impact-factor IAJC journals after the conference. All submissions must be made using our online system at <https://2022.iajc.org/registration>

Have questions or need help? Contact Philip Weinsier (Conference General Chair) at [philipw@bgsu.edu](mailto:philipw@bgsu.edu)

## Editorial Review Board Members

Mohammed Abdallah	State University of New York (NY)	Rungun Nathan	Penn State Berks (PA)
Paul Akangah	North Carolina A&T State University (NC)	Arun Nambiar	California State University Fresno (CA)
Shah Alam	Texas A&M University-Kingsville (TX)	Aurenice Oliveira	Michigan Tech (MI)
Nasser Alaraje	Michigan Tech (MI)	Troy Ollison	University of Central Missouri (MO)
Ali Alavizadeh	Purdue University Northwest (IN)	Reynaldo Pablo	Purdue Fort Wayne (IN)
Lawal Anka	Zamfara AC Development (NIGERIA)	Basile Panoutsopoulos	Community College of Rhode Island (RI)
Jahangir Ansari	Virginia State University (VA)	Shahera Patel	Sardar Patel University (INDIA)
Sanjay Bagali	Acharya Institute of Technology (INDIA)	Thongchai Phairoh	Virginia State University (VA)
Kevin Berisso	Memphis University (TN)	Huyu Qu	Broadcom Corporation
Sylvia Bhattacharya	Kennesaw State University (GA)	Desire Rasolomampionona	Warsaw University of Tech (POLAND)
Monique Bracken	University of Arkansas Fort Smith (AR)	Michael Reynolds	University of West Florida (FL)
Tamer Breakah	Ball State University (IN)	Nina Robson	California State University-Fullerton (CA)
Michelle Brodke	Bowling Green State University (OH)	Marla Rogers	Fastboot Mobile, LLC
Shaobiao Cai	Minnesota State University (MN)	Dale Rowe	Brigham Young University (UT)
Rajab Challoo	Texas A&M University Kingsville (TX)	Karen Ruggles	DeSales University (PA)
Isaac Chang	Illinois State University (IL)	Anca Sala	Baker College (MI)
Shu-Hui (Susan) Chang	Iowa State University (IA)	Alex Sergeev	Michigan Technological University (MI)
Rigoberto Chinchilla	Eastern Illinois University (IL)	Mehdi Shabaninejad	Zagros Oil and Gas Company (IRAN)
Phil Cochrane	Indiana State University (IN)	Hiral Shah	St. Cloud State University (MN)
Curtis Cohenour	Ohio University (OH)	Mojtaba Shivaie	Shahrood University of Technology (IRAN)
Emily Crawford	Claffin University (SC)	Musibau Shofluwe	North Carolina A&T State University (NC)
Dongyang (Sunny)Deng	North Carolina A&T State University (NC)	Jiahui Song	Wentworth Institute of Technology (MA)
Z.T. Deng	Alabama A&M University (AL)	Carl Spezia	Southern Illinois University (IL)
Sagar Deshpande	Ferris State University (MI)	Michelle Surerus	Ohio University (OH)
Marilyn Dyrud	Oregon Institute of Technology (OR)	Harold Terano	Camarines Sur Polytechnic (PHILIPPINES)
Mehran Elahi	Elizabeth City State University (NC)	Sanjay Tewari	Missouri University of Science & Tech (MO)
Ahmed Elsayy	Tennessee Technological University (TN)	Vassilios Tzouanas	University of Houston Downtown (TX)
Cindy English	Millersville University (PA)	Jeff Ulmer	University of Central Missouri (MO)
Ignatius Fomunung	University of Tennessee Chattanooga (TN)	Abraham Walton	University of South Florida Polytechnic (FL)
Ahmed Gawad	Zagazig University EGYPT)	Haoyu Wang	Central Connecticut State University (CT)
Hamed Guendouz	Yahia Fares University (ALGERIA)	Jyhwen Wang	Texas A&M University (TX)
Kevin Hall	Western Illinois University (IL)	Boonsap Witchayangkoon	Thammasat University (THAILAND)
Mohsen Hamidi	Utah Valley University (UT)	Shuju Wu	Central Connecticut State University (CT)
Mamoon Hammad	Abu Dhabi University (UAE)	Baijian "Justin" Yang	Purdue University (IN)
Gene Harding	Purdue Polytechnic (IN)	Xiaoli (Lucy) Yang	Purdue University Northwest (IN)
Bernd Haupt	Penn State University (PA)	Hao Yi	Chongqing University (CHINA)
Yousef Himri	Safety Engineer in Sonelgaz (ALGERIA)	Faruk Yildiz	Sam Houston State University (TX)
Delowar Hossain	City University of New York (NY)	Yuqiu You	Ohio University (OH)
Xiaobing Hou	Central Connecticut State University (CT)	Hong Yu	Fitchburg State University (MA)
Shelton Houston	University of Louisiana Lafayette (LA)	Pao-Chiang Yuan	Jackson State University (MS)
Ying Huang	North Dakota State University (ND)	Jinwen Zhu	Missouri Western State University (MO)
Christian Bock-Hyeng	North Carolina A&T University (NC)		
Pete Hylton	Indiana University Purdue (IN)		
John Irwin	Michigan Tech (MI)		
Toqeer Israr	Eastern Illinois University (IL)		
Alex Johnson	Millersville University (PA)		
Rex Kanu	Purdue Polytechnic (IN)		
Reza Karim	North Dakota State University (ND)		
Manish Kewalramani	Abu Dhabi University (UAE)		
Tae-Hoon Kim	Purdue University Northwest (IN)		
Chris Kluse	Bowling Green State University (OH)		
Doug Koch	Southeast Missouri State University (MO)		
Mohan Krishna	Vidyavardhaka College of Eng. (INDIA)		
Resmi Krishnankuttyrema	Bowling Green State University (OH)		
Zaki Kuruppallil	Ohio University (OH)		
Shiyoung Lee	Penn State University Berks (PA)		
Soo-Yen (Samson) Lee	Central Michigan University (MI)		
Chao Li	Florida A&M University (FL)		
Jiliang Li	Purdue University Northwest (IN)		
Zhaochao Li	Morehead State University (KY)		
Dale Litwhiler	Penn State University (PA)		
Lozano-Nieto	Penn State University (PA)		
Mani Manivannan	ARUP Corporation		
G.H. Massiha	University of Louisiana (LA)		
Thomas McDonald	University of Southern Indiana (IN)		
David Melton	Eastern Illinois University (IL)		
Shokoufeh Mirzaei	Cal State Poly Pomona (CA)		
Kay Rand Morgan	Mississippi State University (MS)		
Sam Mryyan	Excelsior College (NY)		
Jessica Murphy	Jackson State University (MS)		

# DEVELOPMENT OF GROUND STATION SOFTWARE FOR THE COSMIC X-RAY BACKGROUND NANOSAT-2

Marc Beck, Murray State University; Charles Conner, Capitol Technology University; Benjamin Malphrus, Morehead State University

## Abstract

The development and deployment of increasing numbers of CubeSats, an affordable type of small satellite, has presented several technical issues for the users of these systems. The most important of these is the need for command, control, and data-handling software that allows the user on the ground to remotely control the satellite while it is in orbit. At this time, little or no software is commercially available for this purpose, primarily due to the fast-evolving nature of the field as well as the specific and often unique requirements of each mission. In order to increase mission efficiency and reduce development time and costs, the need for a general software framework that can be easily adapted for specific missions has arisen.

In this paper, the authors describe the development of a robust ground-station software (GSSW) package designed to communicate with the Cosmic X-ray Background (CXBN) series of spacecraft. The purpose of this software was threefold: 1) to process and display the scientific data gathered by the sensor system on-board the satellite; 2) to allow satellite system status to be determined and displayed; and, 3) to control the satellite via commands sent by the ground control operator to the spacecraft. Part of the GSSW is a graphical user interface (GUI) that displays data received from the satellite. The mission of CXBN-2 was to perform a high-precision measurement of the cosmic X-ray background radiation. This development was part of a general ground station methodology that would incorporate data flow analysis and illustrate a software approach that is general enough while, at the same time, applicable across a broad spectrum of CubeSat mission requirements.

## Introduction

The design and development of a ground-station software (GSSW) system for use with the cosmic x-ray background nanosat-2 (CXBN-2). CXBN-2 was a follow-up mission to CXBN-1 with the goal of collecting more-precise data. CXBN-1 was part of the Educational Launch of Nanosatellites (ELaNa) initiative in 2012. The CXBN-2 satellite was designed at Morehead State University and built in the Spacecraft Integration and Assembly Facility located inside the Space Science Center (SSC). The SSC is part of the Department of Earth and Space Sciences at Morehead State University. The Satellite was launched by NASA in April of 2017. The development of the GSSW was a collaborative effort between Morehead State University and Murray State University, which have both collaborated in the past on another CubeSat mission, KySat-1.

The parties involved in this project were the Department of Earth and Space Sciences at Morehead State University, which designed, built, and operated the CXBN satellite series, and the Department of Computer Science and Information Systems at Murray State University, which developed the ground station software. Further, the CXBN-3 mission was in the hardware-development phase and would use this same GSSW package. CXBN-2 is a nanosatellite built in the 2-unit (2U) CubeSat form factor that uses a high-performance, commercial X-ray detector array characterized and adapted for this mission. The purpose of the mission was to perform a precise measurement of the cosmic (diffuse) X-ray background in the 20-50 kilo electron volt (keV) range across broad swathes of the sky.

GSSW for satellite missions has to perform three crucial tasks. The first is command and control, which is the ability to send commands to the satellite and to control its subsystems remotely from the ground while the satellite is on orbit. The commands can range from prompting the satellite to transmit data over changing settings to switching individual subsystems of the satellite on or off, to uploading complex sequences of commands. Another important task is health and recovery, which involves monitoring the status of the satellite and ensuring that all of its subsystems are functioning within normal mission parameters, and to perform corrective actions if one or more systems fail.

Satellite health data to be monitored usually consists of telemetry data and includes battery status, temperatures, and subsystem status. Examples for corrective actions that can be taken in order to recover from a fault may include rebooting the satellite's onboard computer or switching to a redundant system. The last task is data handling, which includes processing, display, and archiving of the payload scientific data that are transmitted back to the ground station by the satellite (Zetocha & Brito, 2001).

The GSSW was designed using best practices in a modular, top-down fashion that would allow re-use of general-purpose GUIs and file handling, while also permitting customization based on specific mission requirements. It was written to run on several ground stations, including one located in Morehead, using a 21-meter, full-motion antenna operating on UHF, S-band, and X-bands (Malphrus, Kruth, Combs, Fite, Twiggs, & Schulze, 2010). An additional potential use is the amateur radio community for installation on amateur radio stations that perform similar command-and-control functions on amateur radio satellite systems (Garg, Kand, Pradhan, & Agarwal, 2019).

## Background and Motivation

Murray State University and Morehead State University are both four-year public universities located in western and eastern Kentucky, respectively. The Space Science Center (SSC) at Morehead State University has as a primary mission the design, development, and construction of small satellites in the CubeSat class. These include KySat-1, KySat-2, CXBN-1, CXBN-2, UniSat 5, and Lunar IceCube over the course of the past decade (Malphrus et al., 2012). CubeSat projects were initially designed in order to meet the growing demand for workers and researchers in the science, technology, engineering, and mathematics (STEM) fields. Many universities in recent years have used this vehicle as a way of involving students in interesting, exciting projects. These CubeSat projects were aimed at generating interest among the students and preparing them for careers in the aerospace workplace, among others (Darbali-Zamora, Ortiz-Rivera, & Rincon-Charris, 2015). At the same time, the increasing success of the CubeSat platform (Puig-Suari, Tumer, & Twiggs, 2001) as a new, small-satellite standard has made access to space increasingly more affordable for universities and others, due to the decreased mission and launch costs (Deepak & Twiggs, 2012).

To exploit this revolutionary opportunity, a consortium within the State of Kentucky, known as KentuckySpace (KySpace) consortium was formed circa 2006. The main goal was to foster collaboration between a group of five universities on satellite development projects. These five universities were the University of Kentucky, the University of Louisville, Morehead State University, Murray State University, and Western Kentucky University. KySpace was responsible for the design, development, and deployment of KySat-1 (launched in 2011) and KySat-2 (launched in 2013). Since the launch of KySat-2, there have been many changes to the KySpace consortium. Morehead State has become a leader in CubeSat development, while most of the other institutions have pursued different interests. KySpace has spun off a for-profit company, Space Tango LLC, and maintains KySpace as a non-profit, research-and-development organization. This project represented a continuation of the earlier collaborative efforts between two of the original KySpace member universities, Murray and Morehead State.

Morehead State University continued to look for original science opportunities that could utilize the CubeSat form factor. To this end, the examination of the cosmic background X-ray spectrum resulting from the “Big Bang” represented an achievable science objective with sufficient utility and interest to justify a satellite project. The SSC staff and students designed and built the Cosmic X-ray Background Nanosat (CXBN), a CubeSat with the mission to perform measurements of the cosmic X-ray background. CXBN-1 was successfully launched in 2012 and tracked by the project team at Morehead State University for four and a half months (Simms et al., 2012). The team was able to col-

lect some data and telemetry, but several difficulties, including a low signal-to-noise ratio, did not allow a significant amount of data to be downloaded (Healea et al., 2015). CXBN-2 was a follow-up to CXBN-1 that incorporated a number of technological improvements. Figure 1 shows both the flight model and the engineering model of CXBN-2, a 2U CubeSat. CXBN-2 was launched on April 18, 2017, as a secondary payload on Orbital Antares 7 (OA7) from Cape Canaveral to the International Space Station and was deployed in May of 2017.

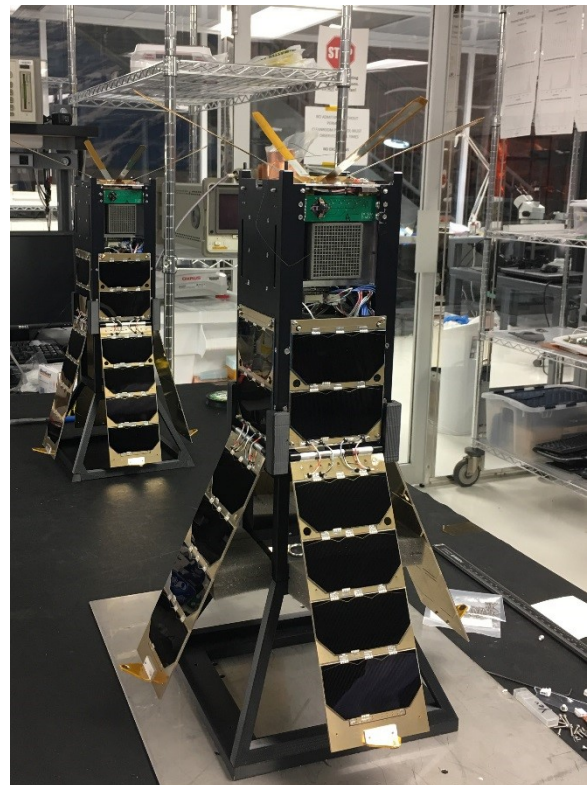


Figure 1. CXBN-2 spacecraft (flight and engineering models) in the Morehead State University Spacecraft Integration and Assembly Facility.

Worldwide, an ever-growing number of people are processing data from small satellites. Typical of them are researchers at universities, with an ever-growing industry and government participation. Currently, there is no commercial, general-purpose GSSW package available for this task. Therefore, the increasing demand for GSSW for small satellites is often met by the users of the satellites themselves. No standard has evolved yet for this task, despite the commonalities among the projects. As an example of an approach, an effort has been made by the NASA Ames Research Center called OpenMCT. This program is being used by the NASA Jet Propulsion Laboratory (JPL) and the NASA Ames Research Center. It shows promise but has not gained ground yet, being supported at a lower funding level (Trimble & Rinker, 2016).



---

## Related Work

Numerous GSSW development projects for small satellites have been undertaken by several universities around the world within the last decade, such as the Ground Station Software Telemetry and Telecommand (GSS TT&C) project developed by the University of Surrey for their PALM-SAT picosatellite (Akhtar & Underwood, 2007). The Georgia Institute of Technology (Choi, Stevenson, & Lightsey, 2017) is supporting five small satellite missions within a two-year framework (2017-2019) using a mission operation software package named QuantumCMD and made by Kratos Defense & Security Solutions, a national security solutions provider (White, 2014). Each of the five satellites has different communication requirements, due to different mission requirements and hardware components (Choi et al., 2017).

Vertat, Linhart, Pokomy, Masopust, Fiala, and Mráz (2018) at the University of West Bohemia in Pilsen, Czech Republic, set up a ground station that is being used to command and control their VZLUSAT-1 satellite. While they describe the ground station itself in great detail, they only mention that they wrote their command and data-handling (C&DH) software themselves. Transceiver frequency tuning and antenna positioner control was driven by several radio-amateur software tools, such as Predict and HamRadioDeluxe (Vertat et al., 2018). Miralles, Valle, Torres, Rosado, Isaac, and Rivera (2012) described a project implementing a CubeSat ground station in Puerto Rico. The GSSW used by that ground station consisted of software defined radio (SDR) as well as C&DH software with a GUI written in Python and Qt. Their SDR and digital signal processing (DSP) were implemented using the free software development toolkit GNU radio (Miralles et al., 2012).

Many projects for developing GSSW were led by students. One of these projects, a senior capstone project at the University of North Dakota, focused on communication security (Kerlin, Straub, Huhn, & Lewis, 2015). The main reason for deciding to write the GSSW in house instead of using existing software was that it would allow for more control and flexibility. It would not be necessary to spend money on purchasing software that might be difficult to adapt to the requirements of the project. Also, there would not be any need to request permission to use software or deal with copyright limitations. Furthermore, software written in house would be easier to modify for future projects. Also, there is very little documentation available related to aspects of data processing and presentation.

Most publications on GSSW for small satellites focus on tracking satellites and establishing communication with them, not on how the data retrieved from them is being processed, stored, and displayed. Many publications on GSSW describe the use of software-defined radio in great detail, while leaving out important information related to data processing.

## Goals and Objectives

In order to understand the GSSW requirements, the overall mission goals were examined, which led to a broad definition of the GSSW requirements. Additionally, there were specific hardware requirements that evolved as part of the project. These requirements shaped various subroutine requirements in the GSSW, which were adapted to the specific hardware used.

## Overall Mission of CXBN-2

As stated previously, the purpose of the GSSW was to process data from and send commands to CXBN-2, which would be performing measurements of the cosmic X-ray background. In addition to the cosmic microwave background radiation, which is a remnant of the Big Bang and is extremely well characterized and understood, the cosmic X-ray background is not as well understood (Chepponis & Kam 1987). The existing measurements of X-ray background in the 20-50 kilo electron volt (KeV) range differ by 20%. The mission of CXBN-2 was to obtain measurements with greater accuracy that differed by less than 5% and, thereby, constrained competing models that attempt to explain the origin of the diffuse X-ray background (Simms et al., 2012).

One of the most difficult challenges in studying the diffuse X-ray background is the fact that it is extremely difficult to observe X-rays at high resolution. Since X-rays tend to penetrate most materials, it is impossible to build a mirror to focus X-rays the same way it is done with visible light or radio waves (Koberlein, 2014). Another challenge is the fact that X-rays are absorbed by the Earth's atmosphere, which requires instruments that detect X-rays to be placed at high altitude, requiring the use of balloons, sounding rockets, or, in this case, satellites. Additionally, large spacecraft that have attempted to measure the diffuse X-ray background typically suffer from contamination of signal by spurious X-rays and gamma rays that are created in the spacecraft, as cosmic ray protons interact with the high-Z material in the spacecraft bus. This interaction causes fluorescence effects, thereby creating secondary photons in the region of interest. CXBN-2 eliminates this problem to a large degree by having very little high-Z material (and very little material at all being 2.4 kg). Measurement of the diffuse X-ray background is an example of science that can potentially be achieved more effectively with small spacecraft like the CubeSat form factor.

## Project Goals

The goal of this project was to develop a GSSW system that could process data transmitted back to Earth by CXBN-2, display these data in a graphical user interface (GUI), and archive the data. The first step was the development of beacon-decoder software, which was being used at the ground

station in Morehead. The primary component of the GSSW was a beacon decoder that would strip the telemetry data from the science data and process both separately. The telemetry was displayed on a dashboard-like graphical user interface. The telemetry contained important information about the status of the satellite, such as the power status of the battery, and magnetometer data to determine the satellite's attitude. The GSSW also allowed the user to uplink commands to the CXBN-2 satellite, which would respond to those signals either with an acknowledged (ACK) signal (if the command was executed successfully) or a not acknowledged (NACK) signal (if the satellite was unable to execute the command successfully).

The GSSW was designed to satisfy a set of primary and secondary requirements. Its primary goals were to perform standard GSSW mission operations, such as command, control, and data handling, including housekeeping, monitoring satellite health, and fault recovery. An additional goal of the GSSW development project was to create the ability to process the scientific payload data. The GSSW was designed specifically with the ability to receive CXBN-2 telemetry packets and display them on the GSSW GUI, as well as the ability to transmit command packets to CXBN-2, according to the selected parameters on the GSSW GUI, and show corresponding response packets from CXBN-2. One of the secondary goals of the GSSW development was to use a well-known programming language, such as C or C++, for platform independence. It was decided to use a combination of both, together with Qt 5, which was used to design the GUI. Another secondary goal was to connect to and communicate with low-cost radio modems, such as the Centronics Terminal Node Controller (TNC) using the KISS interface. KISS, which stands for "keep it simple, stupid," is a protocol for communicating with a serial TNC in amateur radio applications (Matondang & Adityawarman, 2018). Figure 2 shows how the TNC interacts with the control computer or terminal.

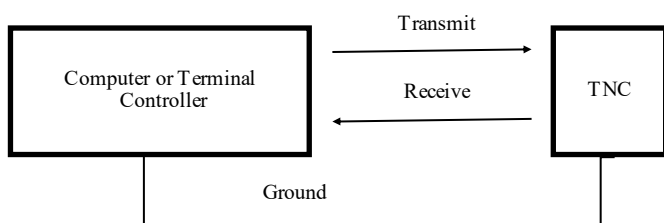


Figure 2. Diagram of the KISS interface with Kantronix TNC.

## Hardware Compatibility Requirements

The hardware of the GSSW consists of the central ground station computer, a USB-to-RS-232 adapter, and the Kantronix 9612+ Terminal Node Controller (TNC). The central computer, on which the GSSW is installed, runs a Windows 7 64-bit operating system. The USB-to-RS-232 adapter, as the name indicates, is a bi-directional, universal adapter that establishes the connection between the USB

port (on the central computer) and the RS-232 port (on Centronics 9612+ TNC). The ground software functions using any adapter available. The driver for the adapter is usually available for download on the manufacturer's website. The GSSW is not dependent on the specific adapter being used, because it can utilize the universal Windows serial communication API (Integrated into Qt Serial Port library).

The CXBN-2 satellite uses an AstroDev Li-1 UHF transceiver manufactured by Astronautical Development (AstroDev), LLC, for data transmission. The transceiver uses Gaussian frequency shift keying (GFSK) modulation on a 437.525 MHz frequency. Its baseline configuration provides command uplink at 9.6 Kbit/s and telemetry downlink at 9.6 Kbit/s. The transceiver is reconfigurable in flight with up to 38.4 Kbit/s (Astronautical Development, LLC Radio Interface Manual, 2013). The corresponding ground station transceiver is an ICOM America IC-910H transceiver. This radio has power outputs of 100W at VHF and 75W at UHF, and was used as the primary transmit/receive device. Although specific hardware components were used, as mentioned above, the GSSW was designed with flexibility in mind and would not be dependent on these specific components. In fact, the GSSW can handle any hardware interface. This was accomplished by using an object-oriented programming approach (OOP). Object-oriented programming has been used successfully since the late 1980s to program in a more structured and modularized fashion (Lewis & Loftus, 2008).

## Software Development

The main components of the GSSW were the beacon decoder software and the GUI. The beacon decoder software was written in C++ using Qt to create the GUI. Due to its speed and stability, C is commonly used to write software for satellite operations, including the software on the satellite itself (Pritchett, Kamrath, Kineman, & Wilson, 2016). C++ offers an advantage over pure C in that it supports object-oriented programming. The main use for Qt is in the development of application software that employs graphical user interfaces (GUIs). It is, however, possible to use Qt for developing programs without a GUI, such as command-line tools and consoles for servers (Qt website, 2016). Inheritance, which is a very commonly used concept in OOP, allows the easy creation of new modules, thereby extending the capabilities of existing ones. This OOP approach reinforces the modularity of the GSSW structure, permitting custom modules to be written without having to scrap the whole framework and start over. This avoids the problem of "spaghetti code," which is very common in university-based projects.

After the primary goals had been fulfilled, a software module was developed to process the scientific data that were gathered by the CXBN-2 payload. All of the X-ray science data were collected by a REDLEN CZT array (256 pixel) (Healea et al., 2015). This instrument differs from the

one flown on CXBN-1 by having twice the detector array and having undergone more accurate calibration and characterization (Haught, Wilczewski, Malphrus, & Brown, 2014). Improvements also include customizing the addressable pixels to have high gain in the 20-50 keV range. The data collected by the REDLEN array can be broken down into the  $x$  and  $y$  coordinates along with the intensity or energy range of pixels in order to generate a bitmap image. The software was also designed to be able to generate multiple graphs. This was originally a low-priority item, because the science data could be processed at any time, while the telemetry data need to be processed while the satellite is transmitting.

## Software Implementation

The satellite transmits a beacon signal that is received by the ground station through a VHF/UHF radio. The GSSW processes this beacon signal, which consists of multiple components. Data from the satellite arrive in the form of a radio signal that is converted by the ground station hardware into data packets. These packets are arrays of bytes that can be read and interpreted by the GSSW, which listens to the serial port for such packets to arrive. Once the packet is received, the software determines if the packet is a telemetry packet or a response packet and process it accordingly. Telemetry packets contain scientific and housekeeping data, while a response packet contains an indication whether a command previously sent to the satellite was successful or not. The GSSW determines the packet type based on the length of the packet. Telemetry packets are 284 bytes long, the first 50 bytes of which are simple housekeeping data such as status of different batteries and timestamps, followed by 230 bytes of scientific data. The last four bytes are

two checksums with two bytes each. This packet structure is very commonly used by CubeSats to communicate with their ground stations (Celik, 2003). The GSSW was designed to be easily adjusted to accommodate other formats. Figure 3 provides an overview of how the different components of the GSSW handle commands to be sent as well as data received.

Another challenge was the different speeds at which the data packets arrive, which is essentially a queueing theory problem. The essence of queueing theory is that it considers the randomness of the arrival process and the randomness of the service process. The most common assumption about the arrival process is that the customer arrival epochs follow a Poisson process (Taha, 2017; Winston, 2004). The GSSW system can be considered an M/M/1 queue. The arrival rate of the packets varies and generally follows a Poisson process.  $a$  is the average number of packets received over a fixed time interval. The times between arrivals (the inter-arrival times) are exponentially distributed. The ratio between the arrival rate and the processing rate determines the queue size.  $T$  is the average time between packets over a fixed time interval. The probability density function for the inter-arrival times is given by Equation 1:

$$P(n < 1) = \frac{\alpha^0 e^{-\alpha}}{0!} = e^{-\lambda T} = P(t > T) \quad (1)$$

which is based upon a discrete Poisson distribution, and

$$P(n) = \frac{\alpha^n}{n!} e^{-\alpha}$$

where,

$$\alpha = \lambda T$$

$$p(t) = \lambda e^{-\lambda t}$$

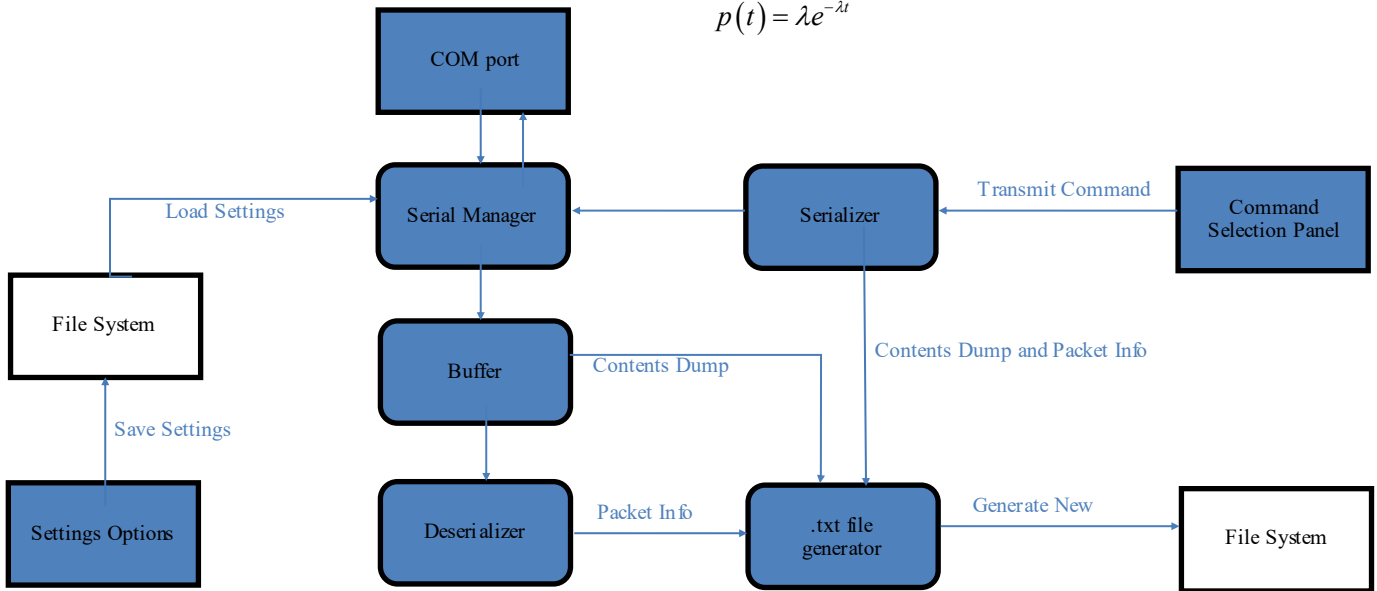


Figure 3. Flowchart of the GSSW.

The average queue size turns out to be as shown in Equation 2:

$$\bar{n} = N = \frac{\rho}{1 - \rho} \quad (2)$$

where,  $\lambda$  is the average arrival rate,  $\mu$  is the average processing rate (also called departure in the literature) out of the queue,  $\rho$  is  $\lambda/\mu$  (Taha, 2017; Winston, 2004), and  $n$  is the instantaneous number of frames in the buffer.

Since, in the case of the GSSW the buffer size is 256, the actual buffer size (at any one time) is  $N \times 256$  bytes. The processing rate depends on the computer being used. In the case of the GSSW, this was a 2.67 GHz Intel E6750 Core2 Duo with 4 GB of RAM. The dwell times did not figure significantly into the overall delay. The radio used for CXBN-2 operated at 9600 baud (bits per second); 9600 baud represents 960 characters per second (8 bits/character, 1 start bit, 1 stop bit). The data were processed at roughly 10 frames per second. A frame consisted of roughly 100 bytes. If the frame size was 100 bytes, then 9.6 frames were processed per second. This corresponded to the frame arrival rate, otherwise known as  $\lambda$ . As noted previously, the processing rate,  $\mu$ , was 10 updates per second. Since the average buffer size,  $N$ , was 24, at least 2400 bytes of buffer were needed. The wait time was  $N/\mu$ , which resulted in a wait time of 2.4 seconds.

Processing the payload data represented the most complicated part of the telemetry packet. First, its components were in random order and were present in a random number of instances. The payload contained four component types: payload (4 bytes), photodiode (1 byte), magnetometer (5 bytes), and thermal (2 bytes). The first four bits of any of the four types contained an identifier that revealed the type of component, which told the parser how many bytes to read in until the next identifier for the next component was to be expected (Pritchett et al., 2016). Table 1 shows how the different payload data types were broken up into bytes and half bytes. An example is the structure of the magnetometer data, which are as follows: Magnetometer identifier = 4 bits, Magnetometer X axis data = 1.5 bytes, Magnetometer Y axis data = 1.5 bytes and Magnetometer Z axis data = 1.5 bytes. The GSSW was originally written to process a sequence of whole bytes, but was later modified to process partial bytes. This strategy allowed for shorter packets, which increased the efficiency of the software.

Also, a buffer was created that had enough space for each type of payload data so that it could read the entire section at once. For example, once the magnetometer data type is encountered, the entire 5 bytes of magnetometer data are read into a buffer all at once. After the magnetometer data are read in, masking and bit shift operations are performed on the 5 bytes to break down the data into their meaningful components (Pritchett et al., 2016).

Table 1. The data stream.

Payload	0xA or 0xB, 0.5 byte (4 bits)	Payload identifier
	1 byte	Payload time stamp
	1 byte	Payload pixel number
Magnetometer	1.5 byte	Payload ADC (Output energy level)
	0xC, 0.5 byte (4 bits)	Magnetometer data Identifier
	1.5 byte	Magnetometer X axis data
	1.5 byte	Magnetometer Y axis data
Photodiode	1.5 byte	Magnetometer Z axis data
	0xD, 0.5 byte (4 bits)	Photodiode identifier, constant
Thermal	0.5 byte	Photodiode data
	0xE, 0.5 byte	Thermal data identifier, constant
	1.5 byte	Thermal data

Figure 4 shows that the GSSW was also capable of allowing the user to send commands to CXBN-2 via the GUI. Since all command packets were similar in structure, a base data structure was created to serve as a template for each type of command packet. Command packets were assembled from user input and sent out through the serial port after the send button had been pressed. The radio equipment then converted the packets from byte arrays to a radio signal and transmitted them to the satellite. Once a command packet arrived at CXBN-2, the satellite's flight software determined the type of command. If the command was executed successfully, a response packet containing either an ACK (acknowledged) or a NACK (not acknowledged) was sent back to the ground station. The size of the response packet varied. The purpose of the response packet was to inform the user at the ground station if the command was executed successfully (Pritchett et al., 2016).

Since the telemetry data packets were expected to arrive at relatively fixed intervals, the system was designed so that each data packet could be processed, displayed, and moved to storage before the arrival of the next. This system could be considered an M/M/1 queue (Taha, 2017; Winston, 2004), since there was only one instance of the GSSW processing the arriving data packets. An SVN repository and remote desktop application was established for the team's use. The SVN used was Tortoise, and the remote desktop application of choice was TeamViewer. The target TeamViewer client had the ability to simulate incoming and outgoing data streams for the satellite. The use of this streamlined the development and testing processes, as the team would no longer have to send the software to be tested, and allowed the team to do more in-depth analysis of software during run-time and debug processes. In addition, the SVN allowed for the streamlining of workflow, as the team could easily access and update the application at any time, as well as log and track changes and revert versions if needed.

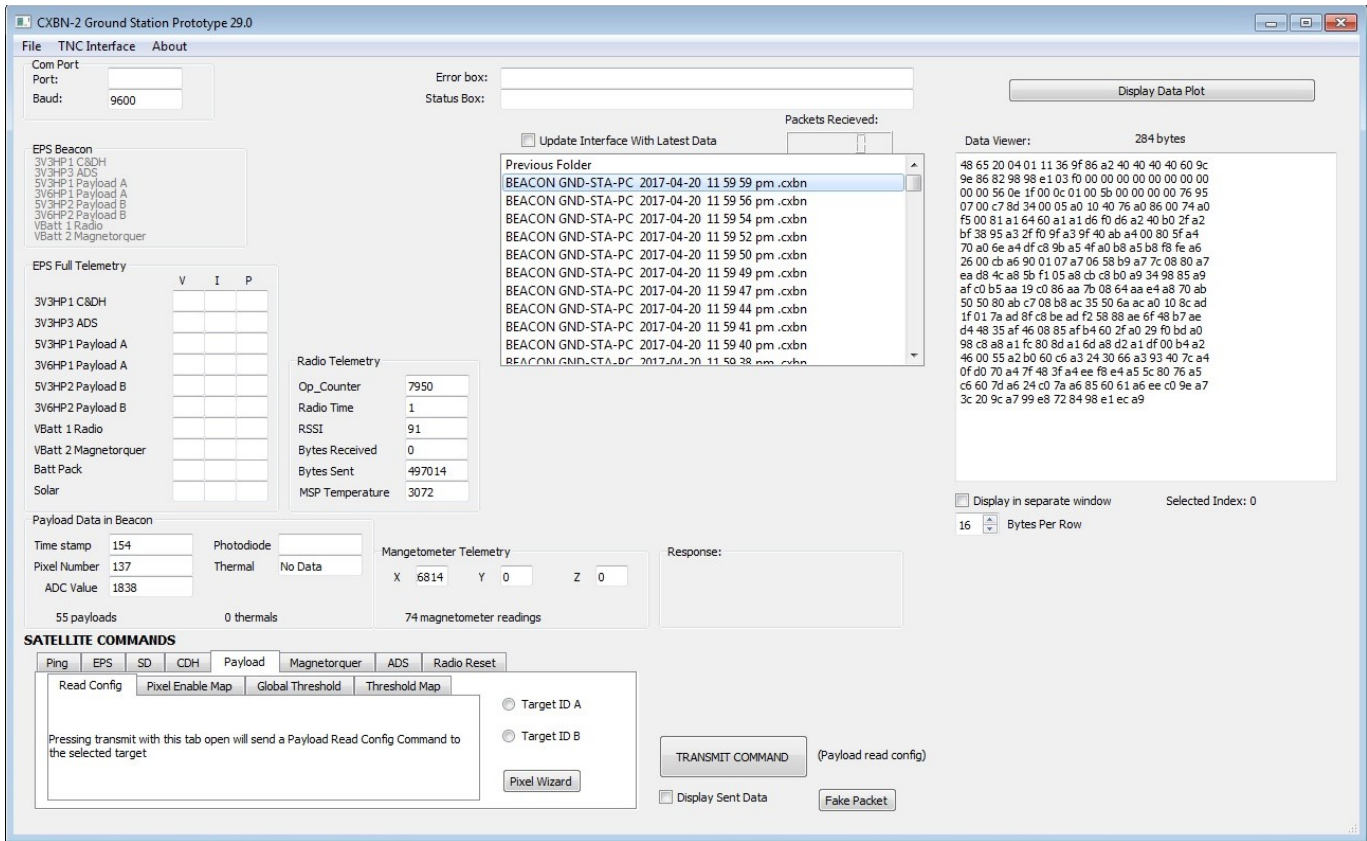


Figure 4. A screenshot of the GUI.

One major issue was the unanticipated changing of packet specification and data formats, which led to continual problems during the development process. Originally, the satellite would send a data packet of a fixed size of 283 bytes, with fixed-length sections for each of its components. The software was designed with this in mind; however, after several bugs suddenly came up, and with no apparent way to correct them, it was eventually discovered that the packet format was changed to a variable-size format. This problem was corrected by checking section headers as the incoming packet was deconstructed and storing the results into arrays of variable size. Another issue that lingered for a while was a series of errors in reading the science data. Upon further inspection, it was discovered that the issue was caused by a change in the sequential order of bytes in the incoming science data stream. This resulted in values that were far off from their expected numbers. This was fixed, as well as the constant multipliers adjusted for the associated values. These values were important for the conversion of voltage and current readouts to a format more easily readable by the user.

With respect to the science data, a new feature was added; a basic function that saved specific combinations of data to .txt files. These data sets, Pixel Address versus ADC Val-

ue and ADC Value versus ADC count, were meant to be used in another application outside the scope of this project, so a universal file type was selected for this purpose. Additionally, the function had the ability to pass these values to another newly constructed module, the data charter. Using these values, or ones that were previously saved, the data charter generated graphs to visualize the data, and save it if desired. If the option to use current data stream values was selected, the chart automatically refreshed to reflect new incoming data. If the user desired, the chart could be cleared. New values could be loaded in as a new chart or appended to the current one.

File-system handling was altered in an attempt to create a more robust, lightweight system that would demand fewer resources. This was done by multiple means. First, the amount of calls to the file system for list updates was reduced drastically. Second, the module was altered to save files in a subdirectory by the hour that they were received, which was within a folder by the month and day; this would increase the organization of gathered data and reduce the number of files that the function would gather upon an update. Third, a more reliable means for tracking directory location was implemented. Finally, functionality was added to load and save commands for later use.

## Software Testing

Compatibility testing utilized an engineering model of the spacecraft and initially simulated ground stations. Later, live ground stations, including the 21-meter space tracking antenna in Morehead, were used. This engineering model was a so-called flat sat. It consisted of identical duplicates of all the hardware components of the actual satellite, but was laid out in a manner that allowed all components to be accessed conveniently for testing. The project faced a great improvement with the establishment of an SVN repository and remote desktop access to a test machine.

The frequency and quality of updates picked up substantially with the adoption of remote desktop testing and SVN repository. Many issues that surfaced were difficult to diagnose until these tools were incorporated into the workflow. Before this, users would often use software builds that were several versions behind, or sometimes tests would take months to occur. Better control of the testing phases allowed the team to work more quickly and better target problematic areas.

## Results

The project resulted in a clear and organized GSSW that was easy to use, even without a user manual. It was ready to be used when CXBN-2 was launched aboard Orbital Atlas 7 on April 18, 2017. The satellite was deployed from the ISS on May 16<sup>th</sup> at 7:55 AM (EST). The solar panels and UHF antennas deployed 30 minutes later and CXBN-2 started transmitting its beacon signal. However, communication with CXBN-2 was lost early on and the ground station did not receive any packets through the CXBN-2 GSSW. After switching to real time, it was possible to receive the raw data. Several aspects of the user interface did not work properly or only worked sporadically. Originally there were plans to port the software to other ground stations, but these plans were later rescinded.

One major change was in the pixel map and threshold wizard. Due to bandwidth limitations, not all of the pixels captured by the CZT detector could be displayed by the GUI. The solution for this problem was to consolidate pixels using a pixel map. The interface had a coordinate map on the pixel enable/disable button section and on the threshold value panel. In addition, an improved file save/load function was implemented to streamline the process for the user. The option to save pixel maps with either auto-generated names or custom names was added. Table 2 shows that an Agile software development approach was used, which was meant to develop a minimum working version and then increment in small steps (Agile Alliance, 2019). In the initial version of the GSSW, all parameters were hardcoded and tested to see if it would fulfill minimum requirements. With each iteration, more flexibility and new functions were added, followed by another round of testing. This approach was very successful and led to a more robust software, while, at the same time, being flexible to adapt to changes in requirements. The GSSW evolved through 20 different versions over a short period of time (< 1 month).

Having all team members in the same physical location for a short time during the initial phase of the project and then continuing collaboration over Skype led to rapid progress. Between 70% and 80% of the GSSW was completed during a single session at Morehead, the remainder was accomplished over the course of three months with teams working at their individual sites and communicating over the internet.

## Conclusions and Future Work

The importance of implementing functionality first was quickly realized. Aesthetics and user friendliness will be improved in later iterations of the GSSW. A database and a command dictionary will be among the improvements to be added to the next version of the GSSW. Currently, the data

Table 2. Timeline of software development and testing.

Timeline for developing GSSW for CXBN-2									
Year	2016							2017	
Milestone Activity	Jul	Aug	Sept	Oct	Nov	Dec	Jan	Feb	Mar
1 Requirements Analysis									
2 Development of Initial Version									
3 Initial Testing									
4 Bug Fixes, Updates and Adjustments									
5 Addressing Secondary Goals									
6 Improving User Friendliness									
7 Final Troubleshooting									
8 Final Version Completed									

are stored in an individual file per beacon located within a folder that is time stamped. Having the software store all data from each pass in a single database file can make viewing the data significantly easier. Data from different payloads can then be stored in individual database tables and the database can be queried using SQL commands. The CXBN-2 GSSW will be adapted for future smallsat missions. CXBN-3, with similar mission specifications, is currently in the early planning stage and uses primarily the same hardware. There is a possibility that a radio with a much higher bandwidth (and much higher data rate) will be used for CXBN-3.

With some minor improvements, the GSSW can easily be adapted for use with CXBN-3 and subsequent similar missions. The same general method and analysis can be used in the development and optimization of any ground control system. Further development will lead to a more generic GSSW package that is easily adapted to a variety of uses. The end goal is to minimize the effort to implement GSSW for a university CubeSat mission. With more bandwidth and a faster computer, the capabilities of the GSSW can be expanded to accommodate such things as flipped bits in data reception, instant spectral calculations, and live pixel data.

## Acknowledgements

The authors would like to thank the following students for their work in developing and testing the GSSW: Aaron S. Pritchett, Dylan J. Wilson, Daniel L. Kineman, and Daniel M. Kamrath from Murray State University. Tobias D. Gedenk, Chloe M. Hart, Michael R. Glaser-Garbrick, and Nathaniel J. Richard from Morehead State University.

## References

- Agile Alliance. (2019) *What is Agile Software Development?* Agile Alliance. Retrieved from <https://www.agilealliance.org/agile101/>
- Akhtar, S., & Underwood, C. (2007). Dynamic Command and Data Handling Ground Station Software. Paper presented at the 3rd International Conference on Recent Advances in Space Technologies Istanbul, Turkey, 14-16 June.
- Astronautical Development, LLC. (2013). *Radio Interface Manual* Astronautical Development, LLC. Retrieved from [www.aastrodev.com](http://www.aastrodev.com)
- Celik, E. (2003). Ground Station Control Software Application, Proceedings of International Conference on Recent Advances in Space Technologies, Istanbul, Turkey, 20-22 November (pp.177-181).
- Choi, T., Stevenson, T., & Lightsey, E. (2017). Reference Ground Station Design for University Satellite Missions with Varying Communication Requirements. Paper presented at the AIAA SciTech Forum, 55th AIAA Aerospace Sciences Meeting, Grapevine, Texas, 9-13 January.
- Darbali-Zamora, R., Ortiz-Rivera, E. I., & Rincon-Charris, A. A. (2015). The Puerto Rico CubeSat project to attract STEM students into the area of aerospace engineering. Paper presented at the 2015 IEEE Frontiers in Education Conference (FIE) El Paso, Texas 21-24 October.
- Deepak, R., & Twigg, R. (2012). Thinking Out of the Box: Space Science Beyond the CubeSat. *Journal of Small Satellites*, 1(1)3-7.
- Garg, L., Kand, A., Pradhan, M., & Agarwal, A. (2019). Automated Ground Station Design for an Amateur LEO Satellite System, Paper presented at the 2019 IEEE Aerospace Conference, Big Sky, Montana 2-9 March.
- Haight, K., Wilczewski, S., Malphrus, B., & Brown, K. (2014). Small Satellite Mission Operations at Morehead State University. Paper presented at the CubeSat Developers' Workshop, California Polytechnic State University, San Luis Obispo, CA, 23-25 April.
- Healea, J., Malphrus, B., McKneil, S., Brown, K., Kruth, J., Twigg, R., ...Cavins, A. (2015). The Cosmic X-Ray Background Nanosat-2 (CXBN-2): An Improved Measurement of the Diffuse X-Ray. Presented at the CubeSat Developers' Workshop, California Polytechnic State University, San Luis Obispo, CA, 22 April.
- Kerlin, S., Straub, S., Huhn, J., & Lewis, A. (2015). Small Satellite Communications Security and Student Learning in the Development of Ground Station Software. Paper presented at the IEEE Aerospace Conference, Big Sky, Montana 7-14 March.
- Koberlein, B. (2014). Exploring the Cosmic X-ray Background. Retrieved from <http://phys.org/news/2014-09-exploring-cosmic-x-ray-background.html>
- Lewis, J., & Loftus, W. (2018). *Java Software Solutions Foundations of Programming Design* (9<sup>th</sup> ed.), Pearson: Upper Saddle River, New Jersey.
- Malphrus, B., Kruth, J., Combs, M., Fite, N., Twigg, R., & Schulze, R. (2010). A University-Based Ground Station: The 21 M Antenna at Morehead State University. Paper presented at SpaceOps 2010 Conference Huntsville, Alabama 25 April.
- Malphrus, B., Combs, M., Kruth, J., Brown, K., Twigg, R., Thomas, E. ...Clements, T. (2012). University-Based Nanosatellite Missions and Ground Operations at Morehead State University. Presented at the SpaceOps 2012 Conference. Stockholm, Sweden, 11-15 June.
- Matondang, J., & Adityawaman, Y. (2018). Implementation of APRS Network Using LoRa Modulation Based KISS TNC 2018. Paper presented at the International Conference on Radar, Antenna, Microwave, Electronics, and Telecommunications (ICRAMET) Sepong, Indonesia, 1-2 November.
- Miralles, D., Valle, O., Torres, N., Rosado, J. G., Isaac, R., & Rivera F. (2012). Nanosatellite Ground Station using Software Defined Radios. Paper presented at the Society of Hispanic Professional Engineers Conference, Fort Worth, TX, 17 November.
- Puig-Suari, J., Tumer, C., & Twigg, R. (2001). CubeSat: The Development and Launch Support Infrastructure

- for Eighteen Different Satellite Customers on One Launch. Paper presented at the 15th Annual USU Conference on Small Satellites, Utah State University, Logan, Utah, 13-16 August.
- Pritchett, A., Kamrath, D., Kineman, D., & Wilson, D. (2016). Development of the Ground Station Software for CXBN-2. Presented at Kentucky Academy of Science (KAS) conference 2016 Louisville, KY, 5 November.
- Qt (2016). *What's New – Qt 5.7*, Retrieved from <https://www.qt.io/qt5-7/>
- Simms, L., Jernigan, J., Malphrus, B., McNeil, R., Brown, K., Rose, T. . . Sun, S. (2012). CXBN: A Blueprint for an Improved Measurement of the Cosmological X-Ray Background. Presented at SPIE Optics and Photonics San Diego, CA, United States 12- 16 August.
- Taha, H.A. (2017). *Operations Research -An Introduction*, (10<sup>th</sup> ed.), Pearson: Upper Saddle River, New Jersey.
- Trimble, J., & Rinker, G. (2016). Open Source Next Generation Visualization Software for Interplanetary Missions. Presented at the 14th International Conference on Space Operations, Daejeon, Korea 16-20 May.
- Vertat, I., Linhart, R., Pokomy, M., Masopust, J., Fiala, P., & Mraz, J. (2018) Small satellite ground station in Pilsen - experiences with VZLUSAT-1 commanding and future modifications toward open reference ground station solution. Presented at the 28th International Conference Radioelektronika (RADIOELEKTRONIKA) Prague, Czech Republic, 19-20 April.
- White, Y. (2014). *Kratos Introduces quantum CMD for Small Satellites and Fleets of Small Satellites*. Retrieved from <https://ir.kratosdefense.com/news-releases/news-release-details/kratos-introduces-quantumcmdtm-first-command-and-control-system>
- Winston, W. L. (2004). *Operations Research: Applications and Algorithms* (4<sup>th</sup> ed.) Cengage: Boston, Massachusetts
- Zetocha, P., & Brito, M. (2001). Development of a testbed for distributed satellite command and control. Paper presented at the 2001 IEEE Aerospace Conference. Big Sky, Montana, 10-17 March.
- University of Maryland, and PhD in electrical engineering in 1999 from the Catholic University of America. Dr. Connor may be reached at [cdconner@captechu.edu](mailto:cdconner@captechu.edu)

**BENJAMIN MALPHRUS** is professor of space science at Morehead State University, where he also serves as the Executive Director of the University's Space Science Center. He earned his BA in studio art from the University of South Carolina in 1984, MS in astrophysics from the University of South Carolina in 1987, and EdD in Physics and Astronomy from West Virginia University in 1991. Dr. Malphrus may be reached at [b.malphrus@moreheadstate.edu](mailto:b.malphrus@moreheadstate.edu)

## Biographies

**MARC BECK** is an assistant professor of computer science at Murray State University. He earned his BS in computer science from Brescia University in 2007, MS in industrial technology in 2009 from Morehead State University, and PhD in computer science and computer engineering in 2015 from the University of Louisville. Dr. Beck may be reached at [mbeck4@murraystate.edu](mailto:mbeck4@murraystate.edu)

**CHARLES CONNOR** is Chair of Engineering at Capitol Technology University. Previously, he was a staff scientist and professor of electrical engineering at the Space Science Center of Morehead State University. He earned his BS in electrical engineering from the University of Maryland in 1979, MS in electrical engineering in 1987 from the



# PROOF OF CONCEPT: DESIGN PARAMETERS FOR A NANOSCALE INTERDIGITATED ELECTRODE SENSOR FOR COVID-19 DETECTION

Mohammed Abdallah, State University of New York Poly

## Abstract

There are three main types of test for SARS-CoV-2 (COVID-19 or COVID). These include polymerase chain reaction (PCR) or nucleic acid amplification test (NAAT), blood test/antibody or serology testing, as well as antigen tests. Each method has positive and negative aspects to it and they are used in different scenarios. Impedance-based biosensing provides a unique, highly sensitive electrical approach to biomolecule detection, cell growth, and other biological events. A nano-bio sensor was evaluated in this current study for detecting COVID-19. Different design parameters were simulated in order to understand how nanoscale electrode size, spacing, and structure would affect a model biosensing assay (antibody-based affinity binding of a protein antigen). The model was tested and verified via COMSOL and predicted increasing impedance during functionalization of electrodes with antibodies and after antigen binding steps. In this paper, the author reports the expected change of impedance from different electrode dimensions, which is a step towards optimization of the design, prior to device fabrication and testing.

## Introduction

There are three main types for SARS-CoV-2 (COVID-19 or COVID) tests. These include polymerase chain reaction (PCR) or nucleic acid amplification test (NAAT)—these two are grouped together as one type—blood test/antibody or serology testing, as well as antigen tests. Each method has advantages and disadvantages and is used in diverse scenarios (Whittington et al., 2020). PCR or NAAT testing is also called molecular/viral testing and is done by swabbing the nose or mouth or by collecting saliva. Once DNA is collected, the PCR technique is used to amplify the DNA. This works by heating the DNA until it splits into two pieces then using an enzyme called taq polymerase to rebuild the two pieces. This process is repeated many times in order to attain billions of copies of the same DNA segment. Comparing known genomes to the subject's DNA allows specialists to determine if a person has, or has had, the virus. It's worth noting that PCR testing works on a wide variety of viruses, bacteria, parasites, and more. One major advantage of PCR testing is that it's accurate. PCR testing is considered the key standard of tests and is often used as a double check if another method reports a positive result. When someone is showing symptoms of COVID and tests positive using a PCR test, it is assumed they have the virus.

That being said, there are some limitations. When administered within a few days of contracting the virus, likely before symptoms appear, it has been found that the false negative rate is anywhere from 50% to 100% (Whittington et al., 2020). Blood tests work by examining a blood sample from a person and attempting to detect antibodies that the body produces to fight off the virus. There are two types of antibodies: IgM, which happens early in an infection, and IgG, which shows up later on. It can take up to three weeks for the body to produce a detectable level of antibodies. Detection of either one can indicate that the person has had COVID, but the detection of IgM antibodies means it is possible that the person is still contagious. So far, it is unknown if having antibodies makes a person immune for any period of time. If that turns out to be the case, that would make antibody tests more in demand, as it would allow certain people to return to a more normal routine (Whittington et al., 2020).

Antigen tests are done by swabbing the inside of the nose and then using the sample to detect a protein on the surface of the virus. They can be performed very quickly, in as little as 10 minutes, making this a very convenient method. The results from this kind of test are reasonably accurate. A positive result is considered extremely accurate, though there is a possibility of false negatives. This is likely due to the fact that this test does not detect small levels of the virus. If accuracy can be increased, antigen tests may be the best bet for wide scale, rapid testing, which would be critically helpful to society. Low cost is another advantage (Whittington et al., 2020). Although not necessarily a test, there has been development of a monitor that would be implanted into the body. This would monitor for key characteristics of the virus, specifically temperature and resting heart rate. With the data from the monitor being constantly collected, it would be easy to detect a sudden change or a trending change that might indicate an underlying issue such as COVID. This could be a huge development beyond COVID, where people could be screened 24/7 for possible complications and have the luxury of much earlier warning/detection.

Biosensors can be used in a wide range of applications to detect cells (Radke & Alcocilja, 2004), toxins (Chen, Fang, Liu & Zeng, 2012), and to monitor diseases in early stages (Zeng, Shen & Mernaugh, 2012). A variety of mechanical, optical, and electrochemical concepts can be used to design and develop biosensors (Zeng et al., 2012). Electrochemical detection methods are ideal for biosensing applications, especially in the case of quick and affordable detection

(Ahn, Lee, Li, Heo, Hong & Ko, 2011). Electrochemical biosensors measure changes in electrical properties that result from the presence of biological moieties (whole cells, proteins, nucleic acids, and other biomarkers). Interdigitated electrodes (IDEs) are one potential type of electrochemical sensing format for biosensing applications. Changes in the electric field at the surface of the IDEs are measured when biological moieties interact with the IDEs, or within the spaces between the IDE electrodes (Manickam, Chevalier, McDermott & Ellington, 2010). IDEs are used to detect and analyze cells or biomarkers by using multi-frequency, impedance-based characterization. Detection and characterization are based on the dielectric properties of the cells/biomarkers (capacitance and conductivity). In the case of whole cells, this can lead to the detection of physiological differences between cells or changes in cell morphology or size over time. IDEs can achieve a wide range of advantages over traditional methods such as real-time detection, label-free analysis, non-invasive sensing, ease of integration, and high-throughput screening.

Based on the space between the electrodes and the bio- or chemical-selective layer deposited on the electrodes, an IDE-based sensor can detect any analyte that has a difference in electric constant from the background solution/medium. For resistive IDE chemical sensors, a conductive thin layer should cover the electrodes. The thin sensing area resistance will change due to the concentration of the analyte. Randle's model can be used to understand the electrical interactions between the electrodes, sensing layer, target cells, and surrounding solution. Extensive research has been performed on the sensing area between the electrodes in IDE chemical sensors. The reason that this sensing area is critical for IDE sensors is that it controls either resistance or capacitance changes due to the presence of the analyte/cell/particles/molecule under consideration. Moreover, the shape of the sensing area between the electrodes is also critical. Traditional square morphologies may result in non-optimal sensing areas. For example, some research efforts have considered curved or sharpened edges of the interdigitated electrodes. Other research work has been performed on the dimensions of the IDE sensor to optimize the sensing area (Fraden, 1997).

Previously, an impedance-based model was reported for cell counting using COMSOL. The effects of gold nano particles on IDE-based sensors were modeled using the same platform. Cell growth modeling and bacterial detection have also been reported. Even though antibody-antigen-based biosensing is one of the most common ways impedance sensors have been used, there has been no known COMSOL model reported on such a system (Binachi, Francesco, Enrica, Gabriele & Carlotta 2012). In this current study, the impact of IDE electrode size and spacing on impedance-based detection of antibody-antigen interactions of COVID-19 using COMSOL was simulated. Optimization of these parameters is guiding subsequent work to fabricate IDE-based sensors for disease diagnosis.

## Design and Simulation: COVID-19 Testing IDE Sensor

The finite element analysis multi-physics simulation software COMSOL was used to simulate an IDE-based impedance spectroscopy sensor. The AC-DC module of COMSOL was used to simulate the electrical response of an IDE impedance sensor, add bio-selective materials (antigens) to the sensor, and to calculate the change in the impedance upon addition of biological target elements (antibodies/IgG) to the IDE. IDEs can be fabricated using a variety of techniques. For this current study, IDEs were simulated based on a nanoscale damascene process in which the IDE pattern is etched into a dielectric ( $\text{SiO}_2$ ) filled with a metal electrode layer (in this case, Cu) and then planarized using chemical mechanical planarization (CMP). Figure 1 shows the general format of the IDEs simulated in this study.

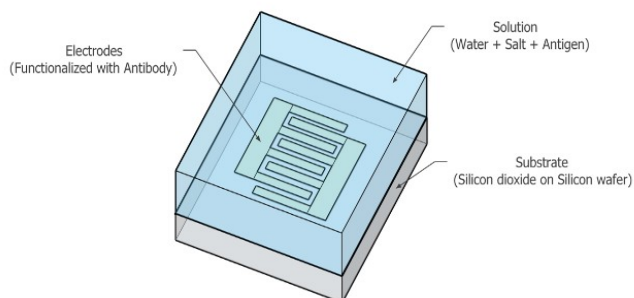


Figure 1. Schematic of the interdigitated electrode configuration modeled in this study.

The IDE electrodes had a width of  $A$ , length of  $F$ , and spacing of  $B$ . An insulating layer,  $D$ , of  $\text{SiO}_2$  was placed underneath the IDE, while the total thickness of the  $\text{SiO}_2$  insulator was represented by  $E$ . Table 1 lists the starting dimensions that were used in the simulations, while Figure 2 illustrates the geometry of the IDE. IDE electrodes were simulated as the capacitive element in an RC circuit in COMSOL, and the relative geometry of the IDE electrodes was modulated and assessed for electrical impedance changes within the context of antibody-antigen-based biosensing. Figure 3 shows that, in this case, protein-based antigens were placed on the surface of the IDE electrodes (linked via a thin attachment layer), followed by addition of an antibody (IgG).

Table 1. IDE dimensions used for the initial model.

Parameter	Dimension
$A$	100 nm
$B$	100 nm
$C$	130 nm
$D$	120 nm
$E$	250 nm
$F$	1400 nm

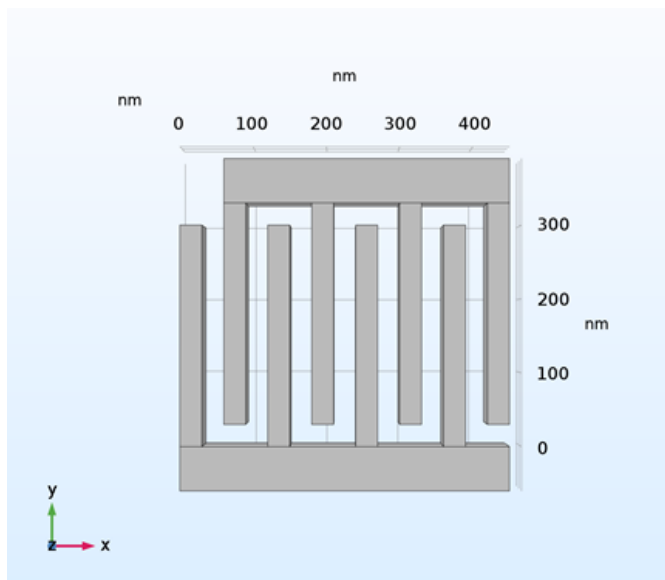


Figure 2. Schematic showing the geometry of the electrode area.

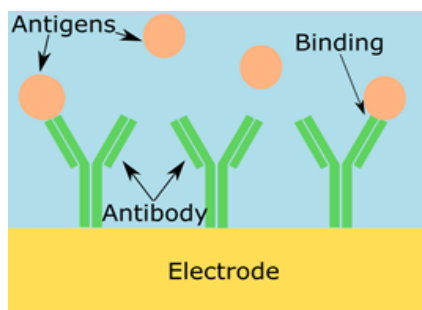


Figure 3. Example showing functionalization of the electrode surface and subsequent immobilization of antibodies, followed by antigen binding.

This simulates a common biosensing approach in which blood-borne antibodies react with the sensor to indicate an immune response to a pathogen. Using this approach, small changes in the number of antibodies bound to antigens on the IDE surface should impart a measurable change in impedance. It is sought to determine how changes in the width and spacing of nanoscale IDE electrodes would affect the impedance response for this biosensing approach. The author has worked on this idea and proved the concept that a change in impedance can be a valid indicator for the binding and existence of the virus (Abdallah, 2021). The author not only proved the concept but a prototype was built, developed, and evaluated via a state-of-the-art FPGA. Table 2 shows, from the simulation in this study, the antigen and antibody dimensions and parameters.

COMSOL was used to simulate the IDE circuit and determine how changes to IDE design would affect the impedance measured at different frequencies. Nyquist plots were used to visualize changes in impedance under these differ-

ent conditions. It was expected that the impedance would increase as more protein was added. A Nyquist plot (imaginary component of the impedance  $|Z|$  vs. the real component of  $|Z|$ ) shows any change in the impedance when protein or IgG is added to the IDE surface. The assumption was that increasing the amount of dielectric on the electrode would create additional resistance (and possibly capacitance), which should cause an increase in the diameter of the semi-circle (absolute value of impedance level) for the measurement.

Table 2. Antigen and antibody simulation dimensions.

IgG diameter	100 nm
Protein layer width x length	100 nm x 1400 nm

## Results and Discussion

In this section, different design aspects of the IDE sensor will be introduced: a) a proof of the concept that the ISE sensor's impedance changes, based on the exiting of the antigens and antibodies; b) 2D and 3D simulation models along with a discussion of the effect of the virus coverage and quantity; c) sensor dimensions and size are discussed as key design factors, when this proposed sensor is fabricated; and, d) three sensor structures. COMSOL was first used to simulate three different scenarios for nanoscale IDEs. The first scenario simulated bare IDE electrodes with no protein-based antigen or IgG above the copper electrodes. The second scenario simulated addition of the antigen coating layer above the copper IDE electrodes but with no IgG binding. The third scenario explored IgG binding to the antigen coating layer. Figure 4 shows the simulation-based impedance response for each of these scenarios. Addition of a small amount of antibody (IgG) above the antigen layer (simulating an antibody-antigen binding response) resulted in a small, insignificant change in impedance. Almost complete coverage of antigen binding to antibody, however, resulted in a significant increase in impedance.

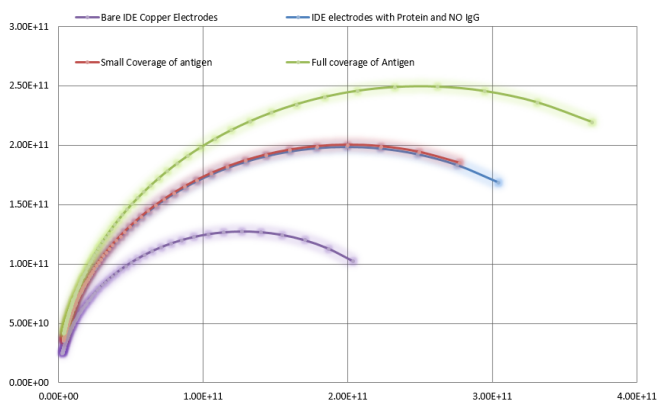


Figure 4. COMSOL simulation results showing the effect of adding antibody and antigen (protein) layers to the IDE on expected impedance  $|Z|$ .

Figures 5 and 6 indicate that the antigen coverage was proportional to a change in impedance. This allows us to precisely select the amount of antigen in the area of the IDE sensor, which, in turn, can be used to determine the level of the COVID-19 virus in the blood.

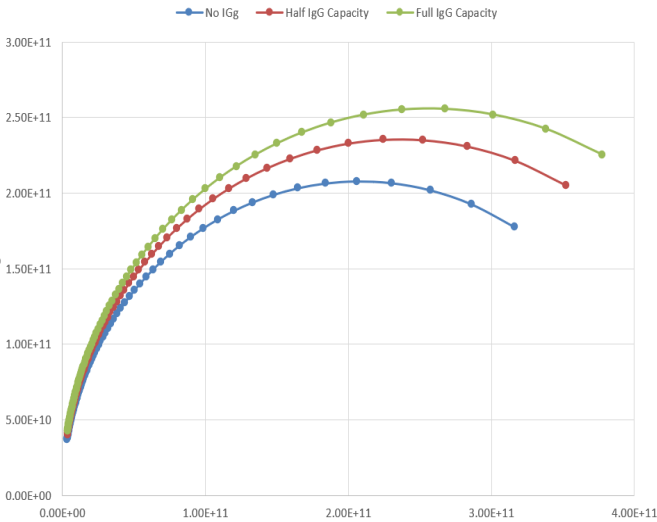


Figure 5. Changes in impedance as a function of antigen coverage area.

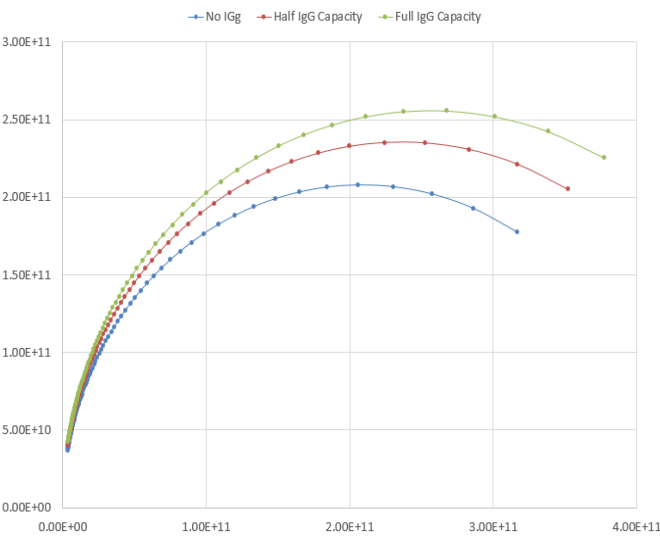
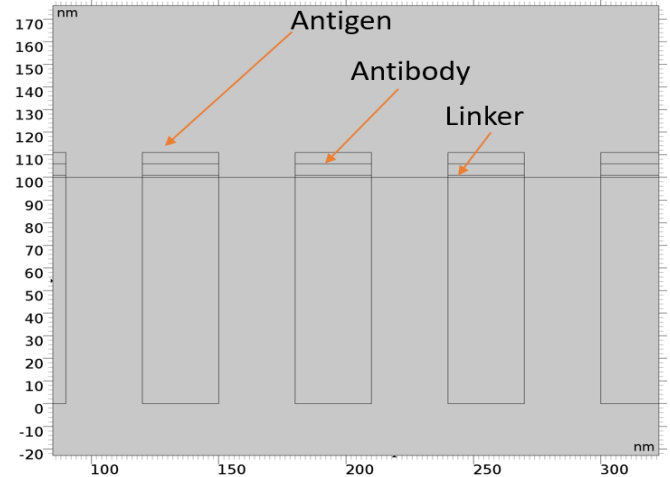
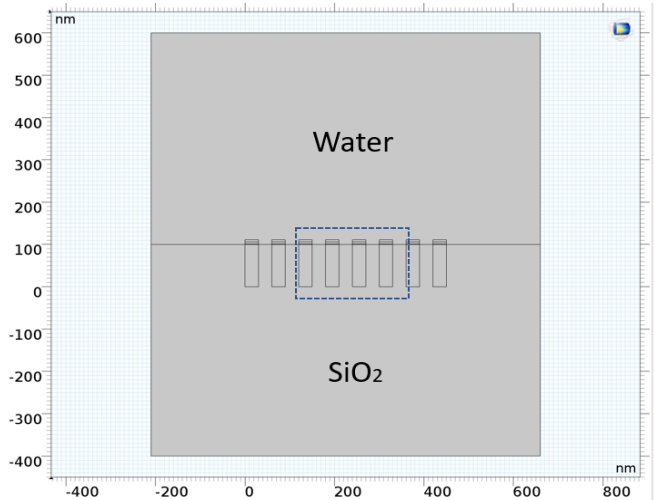


Figure 6. Changes in impedance as a function of antigen coverage area.

Figure 7 shows how the sensor was modeled using 2D and 3D COMSOL simulations. As shown, the antigen layer is above the antibody layer to represent the binding. Different simulation results can be drawn from this 2D model; Figure 8 presents some of these results. Figure 8 also shows the results from the 3D model simulation that prove that adding antigens to the antibodies on the surface of the IDE sensor can be a good representation of the binding by detecting a change in impedance.



(a) 2D simulation.



(b) 3D simulation.

Figure 7. Sensor designs.

Figure 8, the Nyquist plots, shows that impedance increased with more antigens/antibody binding. Fifty percent virus coverage versus full coverage (representing a high quantity of the virus) was simulated. As shown, more virus quantity meant more antigens/antibody bindings, which translated into an increased change in impedance. Figure 8 further shows that the impedance magnitude increased with respect to frequency with more antigens/antibody binding. This was considered solid proof of the concept that the IDE sensors can be used to detect COVID-19 antigens/antibody binding, which is a practical representation of the existence of the virus along with its quantity. Antigen coverage percentage was also studied. The goal was to determine whether the capacity of the antigens would affect the impedance reaction proportionally. Three scenarios were simulated. The first experiment had no antigens present in the IDE sensor. The second experiment had 50% coverage, while the third scenario had a full 100% coverage.

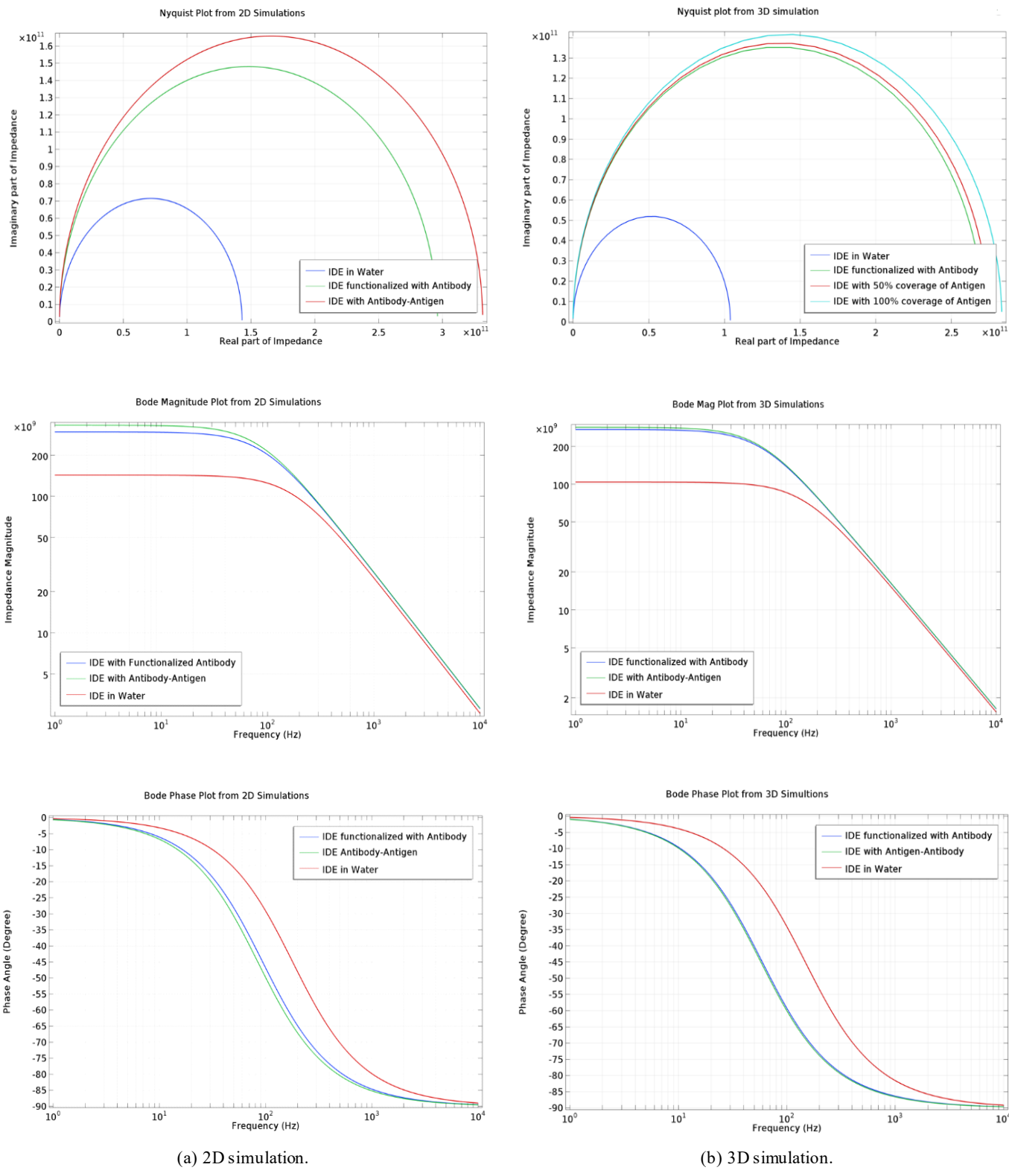


Figure 8. COMSOL simulation results showing the effects of adding antibody and antigen (protein) layers to the IDE on expected impedance.

The dimensions of the IDE electrodes were also studied in order to determine if these dimensions would have an effect on impedance. The IDE electrode width ( $A$ ) and the spacing between electrodes ( $B$ ) were both varied. Nyquist plots were then generated from simulations of these configurations, using a constant amount of antibody and antigen. Figure 9 shows that the IDE electrode width ( $A$ ) was increased to 2x, 4x, and 8x the initial reference width. The resulting impedance values decreased with increasing electrode width. When the spacing between the electrodes was modified (2x, 4x, and 8x the initial reference), the resulting overall impedance of the sensor increased.

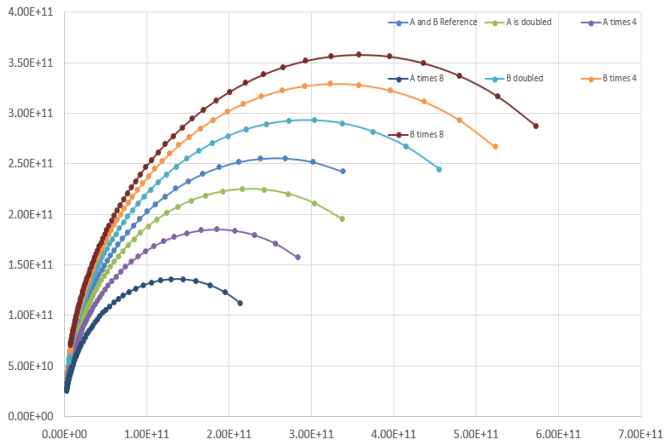


Figure 9. Changes in impedance as a function of modulating IDE dimensions.

Moreover, the dimensions of the entire sensor were studied. This analysis was different from the analysis depicted in Figure 9, since here the entire size of the sensor itself was considered, while in Figure 9, different dimensions of the IDE sensor—such as the distance between electrodes—was the only factor that was changed, while keeping everything else the same without variation. Figure 10 shows that the bigger the overall dimensions of the IDE sensor, the smaller range of impedance variation. One curve (dimensions x10) shows the impedance response when the original dimension of the IDE sensor was scaled 10 times bigger, while the other curve represents the impedance response when the IDE dimension was 100 times bigger. The author recommends having the IDE dimensions be in the nanometer range in order to recognize changes in impedance. Three different proposed device structures were simulated in order to check sensor response and performance. For Device A, Figure 11 shows that the impedance sensor electrode was designed to be inside  $\text{SiO}_2$ .

Figure 12 show that the electrodes for Device B were inside  $\text{SiO}_2$  and on top of the Si substrate, while Figure 13 shows that Device C had its electrodes on top of the  $\text{SiO}_2$  substrate. In the three proposed device structures, these figures show the physical structure for each device, the Nyquist plots, and the Bode plots for both the impedance

magnitudes and angles. In comparison for all three proposed sensor structures and types, Device C showed the highest response on antibody-antigen recognition. Therefore, it is recommended to use the proposed Device C, where its electrodes are on top of the  $\text{SiO}_2$  substrate, when fabricating this IDE sensor to detect the COVID-19 virus.

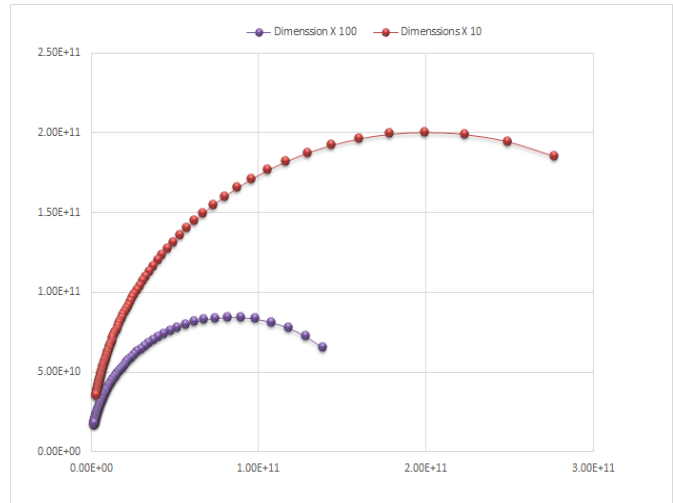


Figure 10. Changes in the size of the sensor.

## Conclusions

These COVID-19 testing methods are not new, but the importance of them is higher than ever before. Optimal testing should be more accurate and, especially, more rapid. Because this virus may be around for years or the foreseeable future, it is critical to make tests as accurate and rapid as possible. This will play a major role in saving lives. In this current study, the author developed an affinity-based impedance sensor model the simulated and tested it using COMSOL Multiphysics software using the electrical AC-DC module as a potential COVID-19 test. The model exhibited the expected response to the addition of biomolecular affinity layers (antibodies) and the subsequent addition of protein-based antigens. A model was developed to simulate impedance-based, antibody-antigen attachments. Based on the simulation results, the author found that impedance changed with more antigens and antibodies binding. This is a proof of concept that the proposed IDE sensor can be used to detect the existence of the COVID virus in the blood.

Different design parameters were studied and simulated. Modulation of IDE electrode size and spacing showed a trend towards lower measured impedance with increasing electrode width. Conversely, increasing the spacing between electrodes was shown to increase measured impedance. Three different sensor structures were proposed and tested. These initial studies will help to guide the design of a nanoscale impedance-based sensing platform to be another effective COVID testing tool. This model predicted the best fabrication process and design considerations.

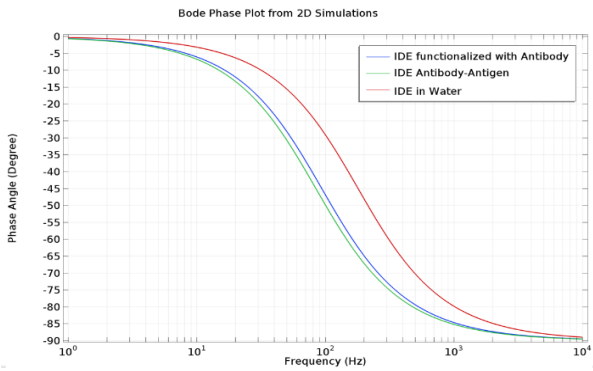
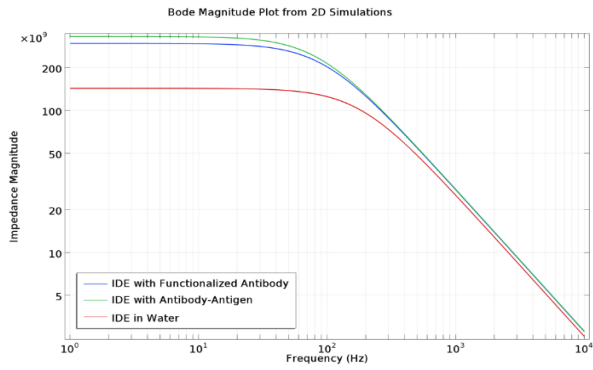
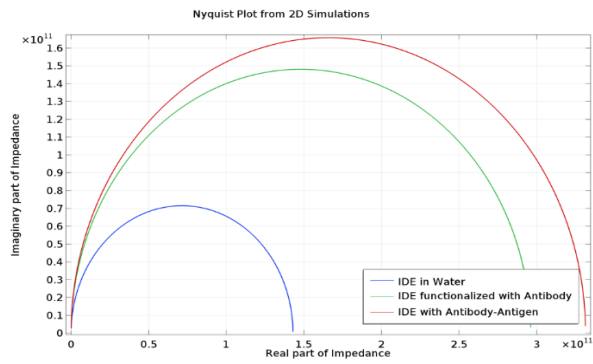
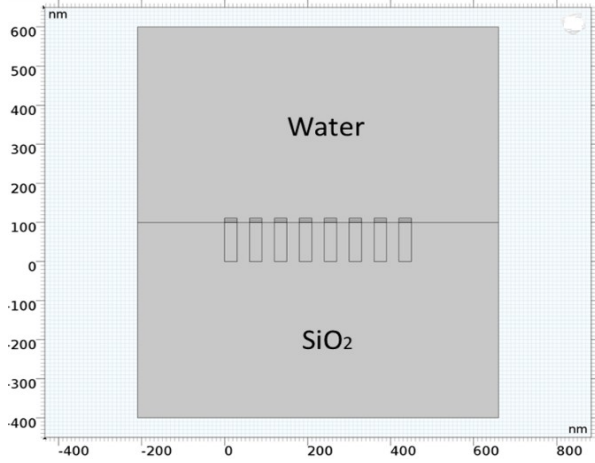


Figure 11. Proposed Device A: structure, Nyquist plot, Bode plots.

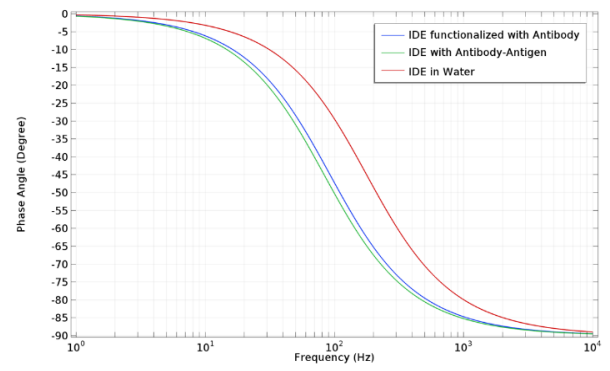
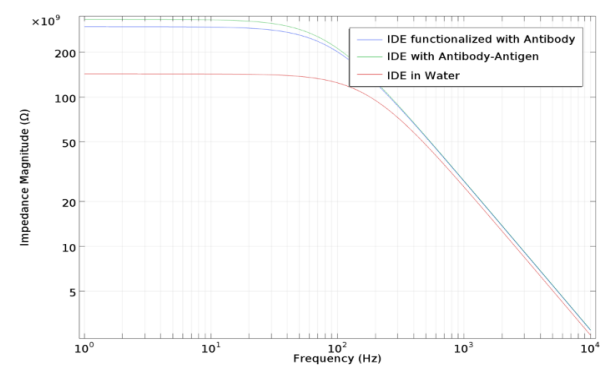
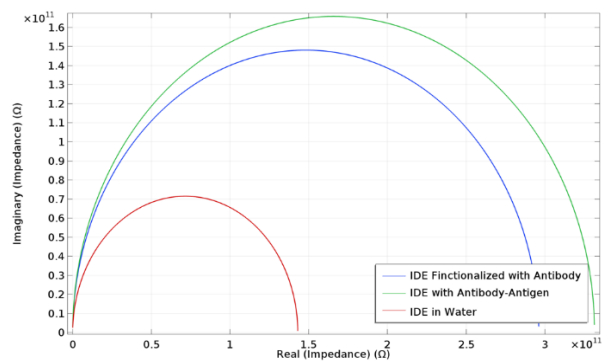
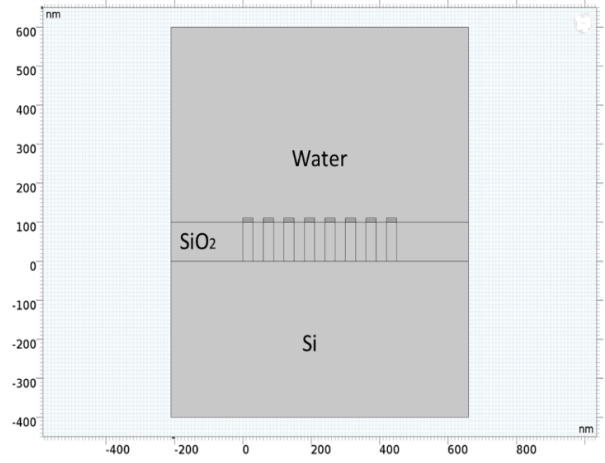


Figure 12. Proposed Device B: structure, Nyquist plot, Bode plots.

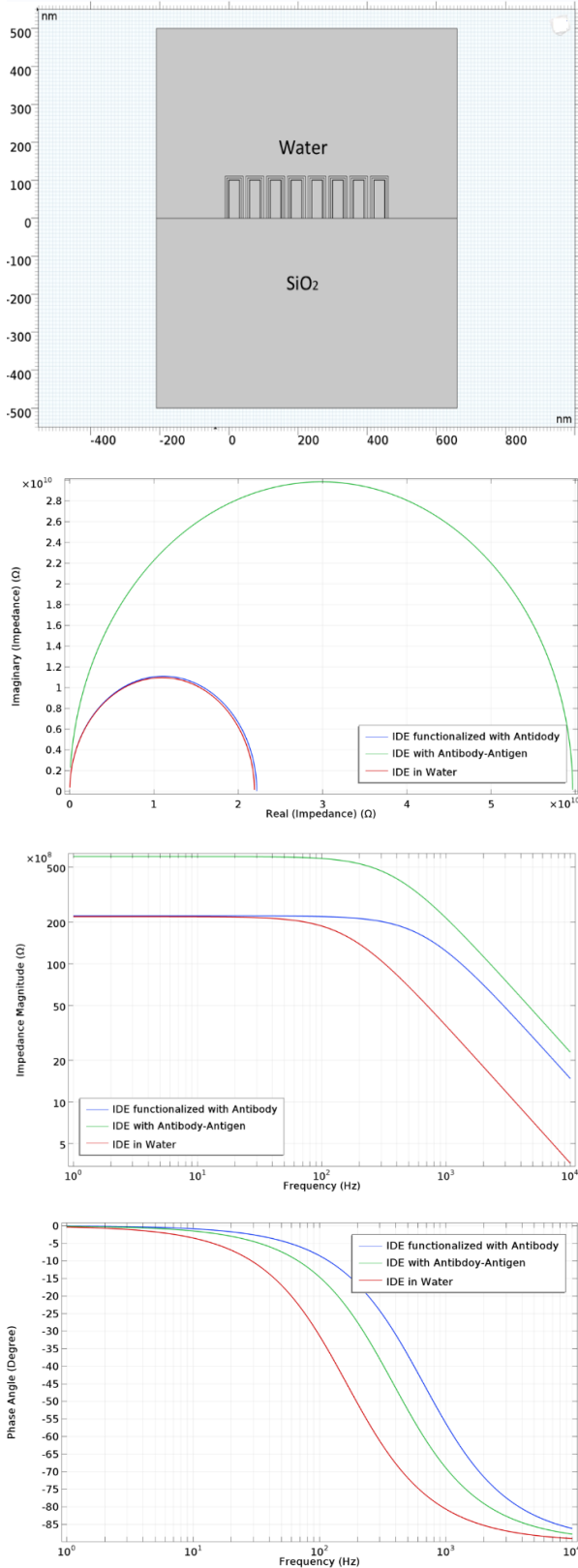


Figure 13. Proposed Device C: structure, Nyquist plot, Bode plots.

## References

- Abdallah, M. (2021). Design, Simulation, and Development of a BioSensor for Viruses Detection using FPGA. *IEEE Journal of Translational Engineering in Health and Medicine*, 9, 1-6.
- Ahn, J., Lee, T., Li, T., Heo, K., Hong, S., & Ko, J. (2011). Electrical immunosensor based on a submicron-gap interdigitated electrode and gold enhancement. *Biosensors*, 26, 4690-4696.
- Binachi, E., Francesco, M., Enrica, R., Gabriele, D., & Carlotta, G. (2012). *Model of an Interdigitated Electrodes System for Cell Counting Based On Impedance Spectroscopy*. Proceedings of COMSOL conference at Milan.
- Chen, J., Fang, Z., Liu, J., & Zeng, L. (2012). A simple and rapid biosensor for ochratoxin A based on a structure-switching signaling aptamer. *Food Control*, 25, 555-560.
- Fraden, J. (1997). *Handbook of Modern Sensors*; American Institute of Physics: Woodbury, New York, 1997.
- Manickam, A., Chevalier, A., McDermott, M., & Ellington, A. (2010). A CMOS Electrochemical Impedance
- Radke, S., & Alcolija, E. (2004). Design and fabrication of a microimpedance biosensor for bacterial detection. *IEEE Journals of Sensors*, 4, 434-440.
- Spectroscopy (EIS) Biosensor Array. *IEEE Transactions on Biomedical Circuits Systems*, 4, 379-390.
- Whittington, R., Muessig, D., Reddy, R., Mohammad, A., Mitchell, K., Brumbaugh, J. ... Hayes, D. (2020). Temperature monitoring with an implantable loop recorder in a patient with presumed COVID-19. *Heart Rhythm*, 6(8): 477-481.
- Zeng, X., Shen, Z., & Mernaugh, R. (2012). Recombinant antibodies and their use in biosensors. *Analytical and Bioanalytical Chemistry*, 402, 3027-3038.

## Biography

**MOHAMMED ABDALLAH** is an associate professor in the Engineering College at the State University of New York Polytechnic Institute. He served as the program coordinator for eight years and the department chair for two years. His current research interest is hardware systems in nanobiosensor applications. He is a senior member of the IEEE and has published more than fifty conference papers and journal articles. Dr. Abdallah may be reached at [abdallm@sunypoly.edu](mailto:abdallm@sunypoly.edu)



# CHARACTERIZATION OF ELECTRICAL WAVEFORMS IN TRANSCUTANEOUS ELECTRICAL NERVE STIMULATORS FOR PERSONAL USE

Albert Lozano-Nieto, The Pennsylvania State University, Wilkes-Barre

## Abstract

Transcutaneous electrical nerve stimulation (TENS) can be used to reduce pain without needing pharmacological drugs or invasive clinical intervention. TENS is based on applying electrical currents with different waveforms to the muscles being targeted for pain relief. This technique was initially developed for use in a medical environment in which clinicians examined the optimal current waveforms at specific body locations. TENS has recently expanded for at-home-use without clinical intervention. Contrary to clinical TENS units, the waveforms for at-home-use are not disclosed. In this current study, the author investigated these waveforms and found a strong variability in their characteristics. This study also addressed potential safety concerns related to their use.

## Introduction

Chronic pain is one of the most common reasons for seeking medical help, either for specific injuries or generalized pain, especially in developed countries. Transcutaneous electrical nerve stimulation (TENS) has been proposed as a non-invasive, inexpensive, safe, and easy-to-administer technique focused on its management without the need for drugs or physical therapy. Additionally, TENS is used in rehabilitation to enhance muscle strength and generate stronger functional movements. TENS can be used either alone or coadjutant with other techniques such as therapeutic exercises, massage therapy, and spa therapy, tailored to the specific areas of the body seeking relief. TENS involves the application of pulsating electrical current to the targeted region by means of two or four electrodes. These stimulate muscular tissue by provoking desired involuntary contractions. This electrical current varies in its intensity, frequency of the pulse, duration of the pulse, and waveform shape.

While the full understanding underlying electrophysiology of TENS is still under debate (Chen, Tabasam & Johnson, 2008), it is known that it is based on the electrical stimuli depolarizing peripheral nerve membranes and generating an induced nerve impulse. This, in turn, modulates the flow of nociceptive impulses in central or peripheral nervous systems, thereby reducing pain (Kitchen & Bazin, 2007). However, the review of the literature regarding the effectiveness of TENS in treating chronic pain is inconclusive. As shown in the following literature review, the reported studies have focused on its use in treating specific conditions rather than being generalized.

TENS has traditionally been applied in a clinical setting with the treatment administered by a clinician. Research on the use of TENS has been focused on evaluating its usefulness when added to traditional techniques for pain relief with non-conclusive results. However, it is important to note that its use has been focused on specific areas of the body rather than generalized discomfort. As such, the effectiveness of TENS against osteoarthritis of the knee, which is characterized by chronic knee pain and joint stiffness resulting in the limitation of daily activities of those having it, was studied against spa treatments. Spa treatments have been used for many years to alleviate these symptoms, as they do not involve the use of pharmacological approaches. The results showed no significant differences between these two therapies (Yaşar, Yakşi, Kurul & Baki, 2021). Similarly, Vaillancourt et al. (2019) concluded that the addition of TENS to therapeutical exercises for pain reduction in elderly populations did not contribute to its reduction, when compared to using therapeutical exercises alone. TENS has also been proposed as an alternative to manual therapy to treat patients with chronic neck pain, which is a frequent health problem associated with modern lifestyles. While the use of TENS alone did not show an improvement in neck pain reduction compared to the traditional approach of manual therapy, some improvement was realized when using these two techniques together (Díaz-Pulido, et al., 2021).

A related technique is vagal nerve stimulation (VNS), which involves the use of the TENS device to produce electrical signals in the brain via the vagus nerve, opposed to delivering the signals to muscles as TENS does. Natelson et al. (2021) studied VNS as a possible non-invasive treatment for chronic, widespread pain in Gulf War veterans with Gulf War illness. This affects about a quarter of the veterans deployed to the Persian Gulf during the 1990-91 conflict and is characterized by widespread pain, fatigue, headaches, and difficulty concentrating (Rayhan, Ravindran & Baraniuk, 2013). Although many years have passed since the conflict, the clinical community has only been able to treat those veterans with drugs that have strong side effects. Thus, VNS emerged as their alternative to potentially relieve these symptoms. However, the results of their study using active VNS and sham VNS, concluded there were no significant differences between these two groups.

TENS was proved effective against traditional therapies used to treat pudendal neuralgia, which is one of the most debilitating forms of genital pain (Eid, Rawash, Sharaf & Eladl, 2021). Because traditional therapies involve the use of drugs with serious side effects and can cause blockage of

---

the pudendal nerve or surgical nerve decompression, TENS emerged as a very attractive technique to treat patients with this condition. The results of this study showed a significant decrease in pain for those patients undergoing TENS for a period of at least 12 weeks. TENS has also been proved to be effective against pain of neurophatic, nociceptive, or musculoskeletal origin. It has been successfully used to treat temporomandibular disorders, especially if the positions of the electrodes are somewhat individualized for each patient (Jung, Byun & Choi, 2016).

Other studies were focused on evaluating how the waveforms of the signals affected pain improvement in patients. One study compared alternating medium-frequency current versus pulsed low-frequency current for neuromuscular performance of competitive athletes. The pulsed low-frequency current used in this study was monopolar with a frequency between 1 Hz and 100 Hz and a pulse duration of 500  $\mu$ s, resulting in a duty cycle of 0.05%-1% (Oliveira, Modesto, Bottaro, Babault & Durigan, 2018). Both types of waveforms showed similar results on the performance of quadriceps muscles of athletes. Likewise, similar studies attempting to find the optimal waveform to elicit higher torque with less discomfort for the athletes being treated resulted in non-consensus (Ward, Oliver & Buccella, 2006). One of the traditional types of waveforms used for muscle strengthening is called "Russian current." This waveform uses a frequency between 2000 Hz and 3000 Hz, with bursts lasting 10 ms and delivered at 20- $\mu$ s intervals. Nevertheless, some studies suggest that Russian current created more muscle fatigue compared to other waveforms (Laufer & Elboim, 2008). The clinical community also suggested the use of different types of waveforms for targeted situations rather than the commonly used Russian current (Bellew, Sanders, Schuman & Barton, 2013). While most TENS applications use surface electrodes, electrical stimulation using needle electrodes has also been used for nerve location during peripheral nerve blockade (Tsui, 2008). This is one of the few invasive applications of TENS that requires application in a sterile environment, thus limiting its use.

Recently, TENS devices have been marketed for at-home use by the general public as pain relief units without having to travel to a clinic. This is limited by users not being aware of the optimal placement of the electrodes, problems with their adherence to the skin, and electrode placement not easily accessible, such as on an individual's back. Furthermore, because the manufacturers and vendors of these at-home TENS devices use enticing names for their different modes of operation (kneading, acupuncture, deep massage, etc.), users may have a false sense of expectation in their results. It is also important to note that because manufacturers do not disclose the waveform characteristics of these different modes of operation, it is difficult to compare them to the TENS units used in a clinical setting (ca.dth.ca, 2021). A final area of concern is that users may not be aware of the conditions for which TENS is not suitable for them or the contraindications on their use (Wright, 2012).

It was not the goal of this study to contribute to the discussion as to whether TENS is an effective technique for relieving pain. Instead, and given the lack of information describing the characteristics of the waveforms used in at-home TENS units, the author aimed to characterize them for further studies. The focus was on determining parameters such as waveform envelope, frequencies, intervals between pulses, maximum current delivered among other variables within their different modes of operation.

## Methods

The study described in this paper characterizes the waveforms generated by a TENS unit (Nursal Model AS1080) purchased from a popular online retailer. This unit is marketed for personal, at-home use for massage and pain relief and is operated by a rechargeable lithium battery. This TENS unit has six different modes of operation, which are named after therapeutical massage techniques such as kneading, acupuncture, cupping, tapping, shiatsu-deep, and auto combination from the previous modes of operation. Within each mode of operation, the user can select from two to four different sub-modes that also have distinctive names listed in operating manual. The unit contains a set of different electrode pads, each one having a unique surface area. Electrode surface area influences the current density injected into the muscles for skin adhesion, distance between electrodes, and their impedance also have a direct effect on the current density and, therefore, muscular contraction.

In reporting the results of this current study, the author used the convention "sub-mode X-Y" in which X represents one of the six modes named above and Y represents a given sub-mode within mode X. For example, sub-mode 1-4 represents sub-mode 4 from mode 1 (kneading). Users of this device can select from different levels of intensity that are displayed in the units by a bar graph increasing from left to right. Voltage levels were neither specified in the instructions booklet nor were found elsewhere. In this investigation, the author measured and recorded the open-circuit waveform and its characteristics for each sub-mode using a Rigol oscilloscope model DS1074. This is a digital sample oscilloscope (DSO) with a bandwidth of 70 MHz, a maximum sample rate of 1GSa/s, and a maximum memory depth of 24 Mpts. These specifications were sufficient for the needs of this study.

The equivalent Thévenin model of this unit was found using traditional methods assuming the TENS unit is a "black box" with only access to its output terminals. The Thévenin equivalent voltage (open-circuit voltage) corresponds to the maximum voltage listed in Appendix. The author noted that the Thévenin equivalent resistance varied within 12% for changing modes and sub-modes of operation. Its average value was found to be 6 k $\Omega$ . This change can be attributed to the variety of periods between pulses stated and, therefore, frequency of operation listed in the Appendix.

When changing modes or sub-modes of operation, the amplitude of the TENS unit reverts to its minimum value for the safety of the user. For this reason, prior to recording the waveform and its electrical characteristics, the amplitude was increased to its maximum value. This allowed a clear comparison among the different modes or sub-modes of operation.

## Results: Basic and Fundamental Pulses

Figure 1 shows that the initial waveforms were based on a combination of the same bi-phasic pulses. These pulses had a total period of 0.75 ms, with their amplitude dependent on the strength chosen by the user.

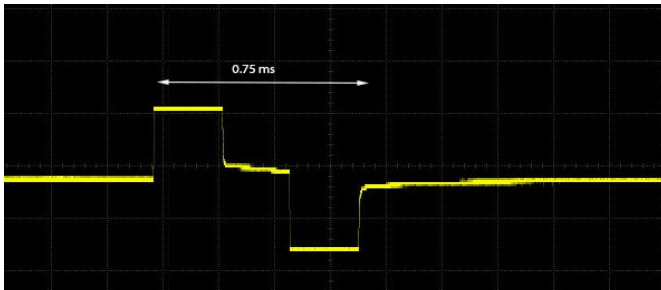


Figure 1. Basic bi-phasic pulse.

The author of this current study also found the following parameters for each signal generated by this unit: (a) type of waveform as defined by its envelope; (b) time duration for a give waveform; (c) time between consecutive waveforms; (d) period between consecutive pulses; and, (e) maximum open-circuit voltage. The specific data values for each mode and sub-mode are summarized in Table 1 in the Appendix. Figure 2 shows how the waveforms generated by each sub-mode can be broadly classified into four different groups, depending on their pattern: 1) burst signals in which the amplitude of the pulses varies during the burst time; 2) signals in which the amplitude remains constant; 3) continuous, modulated signals; and, 4) other types of signals. When reviewing Table 1 and Figure 2, it is important to note that different sub-modes within a given mode may not result in the same type of waveform; in fact, for most modes, the waveforms for each sub-mode were vastly different.

### Mode 1

In Figure 2, the waveforms generated by sub-modes 1-1, 1-2, and 1-4 follow pattern signal (A), while sub-mode 1-3 follows pattern (D). Figure 3 shows that sub-modes 1-1 and 1-2 differ from each other only in the period between consecutive pulses, with the duration of the burst and the time between bursts remaining the same. Figure 3 also shows that the burst from sub-mode 1-1 was shorter than the burst from sub-mode 1-2, the reason for which was the need to trigger the oscilloscope before the signal from sub-mode 1-1 was finished. The data from Table 1 shows that the burst time for both signals was the same.

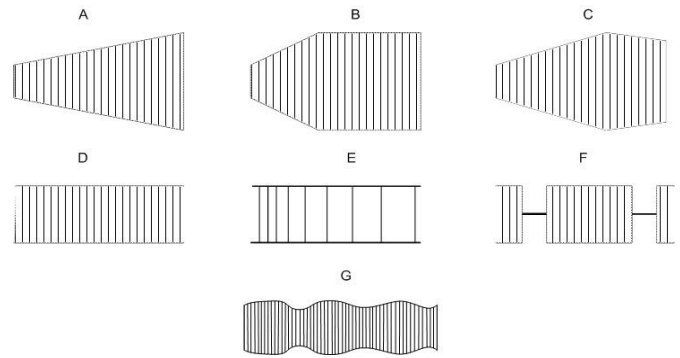


Figure 2. Generalized types of generated waveforms. The vertical lines represent the bi-phasic pulses.

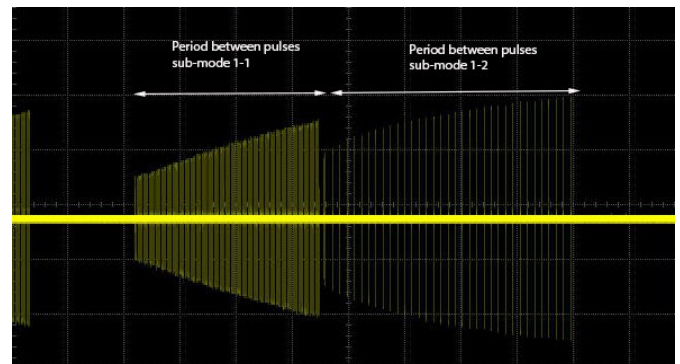


Figure 3. Burst transition between sub-modes 1-1 and 1-2.

Figure 3 shows that the interval between consecutive pulses for sub-mode 1-1 (25 ms) was much shorter than for sub-mode 1-2 (125 ms). The burst signal for sub-mode 1-4 (not depicted in Figure 3) had the same period between consecutive pulses as sub-mode 1-1 (25 ms); however, its burst time of 1 second was much shorter than the burst time for sub-modes 1-1 and 1-2 (4 seconds). Furthermore, the times between bursts were also different. The table in the Appendix displays the specific differences between these sub-modes. The waveform pattern generated by sub-mode 1-3 (pattern D in Figure 2) was different from the waveforms generated by the other sub-modes, and also generated a waveform with constant amplitude pulses and a period between them of 710 ms. Table 1 shows that each of these sub-modes had different open-circuit voltages and, therefore, the intensity of the current for a given setting was different. Given that the resistance between electrode pads remained constant when changing sub-modes, the maximum current delivered by sub-modes 1-1, 1-2, and 1-4 was 30 % greater than the maximum current delivered in sub-mode 1-3.

### Mode 2

Figure 1 further shows how mode 2 in this unit was the only mode based on the generation of two consecutive bi-phasic pulses. This, in turn, created a total pulse width for this mode of 1.5 ms. Figure 4 shows that sub-modes 2-1 and 2-2 generated waveforms with constant amplitude, corre-

responding to pattern (E) from Figure 2. They differ in the period between pulses, which varied from 35 ms to 350 ms for sub-mode 2-1, and from 80 ms to 600 ms for sub-mode 2-2.

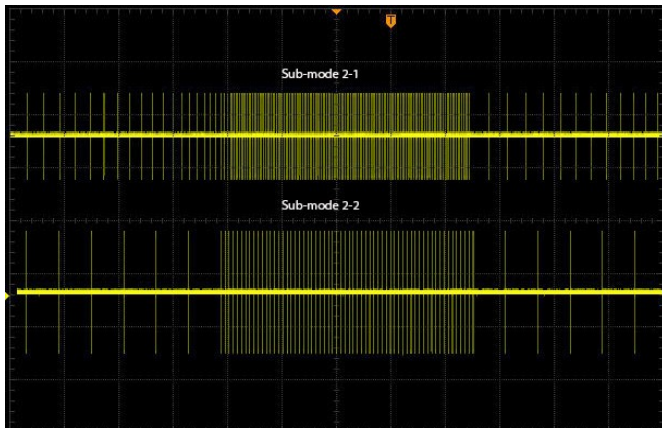


Figure 4. Pulse differences between sub-modes 2-1 and 2-2.

Figure 4 shows that, for the same intensity setting in the TENS unit, the signal amplitude for sub-mode 2-2 was approximately 11% higher than for sub-mode 2-1. The maximum open-circuit voltage for sub-mode 2-1 was 270V, while sub-mode 2-2 was 300V. Sub-mode 2-3 followed waveform pattern (B) from Figure 2. This was another case in which sub-modes within the same mode originated from different signals. For sub-mode 2-3, the amplitude of the pulse increased by 75% until it remained constant with a total duration burst of 4 s.

### Mode 3

Contrary to the rest of the modes for this TENS unit, all of the sub-modes in Mode 3 generated the same general waveform pattern, which is (C) from Figure 2. This waveform is characterized by an increase in amplitude followed by a decrease, although the final amplitude was greater than the initial amplitude. For all three sub-modes, the amplitude of the signal increased by 170%. The period between consecutive pulses also remained constant at 25 ms for all sub-modes. These three sub-modes differed in the time needed to reach the maximum amplitude and also the time between the maximum amplitude and the end of the burst. Figure 5 shows the differences between sub-modes 3-1 and 3-2, while Figure 6 shows the differences between sub-modes 3-1 and 3-3.

### Mode 4

The two sub-modes from Mode 4 generated very different waveforms. Sub-mode 4-1 followed waveform pattern (D), while sub-mode 4-2 followed waveform pattern (G) from Figure 2. Sub-mode 4-1 generated pulses with a period of 2.5 ms and a constant open-circuit amplitude of 90V. This

was the sub-mode that generated the lowest voltage amplitude and, therefore, the lowest maximal current. Figure 7 shows that the waveform generated by sub-mode 4-2 is unique, compared to all of the other waveforms. The amplitude to pulses varied within 30% with a period between pulses of 1.5 ms, which was the shortest period for all of the waveforms in this unit.

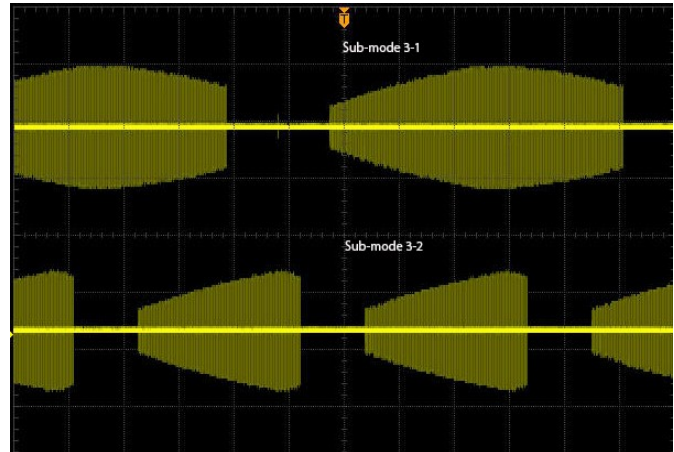


Figure 5. Differences between sub-modes 3-1 and 3-2.

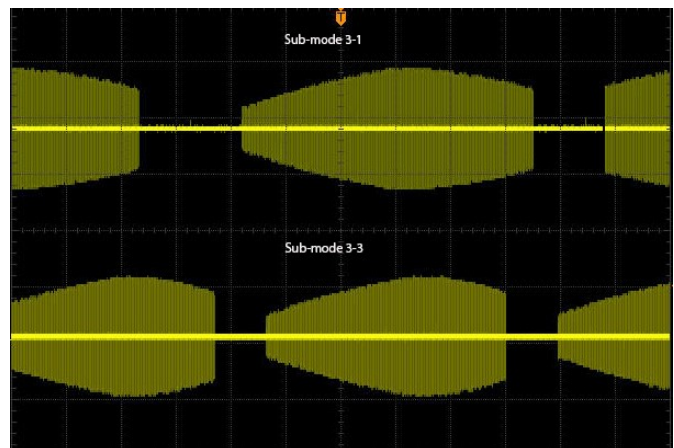


Figure 6. Differences between sub-modes 3-2 and 3-3.

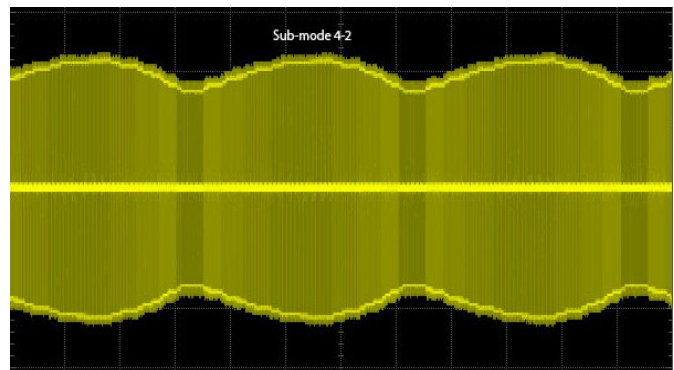


Figure 7. Amplitude-modulated waveform for sub-mode 4-2.

## Mode 5

The waveform generated by sub-mode 5-1 followed pattern (C), a pattern also generated by Mode 3. The amplitude of the pulses in sub-mode 5-1 changed by 150%, which was lower than the 170% change for Mode 3. The waveform generated by sub-mode 5-2 followed waveform pattern (A), with the pulse amplitude changing by 170%. In this case, the time between pulses and burst duration were the same as for sub-modes 1-1 and 1-2.

## Mode 6

The operating booklet for this TENS unit states that Mode 6 is a combination of signals generated from other modes, although it does not specify which ones. Sub-mode 6-1 generated a signal with waveform pattern (D) from Figure 2. This sub-mode had a period between consecutive pulses of 2.2 ms. Figure 8 shows that the signal generated by sub-mode 6-2 corresponds to waveform pattern (F) and is unique among the other sub-modes. This signal consisted of a train of pulses of equal amplitude, lasting 140 ms with a period of 40 ms between trains of pulses. Both sub-modes 6-1 and 6-2 generated the lowest maximum voltage (90V), which was the same value as for sub-mode 4-1. The analysis of these two signals from Mode 6 does not support the statement that Mode 6 is a combination of other sub-modes.

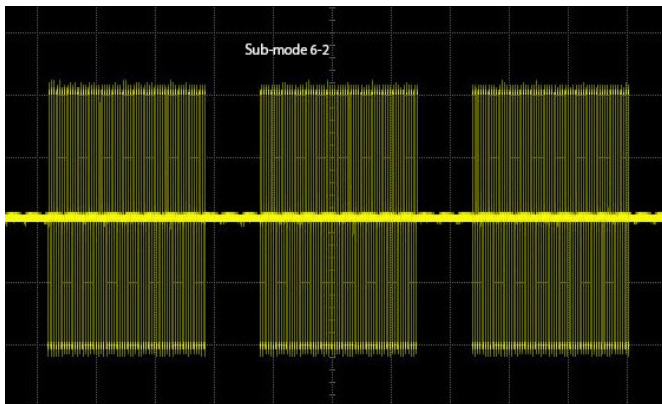


Figure 8. Train of pulses generated by sub-mode 6-2.

## Discussion

The analysis for these signal showed that they were all based on a combination of the 0.75 ms bi-phasic pulses shown in Figure 1. Bi-phasic waveforms have been proved to require a lower peak current to reach the same level of sensory threshold, when compared to mono-phasic signals (Kantor, Alon & Ho, 1994). Furthermore, the existence of an interphase interval (zero voltage between positive and negative pulses) results in a requirement of even lower peak voltages for the same amount of muscle stimulation (Field-Fote, Anderson, Robertson & Spielholz, 2003).

The waveforms generated by this TENS unit differed from each other in the type of burst, total burst time, time between bursts, period between consecutive pulses, and whether the amplitude of the pulses changed or remained constant. Furthermore, the most common type of waveform patterns generated by this unit followed patterns A, B, and C, accounting for 50% of all the waveforms generated. Signals with constant amplitude from waveform patterns D and E accounted for 31%, while the rest of the signals (patterns F and G) were unique to a single sub-mode. Aldayel, Jubeau, McGuigan, and Nosaka (2010) used similar types of burst patterns to compare the effects of alternating current versus pulsed current on muscular responses focusing on torque output, skin temperature, blood lactate, and hormonal responses for electrodes placed on the leg. For these bi-phasic pulses, with parameters similar to those evaluated in this current study, no significant differences were found in the current levels for which volunteers experienced muscle soreness.

The maximum open-circuit voltage in this TENS unit ranged from 90V-300V. Four different sub-modes generated the signals with a maximum amplitude of 300V, while three sub-modes generated the signals with the lowest amplitude of 90V. It is not possible to estimate the current density, as this depends on the location of the electrode pads, their area, the distance between them, and environmental conditions such dry or wet skin, which widely vary even for the same setting. Despite these relatively high voltages, the total energy delivered to the muscles, which can be estimated by integrating the area under the signals, remained low, due to a small duty cycle of the total waveform. The highest duty cycle was found to be 50%, which corresponded to sub-modes that generated the lowest maximum open-circuit voltage.

The table in the Appendix shows an unexpected finding from this study: that the different sub-modes within a specific mode generated vastly different signals. The instruction booklet does not address this topic. In addition, it is important to note that, when changing modes or sub-modes, the signal amplitude drops to its minimum value in order to prevent the user from receiving higher-than-expected amounts of current. It is necessary to point out that the waveforms and their characteristics summarized in this study correspond to a single commercial TENS unit for at-home use. However, based on the types of waveforms reported in the literature, it is reasonable to expect that other TENS units generate similar signals.

## Conclusions

The TENS unit in this study was marketed for at-home use and generated a total of 16 different waveforms. All of them were based on a combination of bi-phasic pulses with a total period of 0.75 ms, as they require the lowest current level to reach the same amount of muscle stimulation. The 16 different waveforms differed from each other in their

patterns, total repetition period, the ratio of change for the signal amplitude, period between consecutive pulses, and whether the signals were based on single or double biphasic pulses. While the manufacturers of at-home TENS units do not disclose the characteristics of the signals generated by their units, it is reasonable to expect that all are similar to those described in this paper.

Individuals interested in using a TENS unit should verify that the device they intend to use is approved by the FDA rather than just listed or registered with the FDA, which is a critical difference (Godman, 2021). A list of all approved devices for home use is available on the FDA website for consultation (Devices@FDA). A final factor to consider is the potential risk that these TENS units may pose to the public, especially for users with implanted electronic devices such as pacemakers. Additional potential hazardous applications are their use in individuals with poor circulation, swelling of the legs and a history of blood clots, as well as nerve damage derived from muscle contractions. All situations in which individuals should not use a TENS unit are clearly listed in the instruction booklet. However, the risk assessment of using at-home TENS devices is beyond the scope of this paper.

## References

- Aldayel, A., Jubeau, M., McGuigan, M., & Nosaka, K. (2010). Comparison between alternating and pulsed current electrical muscle stimulation for muscle and systemic acute responses. *Journal of Applied Physiology*, 109(3), 735-744. doi:10.1152/jappphysiol.00189.2010.
- Bellew, J. W., Sanders, K., Schuman, K., & Barton, M. (2013). Muscle force production with low and medium frequency burst modulated biphasic pulsed currents. *Physiotherapy Theory and Practice*, 30(2), 105-109. doi:10.3109/09593985.2013.823582.
- Cadth.ca. Home Transcutaneous Electrical Nerve Stimulation for Chronic Pain: A Review of the Clinical Effectiveness. (2016). *Canadian Agency for Drugs and Technologies in Health*. Retrieved from [https://www.cadth.ca/sites/default/files/pdf/htis/2016/RC0832\\_TENS\\_Final.pdf](https://www.cadth.ca/sites/default/files/pdf/htis/2016/RC0832_TENS_Final.pdf)
- Chen, C., Tabasam, G., & Johnson, M. I. (2008). Does the pulse frequency of transcutaneous electrical nerve stimulation (TENS) influence hypoalgesia? *Physiotherapy*, 94(1), 11-20. doi:10.1016/j.physio.2006.12.011.
- Devices@FDA. (n.d) Retrieved from <https://www.accessdata.fda.gov/scripts/cdrh/devicesatfda/index.cfm>
- Díaz-Pulido, B., Pérez-Martín, Y., Pecos-Martín, D., Rodríguez-Costa, I., Pérez-Muñoz, M., Calvo-Fuente, V. ...Barco, Á. A. (2021). Efficacy of Manual Therapy and Transcutaneous Electrical Nerve Stimulation in Cervical Mobility and Endurance in Subacute and Chronic Neck Pain: A Randomized Clinical Trial. *Journal of Clinical Medicine*, 10(15), 3245. doi:10.3390/jcm10153245.
- Eid, M. M., Rawash, M. F., Sharaf, M. A., & Eladl, H. M. (2021). Effectiveness of transcutaneous electrical nerve stimulation as an adjunct to selected physical therapy exercise program on male patients with pudendal neuralgia: A randomized controlled trial. *Clinical Rehabilitation*, 35(8), 1142-1150. doi:10.1177/0269215521995338.
- Field-Fote, E. C., Anderson, B., Robertson, V. J., & Spielholz, N. I. (2003). Monophasic and biphasic stimulation evoke different responses. *Muscle & Nerve*, 28(2), 239-241. doi:10.1002/mus.10414.
- Godman, H. (2021, July 01). Are home pain relief gadgets safe for use? Retrieved from <https://www.health.harvard.edu/pain/are-home-pain-relief-gadgets-safe-for-use>
- Jung, J., Byun, J., & Choi, J. (2016). Basic Understanding of Transcutaneous Electrical Nerve Stimulation. *Journal of Oral Medicine and Pain*, 41(4), 144-154. doi.org/10.14476/jomp.2016.41.4.145.
- Kantor, G., Alon, G., & Ho, H. S. (1994). The Effects of Selected Stimulus Waveforms on Pulse and Phase Characteristics at Sensory and Motor Thresholds. *Physical Therapy*, 74(10), 951-962. doi:10.1093/ptj/74.10.951.
- Kitchen, S., & Bazin, S. (2007). *Electrotherapy: Evidence-based practice*. Edinburgh: Churchill Livingstone.
- Laufer, Y., & Elboim, M. (2008). Effect of Burst Frequency and Duration of Kiloherz-Frequency Alternating Currents and of Low-Frequency Pulsed Currents on Strength of Contraction, Muscle Fatigue, and Perceived Discomfort. *Physical Therapy*, 88(10), 1167-1176. doi:10.2522/ptj.20080001.
- Natelson, B. H., Stegner, A. J., Lange, G., Khan, S., Blate, M., Sotolongo, A. ...Helmer, D. A. (2021). Vagal nerve stimulation as a possible non-invasive treatment for chronic widespread pain in Gulf Veterans with Gulf War Illness. *Life Sciences*, 282, 119805. doi:10.1016/j.lfs.2021.119805.
- Oliveira, P., Modesto, K., Bottaro, M., Babault, N., & Durigan, J. (2018). Training Effects of Alternated and Pulsed Currents on the Quadriceps Muscles of Athletes. *International Journal of Sports Medicine*, 39(07), 535-540. doi:10.1055/a-0601-6742.
- Rayhan, R. U., Ravindran, M. K., & Baraniuk, J. N. (2013). Migraine in gulf war illness and chronic fatigue syndrome: Prevalence, potential mechanisms, and evaluation. *Frontiers in Physiology*, 4. doi:10.3389/fphys.2013.00181.
- Tsui, B. C. (2008). Electrical Nerve Stimulation. *Atlas of Ultrasound and Nerve Stimulation-Guided Regional Anesthesia*, 9-18. doi:10.1007/978-0-387-68159-7\_2.
- Vaillancourt, S., Coulombe-Lévêque, A., Fradette, J., Martel, S., Naour, W., Silva, R. A., & Léonard, G. (2019). Combining transcutaneous electrical nerve stimulation with therapeutic exercise to reduce pain in an elderly population: A pilot study. *Disability and Rehabilitation*,

- 
- 43(15), 2141-2148.  
doi:10.1080/09638288.2019.1693639.
- Ward, A. R., Oliver, W. G., & Buccella, D. (2006). Wrist Extensor Torque Production and Discomfort Associated With Low-Frequency and Burst-Modulated Kilo-hertz-Frequency Currents. *Physical Therapy*, 86(10), 1360-1367. doi:10.2522/ptj.20050300.
- Wright, (2012). Exploring the evidence for using TENS to relieve pain. *Nursing Times*, 108(11), 20-23.
- Yaşar, M. F., Yakşi, E., Kurul, R., & Balcı, M. (2021). Comparison of outpatient and inpatient spa therapy in knee osteoarthritis. *International Journal of Biometeorology*, 65(10), 1675-1682. doi:10.1007/s00484-021-02122-z.

## Biography

**ALBERT LOZANO-NIETO** is a professor of engineering at The Pennsylvania State University, Wilkes-Barre campus, and the coordinator of its BS in Electrical Engineering Technology. He earned his BS, MS, and PhD degrees from the Polytechnic University of Catalonia in Barcelona Spain. Dr. Lozano-Nieto's research interests include the characterization of physiological events, use of bioelectrical impedance techniques, and improving education in engineering technology. Dr. Lozano-Nieto may be reached at [ax117@psu.edu](mailto:ax117@psu.edu)

## Appendix

*Table 1.* Summary of the different parameters for the waveforms generated by the TENS unit under study.

Mode	Sub-mode	Waveform	Amplitude increase	Burst time	Time between bursts	Total rep period	Pulse type	Bi-phasic pulse width	Period between pulses	Voltage open circuit
1	1-1	Burst (A)	150%	4 s	2 s	6 s	Single	0.75 ms	25 ms	270 V
	1-2	Burst (A)	100%	4 s	2 s	6 s	Single	0.75 ms	125 ms	270 V
	1-3	Constant (D)	N/A	N/A	N/A	N/A	Single	0.75 ms	710 ms	270 V
	1-4	Burst (A)	100%	1 s	300 ms	1.3 s	Single	0.75 ms	25 ms	190 V
2	2-1	Constant (E)	N/A	N/A	N/A	9.5 s	Double	1.5 ms (2*0.75 ms)	35 ms – 350 ms	270 V
	2-2	Constant (E)	N/A	N/A	N/A	11 s	Double	1.5 ms (2*0.75 ms)	80 ms – 600 ms	300 V
	2-3	Burst (B)	75%	4 s	2 s	6 s	Double	1.5 ms (2*0.75 ms)	25 ms	270 V
3	3-1	Burst (C)	170%	11 s	3 s	14 s	Single	0.75 ms	25 ms	300 V
	3-2	Burst (C)	170%	6 s	2 s	8 s	Single	0.75 ms	25 ms	300 V
	3-3	Burst (C)	170%	9 s	2 s	11 s	Single	0.75 ms	25 ms	300 V
4	4-1	Constant (D)	N/A	N/A	N/A	N/A	Single	0.75 ms	2.25 ms	90 V
	4-2	Modulated G)	30%	N/A	N/A	N/A	Single	0.75 ms	1.5 ms	100 V
5	5-1	Burst (C)	150%	10 s	4 s	14 s	Single	0.75 ms	25 ms	300 V
	5-2	Burst (A)	170%	4 s	2 s	6 s	Single	0.75 ms	25 ms	270 V
6	6-1	Constant (D)	N/A	N/A	N/A	N/A	Single	0.75 ms	2.2 ms	90 V
	6-2	Pulse Train F)	N/A	140 ms	40 ms	180 ms	Single	0.75 ms	2.2 ms	90 V



# STEEL TRUSS DESIGN OPTIMIZATION FOR WEIGHT MINIMIZATION USING A MULTIPLE LINEAR REGRESSION DATA FIT

Michael C. Pickett, Facilities Explosive Safety Mandatory Center of Expertise, AL; Stephen Cotton, Tumkey Processing Solutions, TN

## Abstract

In this study, the authors examined an application of a multiple linear regression data fit to minimize the cost of steel trusses in industrial-type facilities using seven parameters: length (L) (ft.), depth-to-length ratio (D/L) (ft./ft.), panel point spacing (PPS) (ft.), point load (P) (Kips), uniform dead load (w(DL)) (Kips/ft.), uniform live load (w(LL)) (Kips/ft.), and moment (M) (in LRFD) (Kip-ft.). This method provides a useful tool for maximizing efficiency of steel trusses by taking iterative runs of the equation, generated from the data fit, and varying the spatial parameters of the truss to reduce the weight without designing multiple trusses. The lightest truss generated from the iterative takes can then be used as a design starting point. This practice would lead to higher-value engineering savings produced in less time, and safer facilities at a lower cost to owners.

Length (L) was taken as the work point end-to-end length of the truss and depth (D) as the center-to-center of the top and bottom chord members. Panel-point spacing was taken from the working points of the web members. The moments of each truss were taken in LRFD (load and resistance factor design) to account for the increased effect of live loads versus dead loads in truss sizes. With 90 design iterations varying these seven parameters, results were recorded as tons per linear foot (tons/LF), and all of the data were inputted into a 7x90 matrix. The least squares fit of the multiple linear regression data then produced a linear equation that fit the data at an acceptable level. Results showed that an equation for optimization of steel trusses by weight is possible and provides a high correlation to empirical data, as is proven by an  $r^2$  value of 97.11%. Furthermore, the results showed that an improvement to the current industry rule-of-thumb estimate for truss weight can be achieved using this method.

## Introduction

The origin of trusses can be traced back as far as the 16<sup>th</sup> century, but it was in the 17<sup>th</sup> century that methods for analyzing statically determinate trusses were developed by John Bemoulli and Leonard Euler (Gasparini & Provost, 1989). Since then, significant developments have been made in analysis methods and the use of computational software to accelerate the design process; however, even with these new developments, there are certain aspects that software is incapable of optimizing at this time and requires user knowledge

and inputs to accomplish (Zhaochao & Yonggui, 2021). One example is the economical spacing of members and joints. Before available software analyzes a truss, several parameters must be inputted: material strength, length, depth, nodal spacing, boundary conditions, and loads. Taking advantage of the economy of spacing members and nodes can bring value-added engineering and reduce costs of construction for owners (Barthelemy & Hafika, 1993).

## Research Significance

Optimization is generally taken to mean minimizing the effort required or maximizing benefit (Rao, 2020). In this current study, an approximation method was employed that achieved both by creating a tool that reduced design iterations and aided in the selection of economical steel truss designs. Owner representatives have an interest in the intersection of bay size optimization for maximum space for process engineering and the tradeoffs in increased facility cost for larger spans. An approximation tool such as this one provides users with an early planning tool for column layout decisions that are often coordinated with process engineers, as well as other disciplines, in industrial facilities. Industrial facilities can have millions of square feet, in some cases, and, even in cases of smaller footprints, the minute difference of the weight of one truss, repeated throughout the design, can play a substantial role in facility costs.

While the total costs of the truss will also include labor and equipment, RS Means gives these costs as a multiple of linear feet of members that increases as member size increases. Therefore, equipment and labor costs increase with weight as well, though with different scalars. Value engineering is becoming more commonly used and, at times, is even a reimbursable effort when working with the government. This current project highlighted one potential method for optimizing steel truss design to reduce costs without sacrificing efficiency or structural integrity.

In current industry practice, rules of thumb for truss design such as Length-to-Depth (L/D) ratios still require a number of iterations for weight minimization. Small budgets for structural design and hard timelines rarely allow for additional time to be spent producing cost-saving results through strenuous alterations and repeated iterations in design. From this current project, the authors present here an alternative option and a simple mathematically based approach to quickly finding optimum parameters for truss design by minimizing weight on a per-linear-foot basis.

## Materials and Sections

The trusses were designed in RAM Elements software using WT-Sections (a structural steel shape) and double angles. The WT-Sections were given A992 Material Properties and the double angles given A36 Material Properties. WT Sections were selected for top and bottom chords, due to being one common option for industrial-type facility roof trusses and the ease of using the stem as a connection to the web members. A WT 7x19 was selected as the minimum top and bottom chord for truss design, due to the allowance of using the stem as a gusset plate. Web members used were all double angles and kept to a minimum of L 2½" x 2½" x 1/4".

## Analysis

The analysis was performed using 2D Frame Analysis in RAM Elements (structural design and analysis software from Bentley). The steel trusses were modeled matching all material properties. Loads were input and LRFD load cases generated. Figure 1 shows the nodes and member configuration of Truss 1. The end connections of the top chord were pinned and the bottom chord was modeled as a roller in the longitudinal direction. The bottom chord was assumed to be braced in the out-of-plane direction at each location of the web member connections. The web members were assumed to be hinged connections to the bottom and top chords. Parameters were varied in accordance with Table 1 in the RAM Elements software and re-analyzed for each Truss 1-90. Member stress ratios were kept to the limit of 0.90 to allow for slight future increase in loads without the addition of reinforcement. After results were obtained, a matrix was formed using the data of Table 1 and solved using linear regression. The resulting equation was then checked for accuracy using Equation 1:

$$r^2 = 1 - \frac{(y_i - \hat{y}_i)^2}{(y_i - \bar{y}_i)^2} \quad (1)$$

Top chord end nodes were considered as pinned and a roller in the y direction was modeled for bottom chord end nodes. Web members were considered hinged and chord members braced at panel points to reflect bottom chord bracing.

Equation 2 reflects the resulting matrix. Results showed that the use of linear regression was appropriate for generating an approximation equation for the weight of steel trusses. An  $r^2$  value of 97.11% was a high correlation of the approximation equation for expected weights to the actual weights. In addition to comparing the results of Equation 2, the accuracy of the standard rule-of-thumb equation,  $Wt \text{ (lbs/LF)} = (6 \cdot M)/D$ , currently in use (Ioannides & Ruddy, 2000), was compared to the results; it was found that it had a negative  $r^2$  correlation to the actual truss weights. This indicated that it was not an acceptable fit to the data. Table 1 shows that the average error of Equation 2 was 7.05% and maximum error was 21.13%. As the member sizes can drastically fluctuate when a small change in point or uniform load causes an increased section, these results are an acceptable fit to the data.

$$Wt. \left( \frac{Tons}{LF} \right) = L(0.000276) - \frac{D}{L}(0.0883) + PPS(0.000355) + M(0.0000214) + P(0.000247) + WL(DL)(0.0076) + WL(LL)(0.00313) + \left[ \left( \frac{D}{L} - 0.126 \right) * \left( 0.412 * \frac{(L-30) * 0.5 * 2 * (P+8) + 20 * (WL(LL) + 0.8)}{128} \right) \right] \geq 0.0331 \text{ Tons / LF} \quad (2)$$

where,

- L = length of the truss from end-to-end work points
- D/L = depth-to-length, with depth taken center-to-center of the top and bottom chords
- PPS = panel point spacing taken from center-to-center of the vertical web members
- M = LRFD moment
- P = total service point load
- w(DL) = uniform dead load
- w(LL) = uniform live load

Equation 2 was compared to a line of equality with a 20% error in Figure 2 for the 90 steel trusses used in the data set shown in Table 1. This equation is only applicable within the range of each parameter. Conservatively, keeping the variables within the following ranges will ensure more accurate results and lead to lighter trusses.

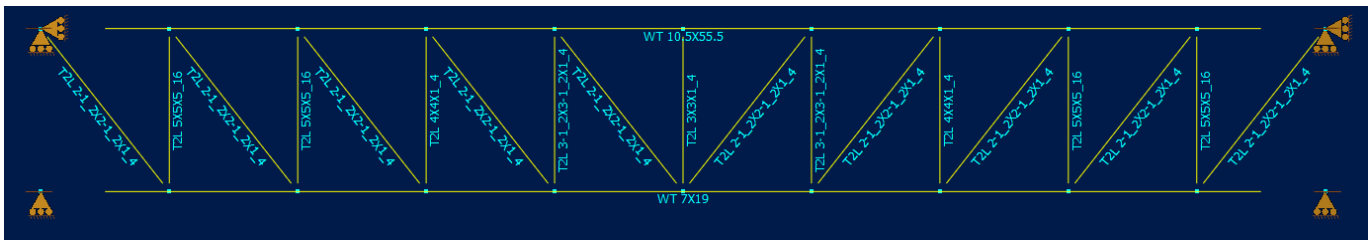


Figure 1. Truss 1 (T1) nodes and members.

Table 1. Steel truss parameters.

Truss	Length (ft.)	Depth-to-length ratio	Panel pt. spacing (ft.)	Pt. load (Kips) (LL)	Uniform load (Kip/ft) w(DL)	Uniform load (Kip/ft) w(LL)	Moment (Kip-ft.)	Weight (tons)	Weight (tons/LF)	Expected (tons/LF)	$\Delta$
T1	50	0.10	8.333	8	0.20	1.50	1305	2.40	0.0480	0.0495	-0.0015
T2	50	0.14	8.333	11	0.20	0.50	985	1.90	0.0380	0.0337	0.0043
T3	50	0.10	8.333	0	0.20	0.70	425	1.77	0.0354	0.0331	0.0023
T4	50	0.06	8.333	7	0.20	0.20	595	2.28	0.0456	0.0369	0.0087
T5	50	0.10	8.333	8	0.00	0.00	480	1.79	0.0358	0.0357	0.0001
T6	50	0.14	8.333	12	0.50	0.60	1208	1.86	0.0372	0.0414	-0.0042
T7	50	0.10	8.333	1	0.25	0.30	304	1.50	0.0300	0.0331	-0.0031
T8	50	0.10	8.333	4	0.20	0.10	365	1.58	0.0316	0.0331	-0.0015
T9	50	0.14	8.333	11	0.60	1.60	1685	2.69	0.0538	0.0560	-0.0022
T10	50	0.10	8.333	2	0.40	1.70	1120	2.30	0.0460	0.0456	0.0004
T11	40	0.08	10	12	0	1.8	960	1.92	0.0480	0.0423	0.0057
T12	40	0.14	10	0	0.1	0.7	248	1.36	0.0340	0.0331	0.0009
T13	40	0.07	10	8	0.6	0	400	1.32	0.0330	0.0331	-0.0001
T14	40	0.13	10	11	0.5	0.9	760	1.48	0.0370	0.0331	0.0039
T15	40	0.13	10	11	0.2	1.2	784	1.53	0.0383	0.0331	0.0052
T16	40	0.13	10	1	0.1	1.3	472	1.36	0.0340	0.0331	0.0009
T17	40	0.13	10	5	0.2	0.4	336	1.12	0.0280	0.0331	-0.0051
T18	40	0.13	10	9	0.6	0	432	1.14	0.0285	0.0331	-0.0046
T19	40	0.07	10	2	0.2	1.1	464	1.53	0.0383	0.0331	0.0052
T20	40	0.13	10	8	0.6	1.7	944	1.62	0.0405	0.0357	0.0048
T21	60	0.07	10	12	0.3	1.8	2322	5.20	0.0867	0.0952	-0.0086
T22	60	0.12	10	0	0.2	0.2	252	1.75	0.0292	0.0331	-0.0039
T23	60	0.10	10	6	0.4	1.4	1656	3.35	0.0558	0.0632	-0.0073
T24	60	0.12	10	9	0.3	0.6	1242	3.07	0.0512	0.0451	0.0061
T25	60	0.12	10	7	0.5	0.8	1350	2.75	0.0458	0.0491	-0.0032
T26	60	0.12	10	10	0.3	0.5	1242	2.77	0.0462	0.0450	0.0011
T27	60	0.14	10	1	0.3	1.5	1314	2.87	0.0478	0.0467	0.0011
T28	60	0.06	7.50	7	0.3	0.6	1266	4.74	0.0790	0.0623	0.0167
T29	60	0.12	7.50	6	0.3	0.3	954	2.45	0.0408	0.0359	0.0049
T30	60	0.13	7.50	9	0.6	1.6	2340	4.44	0.0740	0.0717	0.0023
T31	70	0.10	8.75	8	0.3	0	1117	3.38	0.0483	0.0484	-0.0002
T32	70	0.08	7.00	2	0.3	1.4	1873	5.90	0.0843	0.0778	0.0065
T33	70	0.11	8.75	12	0.4	1.0	2618	5.11	0.0730	0.0823	-0.0093
T34	70	0.11	7.00	6	0.4	0.1	1232	3.58	0.0511	0.0458	0.0053
T35	70	0.11	8.75	7	0.3	0.1	1103	3.22	0.0460	0.0433	0.0027
T36	70	0.14	8.75	4	0.4	1.3	2016	4.62	0.0660	0.0663	-0.0003
T37	70	0.13	7.00	3	0.2	0.6	1155	3.34	0.0477	0.0400	0.0077
T38	70	0.07	8.75	11	0	0.9	2114	5.59	0.0799	0.0880	-0.0081
T39	70	0.07	7.00	2	0.4	0	574	3.03	0.0433	0.0419	0.0014
T40	70	0.09	8.75	5	0.5	1.8	2692	6.29	0.0899	0.1000	-0.0101
T41	80	0.06	10	11	0.6	1.1	3392	10.17	0.1271	0.1358	-0.0087
T42	80	0.08	10	0	0.5	0.5	1120	5.24	0.0655	0.0627	0.0028
T43	80	0.09	10	2	0.1	1.7	2528	6.47	0.0809	0.0966	-0.0158
T44	80	0.12	10	6	0.5	0.7	2144	5.43	0.0679	0.0707	-0.0028
T45	80	0.11	10	4	0.2	0.8	1728	5.00	0.0625	0.0628	-0.0003

Table 1 (cont.). Steel truss parameters.

Truss	Length (ft.)	Depth-to-length ratio	Panel pt. spacing (ft.)	Pt. load (Kips) (LL)	Uniform load (Kip/ft) w(DL)	Uniform load (Kip/ft) w(LL)	Moment (Kip-ft.)	Weight (tons)	Weight (tons/LF)	Expected (tons/LF)	$\Delta$
T46	80	0.06	8.00	6	0.2	0.5	1792	7.59	0.0949	0.0853	0.0096
T47	80	0.08	8.00	1	0.2	1.0	1440	5.61	0.0701	0.0725	-0.0024
T48	80	0.09	8.00	12	0.2	0.4	2624	7.03	0.0879	0.0956	-0.0077
T49	80	0.10	8.00	6	0.1	0.5	1696	5.76	0.0720	0.0656	0.0064
T50	80	0.11	8.00	4	0.6	1.2	2752	8.24	0.1030	0.0890	0.0140
T51	90	0.14	11.25	2	0.3	1.1	2435	6.71	0.0746	0.0813	-0.0068
T52	90	0.08	11.25	5	0.2	1.4	3231	11.19	0.1243	0.1254	-0.0011
T53	90	0.09	11.25	10	0.4	0.3	2412	8.58	0.0953	0.0964	-0.0010
T54	90	0.10	11.25	4	0.5	1.5	3614	9.56	0.1062	0.1215	-0.0152
T55	90	0.11	11.25	3	0.6	0	1161	4.66	0.0518	0.0537	-0.0019
T56	90	0.13	9.00	10	0	0.1	1962	5.86	0.0651	0.0631	0.0020
T57	90	0.08	9.00	0	0.6	1.6	3321	10.78	0.1198	0.1266	-0.0069
T58	90	0.09	9.00	6	0.1	0.3	1688	6.96	0.0773	0.0744	0.0029
T59	90	0.10	9.00	4	0.2	1.3	3069	9.43	0.1048	0.1053	-0.0005
T60	90	0.11	9.00	3	0.4	0	1026	4.77	0.0530	0.0485	0.0045
T61	100	0.06	10	7	0	0.5	2400	11.89	0.1189	0.1152	0.0037
T62	100	0.12	12.50	6	0.5	1.8	5310	17.90	0.1790	0.1505	0.0285
T63	100	0.08	10	10	0.2	0.4	3100	11.96	0.1196	0.1216	-0.0020
T64	100	0.09	12.50	3	0.2	0.7	2180	9.15	0.0915	0.0928	-0.0013
T65	100	0.10	10	2	0.3	1.0	2850	10.25	0.1025	0.1029	-0.0004
T66	100	0.11	12.50	7	0.3	0.6	2770	9.81	0.0981	0.0962	0.0019
T67	100	0.12	10	8	0.3	0.2	2450	8.07	0.0807	0.0808	-0.0001
T68	100	0.14	12.50	4	0.6	1.2	3940	11.78	0.1178	0.1217	-0.0039
T69	100	0.09	10	3	0.3	1.7	4450	13.98	0.1398	0.1511	-0.0113
T70	100	0.11	12.50	10	0.4	0.2	2600	8.82	0.0882	0.0925	-0.0043
T71	110	0.06	11	12	0.25	0.9	5272	24.10	0.2191	0.1987	0.0204
T72	110	0.06	9.17	1	0.1	0.5	1656	11.30	0.1027	0.0954	0.0073
T73	110	0.07	11	9	0.5	1.0	5308	23.42	0.2129	0.1906	0.0223
T74	110	0.13	9.17	0	0.25	1.1	3116	11.47	0.1043	0.0965	0.0078
T75	110	0.08	11	3	0.25	0.4	2082	10.55	0.0959	0.0973	-0.0014
T76	110	0.08	9.17	3	0.25	0.6	2698	11.94	0.1085	0.1123	-0.0038
T77	110	0.09	11	5	0.6	0.8	4125	16.53	0.1503	0.1446	0.0056
T78	110	0.09	9.17	8	0.5	0.1	3262	11.34	0.1031	0.1203	-0.0172
T79	110	0.14	11	10	0.25	1.2	5558	16.39	0.1490	0.1604	-0.0114
T80	110	0.10	9.17	4	0.4	0.4	2750	11.02	0.1002	0.1023	-0.0021
T81	120	0.07	10	5	0.2	0.2	2448	13.50	0.1125	0.1195	-0.0070
T82	120	0.07	12	1	0.2	0.9	3264	16.61	0.1384	0.1432	-0.0048
T83	120	0.14	10	0	0.25	1.3	4284	14.78	0.1232	0.1318	-0.0086
T84	120	0.08	12	1	0.25	1.4	4812	22.44	0.1870	0.1784	0.0086
T85	120	0.08	10	9	0.3	0.3	4104	16.77	0.1398	0.1514	-0.0117
T86	120	0.08	12	11	0.3	1.1	6456	24.84	0.2070	0.2158	-0.0088
T87	120	0.09	10	9	0.25	0.3	3996	16.85	0.1404	0.1424	-0.0019
T88	120	0.09	12	8	0.25	0.2	3036	13.78	0.1148	0.1203	-0.0055
T89	120	0.10	10	5	0.2	1.6	6480	25.21	0.2101	0.1975	0.0126
T90	120	0.12	12	7	0.2	0.2	2688	11.02	0.0918	0.0918	0.0000

- Length 40'-120'
- D/L 0.06-0.14
- PPS 7'-12'
- M 0-6500 Kip-ft
- P 0-12 Kips
- w(DL) 0-0.6 Klf
- w(LL) 0-1.8 Klf

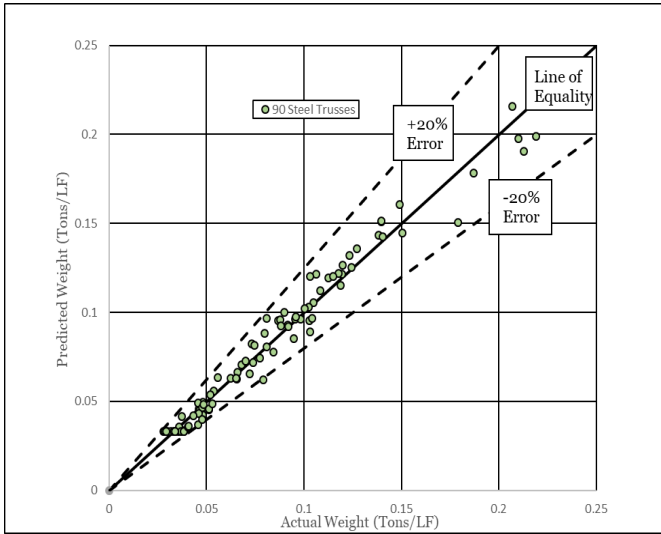


Figure 2. Line of equality comparison.

To illustrate the practical use of this approximation equation and take advantage of its application, consider the following example. A 40,000 sq. ft. facility that is to be square in size with a roof dead load of 20 psf and a roof live load of 25 psf. Ignoring the economy of columns and jack trusses, Equation 2 allows the user to find the most economical grid layout and truss spacing for static vertical loads. Figures 3 and 4 show two of several possible approaches for the grid layout.

The loads and parameters for Grid Layout 1 are:

- Length 100'
- D/L 0.126
- PPS 10'
- M 1000 Kip-ft
- P 1 Kips
- w(DL) 0.2 Klf
- w(LL) 0.25 Klf

And for Grid Layout 2:

- Length 50'
- D/L 0.126
- PPS 5'
- M 125 Kip-ft
- P 0.25 Kips
- w(DL) 0.1 Klf
- w(LL) 0.125 Klf

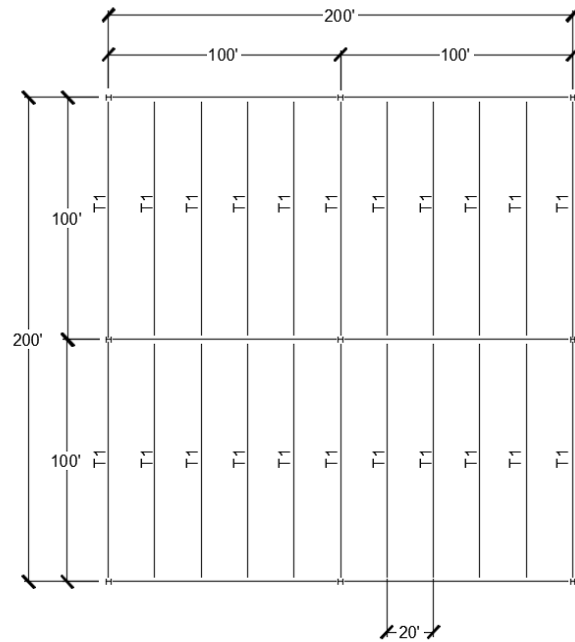


Figure 3. Grid layout 1.

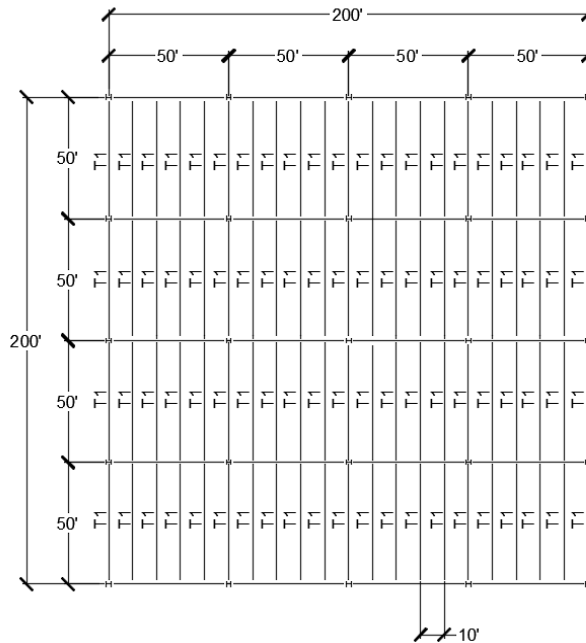


Figure 4. Grid layout 2.

The expected weight from Equation 2 for Grid Layout 1 is 0.0440 tons/LF and 0.0331 tons/LF for Grid Layout 2. Calculating the linear feet of TIs for both layouts gives 2200 feet for Grid Layout 1 and 4200 feet for Grid Layout 2. This produces estimates of 96.8 tons for 100-foot trusses and 139.0 tons for 50-foot trusses. Using Equation 2, the

authors found that a third option of using 50-foot trusses with 20-foot tributary widths would give the lightest steel truss weight at 72.8 tons. The actual weights of these trusses were checked using RAM Elements. The 50-foot trusses with the 10-foot tributary width's actual weight were 0.0302 tons/LF, 9.6% lighter than expected, giving an actual total weight of 126.84 tons. The 100-foot trusses' actual weights were 0.0539 tons/LF, 18.4% heavier than expected, giving an actual total weight of 118.58 tons. The 50-foot trusses with the 20-foot tributary width's actual weight were 0.0312 tons/LF, 6.1% lighter than expected, yielding a total weight of 68.64 tons. The 50-foot trusses with the 20-foot tributary width were 42.12% lighter than the 100-foot trusses with the same spacing. Figures 5 and 6 show the loading and sections. This is just one example of the benefits of utilizing this method. With this information, a facility engineer could give a good estimate of the cost of expanding bay size to compare with the benefits to process engineering of the increased space.

A secondary effort was made to find the optimum depth-to-length ratio, as the initial findings indicated that a rule-of-thumb L/D of 12 or D/L of 0.0833 was far too low. Using 18 of the 90 trusses previously analyzed, one heavily loaded and one lightly loaded for each length increment, the D/L ratio was increased by 0.01 from 0.06 to 0.13 and a gradient table was created showing the location of the optimum D/L for each truss by quantifying the weight in tons per linear foot for incremental changes in depth of the same length truss for each of the 18 trusses. This effort formed a sensitivity analysis of the D/L ratio of the steel trusses to show the independent variables' effect on the dependent variable of weight (Shariat, Shariati, Madadi, & Wakil, 2018). Table 2 shows that the average optimum D/L for the trusses was 0.126, not the 0.0833 previously indicated as a rule of thumb (Ioannides & Ruddy, 2000). An assumed D/L ratio of 0.126 gives a 13.5% lighter steel truss than the previous rule-of-thumb value of 0.0833, when interpolating between Table 2 values for the nearest rounded values.

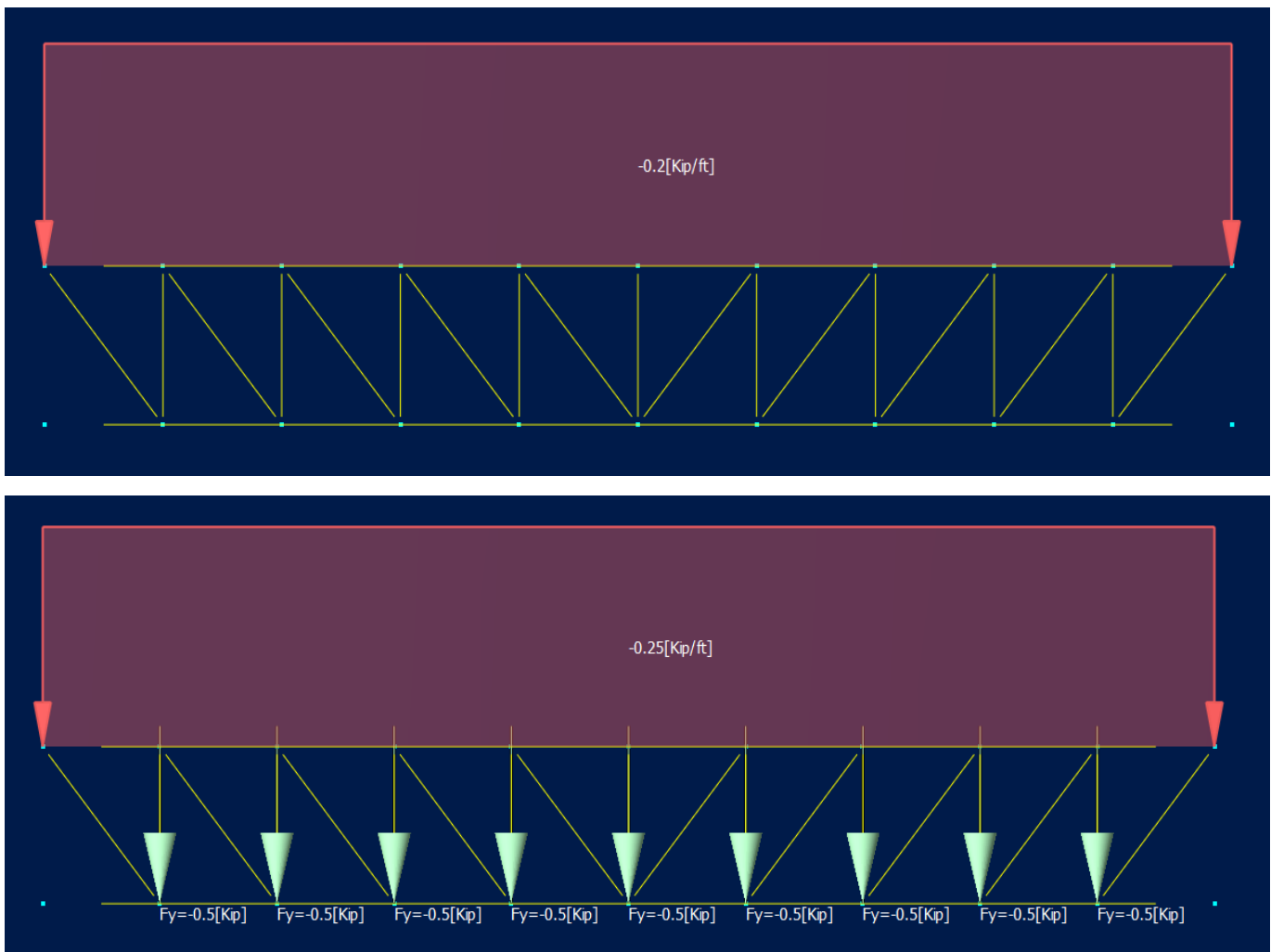


Figure 5. 100-foot truss dead load and live load.

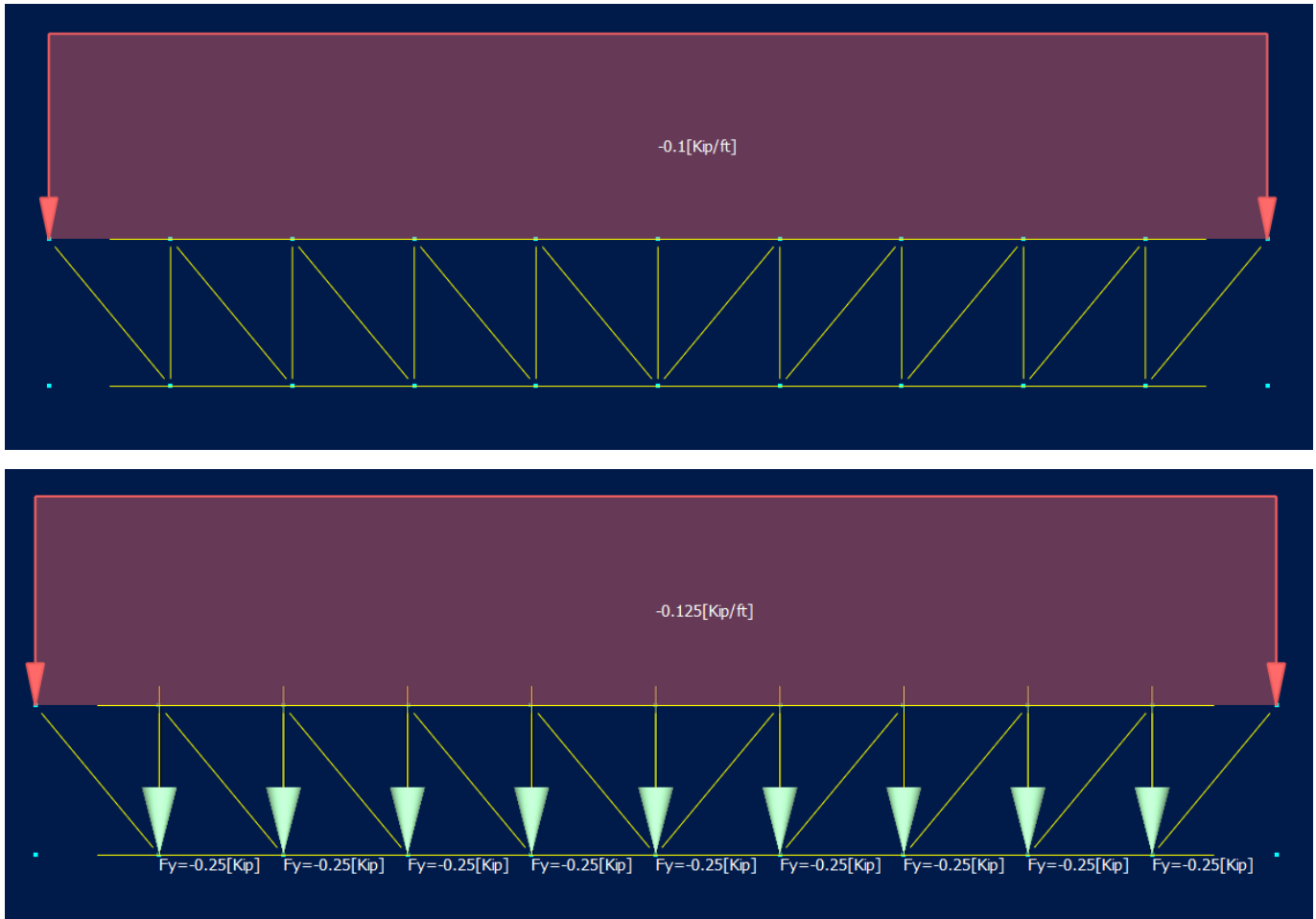


Figure 6. 50-foot truss dead load and live load.

As a third data comparison, six existing trusses previously designed were input into Equation 2 for comparison to check the accuracy of the weight approximation. It can be seen from Table 3 that, even while extrapolating slightly above the ranges of parameters used in the study, Equation 2 still provides an acceptable fit to the data with a maximum error of 26% for the existing trusses. In the third data comparison, the capability of converting unequal point loads to an equivalent moment with equal point loads for input was tested and it was found that Equation 2 was still an acceptable fit using this method.

## Summary and Conclusions

The use of genetic algorithms has been primarily focused on the optimization of parameters under a particular condition or scenario to mutate the set of varying parameters in order to optimize the desired outputs under given conditions. The limitation of genetic algorithms is the complexity and conditional parameters for individual circumstances. The use of a linear regression matrix provides a method for

optimization that is not only easier to use, understand, and communicate, but also is one equation for a vast set of potential parameters. This is one example of the potential use for such methods. The results of this study showed that linear regression fitting can be used for optimization and, in this application, produce an effective means for estimating the weight of steel trusses for use in both initial design and cost estimating. The results of this study further showed that the previously accepted rule-of-thumb method for truss weight approximation can be improved upon using Equation 2 (Ioannides & Ruddy, 2000). The potential applications of Equation 2 range from truss layout and nodal spacing optimization to improved rough estimating for facility planning. While reducing weight can benefit owners, it is important to remember that the lowest weight does not always equal the lowest cost and the impact of economies of scale in repeated design of members should be considered. However, assuming this equation is used to design for a bounded worst-case condition for a repeated truss type, it would lead to construction cost reductions independent of the economies-of-scale effect.

Table 2. Optimum depth-to-length ratios for various trusses.

L (ft.)	Truss	Type	Wt. 0.06 D/L	Wt. 0.07 D/L	Wt. 0.08 D/L	Wt. 0.09 D/L	Wt. 0.10 D/L	Wt. 0.11 D/L	Wt. 0.12 D/L	Wt. 0.13 D/L	Optimum	Δ
40	T14	Heavy	0.0455	0.0445	0.0428	0.0398	0.0400	0.0393	0.0375	0.0378	0.125	0.0080
40	T17	Light	0.0313	0.0298	0.0295	0.0283	0.0280	0.0298	0.0300	0.0303	0.095	0.0033
50	T1	Heavy	0.0712	0.0666	0.0632	0.0598	0.0578	0.0554	0.0498	0.0504	0.125	0.0214
50	T7	Light	0.0340	0.0344	0.0326	0.0312	0.0296	0.0286	0.0290	0.0294	0.110	0.0054
60	T21	Heavy	0.0902	0.0867	0.0797	0.0723	0.0648	0.0640	0.0652	0.0622	0.130	0.0280
60	T22	Light	0.0342	0.0343	0.0327	0.0330	0.0315	0.0300	0.0290	0.0293	0.125	0.0052
70	T32	Heavy	0.0920	0.0851	0.0803	0.0741	0.0707	0.0661	0.0631	0.0623	0.125	0.0297
70	T35	Light	0.0597	0.0557	0.0509	0.0476	0.0479	0.0451	0.0450	0.0457	0.120	0.0147
80	T41	Heavy	0.1333	0.1240	0.1163	0.1053	0.1048	0.0978	0.0893	0.0864	0.130	0.0469
80	T42	Light	0.0760	0.0698	0.0679	0.0616	0.0578	0.0573	0.0589	0.0563	0.130	0.0198
90	T52	Heavy	0.1364	0.1299	0.1190	0.1040	0.0977	0.0936	0.0887	0.0887	0.125	0.0478
90	T55	Light	0.0667	0.0648	0.0621	0.0548	0.0557	0.0539	0.0546	0.0488	0.130	0.0179
100	T62	Heavy	0.2518	0.2534	0.2243	0.2080	0.1970	0.1833	0.1759	0.1657	0.130	0.0861
100	T64	Light	0.1153	0.1141	0.0999	0.0920	0.0880	0.0833	0.0783	0.0802	0.125	0.0370
110	T73	Heavy	0.2544	0.2565	0.2153	0.2132	0.1847	0.1722	0.1633	0.1533	0.130	0.1011
110	T74	Light	0.1666	0.1551	0.1431	0.1226	0.1148	0.1143	0.1130	0.1043	0.130	0.0624
120	T84	Heavy	0.2009	0.2013	0.1860	0.1591	0.1487	0.1484	0.1406	0.1349	0.130	0.0660
120	T88	Light	0.1513	0.1385	0.1278	0.1186	0.1116	0.1051	0.1023	0.1002	0.130	0.0512

Table 3. Equivalent moment checks.

Truss	Length (ft.)	Depth-to-length ratio	Panel pt. spacing (ft.)	Pt. load (Kips) (LL)	Uniform load (Kip/ft.) w(DL)	Uniform load (Kip/ft.) w(LL)	Moment (Kip-ft.)	Weight (tons)	Weight (tons/LF)	Expected (tons/LF)	Δ
T1	60	0.15	10	12.3	0	1.21	1100	2.538	0.0423	0.0450	-0.0027
T2	60	0.15	10	6.8	0	0.73	634	1.87	0.0311	0.0302	0.0009
T3	60	0.15	10	6.8	0	0.93	719	2.036	0.0339	0.0330	0.0009
T4	60	0.15	10	12.3	0	1.6	1275	4.125	0.0688	0.0508	0.0180
T5	60	0.15	10	12.3	0	1.01	1010	3.192	0.0532	0.0421	0.0111
T6	60	0.15	10	12.3	0	1.89	1406	3.057	0.0510	0.0550	-0.0041

## References

- Barthelemy, J., & Hafika, R. T. (1993). Approximation Concepts for Optimum Structural Design - A Review. *Structural Optimization*, 5(3), 129-144.
- Gasparini, D. A., & Provost, C. (1989). Early Nineteenth Century Development in Truss Design in Britain, France, and the United States. *Construction History*, 5, 21-33.
- Hansen, S., & Vanderplaats, G. (1990). Approximation method for configuration optimization of trusses. *AIAA Journal*, 28(1), 161-168.
- Ioannides, S., & Ruddy, J. (2000, February) Rules of Thumb for Steel Design, *Modern Steel Construction*, 67-71.
- Salajegheh, E., & Vanderplaats, G. N. (1993). Optimum Design of Trusses with Discrete Sizing and Shape Variables. *Structural Optimization*, 6, 79-85.



- 
- Vanderplaats, G. N., & Han, S. H. (1990). Arch Shape Optimization Using Force Approximation Methods. *Structural Optimization*, 2(4), 193-201.
- Vanderplaats, G. N., Thomas, H. L., & Shyy, Y. K. (1991). A Review of Approximation Concepts for Structural Synthesis. *Computing Systems in Engineering*, 2(1), 17-25.
- Rao, S. (2019). *Engineering Optimization: Theory and Practice*. New Jersey: John Wiley & Sons, Inc.
- Shariat, M., Shariati, M., Madadi, A., & Wakil, K. (2018). Computational Lagrangian Multiplier Method Using Optimization and Sensitivity Analysis of Rectangular Reinforced Concrete Beams. *Steel and Composite Structures*, 29(2), 243-256.
- Zhaochao, L., & Yonggui, X. (2021). Buckling Mechanism of Thin-Walled Arches with Composite Polyhedral Shapes. *Composite Structures*, 271, 114134.

## Biographies

**MICHAEL C. PICKETT**, PE, received his BS from Western Kentucky University and ME from Vanderbilt University and is currently working for the Facilities Explosive Safety (FES) Mandatory Center of Expertise (MCX) as a blast engineer at the Army Corps of Engineers in Huntsville, AL. His research interests include material optimization, cost efficiency in structural design, structural health monitoring, and blast design. Mr. Pickett may be reached at [Michael.C.Pickett@usace.army.mil](mailto:Michael.C.Pickett@usace.army.mil)

**STEPHEN A. COTTON**, PE, SE, received his BS from Tennessee Tech University and MS from Virginia Tech and is currently working for the structural engineering group at Tumkey Processing Solutions, LLC in Franklin, TN. He also serves as Director of Services at BIM Consulting, LLC in Arrington, TN. His research interests include design optimization, cost efficiency in structural design, outreach to local universities for growth in building information modeling, and building information modeling with interoperability. Mr. Cotton may be reached at [bim.consulting.tn@gmail.com](mailto:bim.consulting.tn@gmail.com) or [scotton@tumkeyprocessingsolutions.com](mailto:scotton@tumkeyprocessingsolutions.com)

# SHEAR LAG IN DIAGRID TALL BUILDINGS

Mohammad T Bhuiyan, West Virginia State University

## Abstract

In a previous study, the author found that a triangulated exoskeleton, or diagrid, structural system was emerging as a structurally efficient and architecturally valid solution for tall buildings (Bhuiyan & Leon, 2018). The diagrid creates a highly efficient and redundant tube structure by providing a structural network allowing multiple load paths. The shear lag effect, which causes a nonlinear distribution of axial stresses along the building face, is important for any tube-type tall building. Tube-type structures (framed-tube, bundled-tube, etc.) were widely used for high-rise buildings. Even though the diagrid system was conceived in the 1960s, engineers started using this structural system for tall buildings only recently. Even though use of this structural system is gaining popularity, technical publications in shear lag effect for this structural system are exceedingly rare. The objective of this current study was to examine shear lag in diagrid tall buildings. Three diagrid buildings were selected for this study. Wind loads were applied to the 3D finite element models and axial stresses were calculated and plotted. The results showed a superior performance of the diagrid system with minimal shear lag.

## Introduction

Most of the structural systems initially deployed for tall buildings were steel frames with diagonal braces in various configurations (X, K, and inverted V). However, while the structural importance of diagonals was well recognized, their aesthetic potential was not explicitly appreciated. Bhuiyan (2011) wrote:

Thus, diagonals were generally embedded within the building cores, located in the interior of the building and hidden from view. A major departure from this design approach was 100-story John Hancock building in Chicago, in which diagonals were located along the entire exterior perimeter surfaces of the building in order to maximize their structural effectiveness and capitalize on the aesthetic innovation. Another expression of the structural system on the exterior of the building (exoskeleton) is the Diagrid system, one of whose earliest expressions dates back to the 1960s with the IBM Building in Pittsburgh. (p. 1)

Engineers did not give much attention to this type of structural system until recently, with the completion of the striking Re Suisse building in London and the 46-story Hearst Tower in New York (Moon, Connor & Fernandez, 2007). The diagrid creates a highly efficient and redundant tube structure by providing a structural network allowing

multiple load paths. The diagrid forms an exterior tube that can maximize the moment arm to resist overturning. The framed-tube, or braced-tube, system is used for many high-rise buildings. But, shear lag affects these systems. "It causes a nonlinear distribution of axial stresses along the building face. Usually it causes higher stresses at the corner columns than the inner columns. Shear lag reduces the structural efficiency of any tube structure" (Leonard, 2007).

## Shear Lag in Tubular Structures

The overall bending behavior of a tubular building is similar to that of a box girder, though shear deformations, which generally are neglected in box girders, play an important role in tubular buildings. The Euler-Bernoulli assumption that plane sections remain plane after bending is often used for the analysis of beam structures. According to this assumption, the longitudinal stresses in the webs and flanges should be linearly and uniformly distributed; Figure 1(a) shows an example of this. However, this assumption is appropriate and strictly applicable only when there is no shear force or when the structure has infinite shear stiffness. "In actuality, when the structure is subjected to shear forces, a shear flow develops between the web and flange panels and, owing to shear deformations of the panels, the longitudinal displacements in the parts of the webs and flanges remote from the web-flange junctions lag behind those at the junctions" (Kwan, 1996). Figure 1(b) shows how the longitudinal stress in the webs and flanges are distributed. "Such a 'shear lag' phenomenon reduces the effectiveness of the tubular structure by increasing the stresses at the web-flange junctions and reducing the axial stresses at the middle of the frame panels. The net result of the accumulation of these effects is to increase the lateral deflection of the structure" (Leonard, 2007).

Leonard (2007) went on to state the following:

More recent studies have found a phenomenon in box section opposite to the shear lag effect. Foutch and Chang, 1982 observed this anomaly in a cantilever box girder subjected to uniformly distributed load. In the region beyond one-quarter of the cantilever length from the fixed end, the bending stresses in the box section at the corners are lower than the stresses at the middle of the flange panel as shown in Figure 2. This phenomenon is called 'negative shear lag'. (p.11)

Lee, Yoo, and Yoon, 2002 attempted to explain the origin of negative shear lag. They suggested that because distributed load can be formed by superimposing distributed loads acting on the differential length, the negative shear lag that occurs in a

cantilever box girder under uniformly distributed load could also occur in a cantilever box girder under a concentrated load. They modeled a cantilever box girder subjected to a concentrated load at midspan. The analysis showed that there is no negative shear lag between the support and the point of concentrated load just as in the cantilever subjected to a concentrated load at the free end” (Leonard, 2007). However, it was found that negative shear lag occurs at the point of concentrated load ( $x = 0.5 L$ ) in Figure 3) and beyond. (p.11)

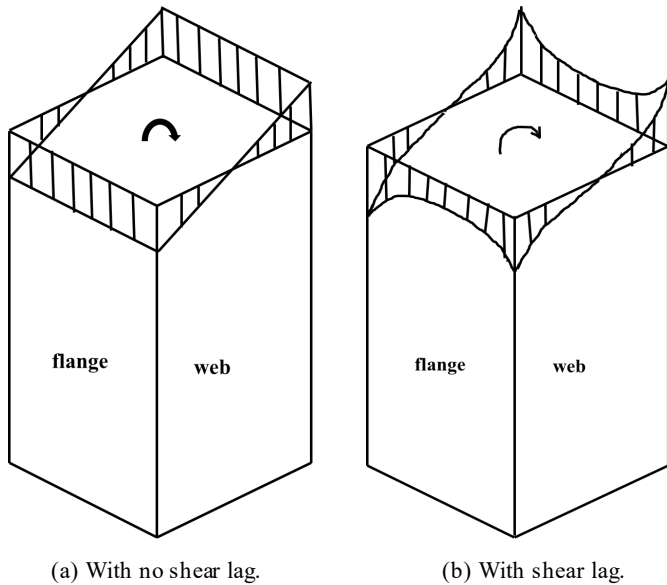


Figure 1. Axial stress distribution in tubular structures.

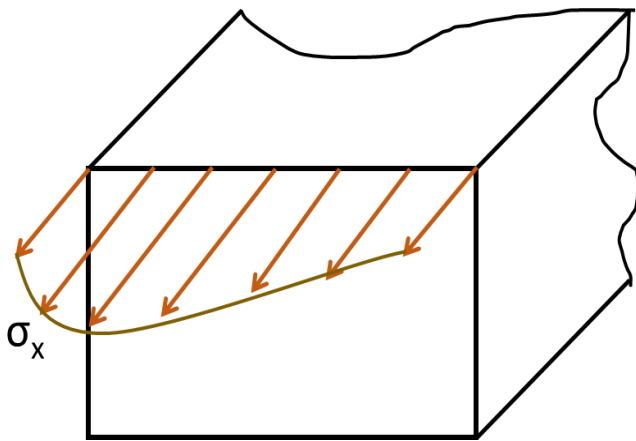


Figure 2. Negative shear lag.

According to elementary bending theory, there should be no bending stresses in the flange where the bending moment is equal to zero. Contrary to the expected result from elementary beam theory, considerable stresses developed in the flange at the location of the load, where the theoretical

bending moment was equal to zero. Figure 4 shows that the tension flange, when subjected to uniform shear flow, deformed due to positive shear lag. “Consequently, the remaining portion of the tension flange on the right side in the zero bending moment zone will necessarily deform as shown in Figure 4 in order to meet the compatibility condition at the juncture” (Leonard, 2007). Therefore, it appears that the compatibility requirement of the flange deformations at  $x = L/2$  creates stress distributions similar to negative shear lag in the zero-bending moment zone (Lee, Yoo & Yoon, 2002).

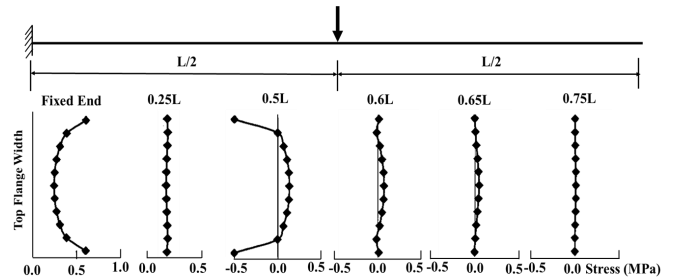


Figure 3. Top flange stresses for concentrated load at mid-span (Lee, et. al., 2002) [Reprinted with permission].

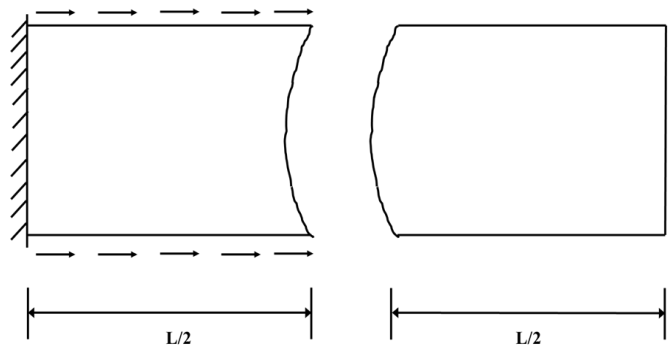


Figure 4. Deformed shape of flange (Lee, et. al., 2002) [Reprinted with permission].

Leonard (2007) studied the effect of shear lag on the diagrid system using a square-plan, sixty-story structure. He found that minor shear lag does exist in the bottom part of the diagrid building, and further observed minor negative shear lag at the top part of the building. As his study was limited to a single footprint and height diagrid building, it was necessary to study multiple diagrid tall buildings with different height and footprints in order to assess the effect of shear lag.

## Case Study Buildings

Three diagrid structures (64-, 82-, and 38-story) with different footprints and heights were selected for this current study. All of the buildings were located in a suburb of Los Angeles, California. This was a zone of high seismic ground motions and moderate winds velocities (135kph or 85 mph).

Figure 5(a) shows a 3D view of the 64-story diagrid structure. The overall plan dimensions of the building were 52 m x 35.5 m (172' x 115'), and the building height was 224 m (735'). It should be noted that gravity columns were located only around the core of the building and that there were no vertical columns (either gravity column or lateral-force resisting column) outside the building core. The wind - and earthquake-resistant system was composed of a network of diagonal elements around the building's perimeter. The floor framing was a composite system, where a 75-mm (3") concrete topping was used over a 75mm-deep (3") steel deck supported by open-web steel joists.

The second building was an 82-story building. The overall plan dimensions of the building were 48m x 48m (157' x 157'), and the building height was 287 m (942'). Figure 5(b) shows a 3D view of the diagrid structure. The floor framing was a composite system similar to the 64-story building. Similar to the other two buildings, the third build-

ing was a 38-story building for which the overall plan dimensions were 33 m x 33 m (108' x 108') with a height of 133 m (436'). Figure 5(c) shows a 3D view of the structure. A more detailed description and preliminary design of these diagrid structures can be found in the study by Bhuiyan and Leon (2018).

## Modeling and Analysis Procedures and Wind Load

Elastic 3D building models were used for all of the analyses using SAP2000 (CSI, 1997) general purpose structural engineering software. The Frame Element of SAP2000 is usually used to model beam-column behavior in planar and three-dimensional structures. Figure 6 shows how a Frame Element was used to model all of the story braces and gravity columns. Features and assumptions used in the SAP2000 models were:

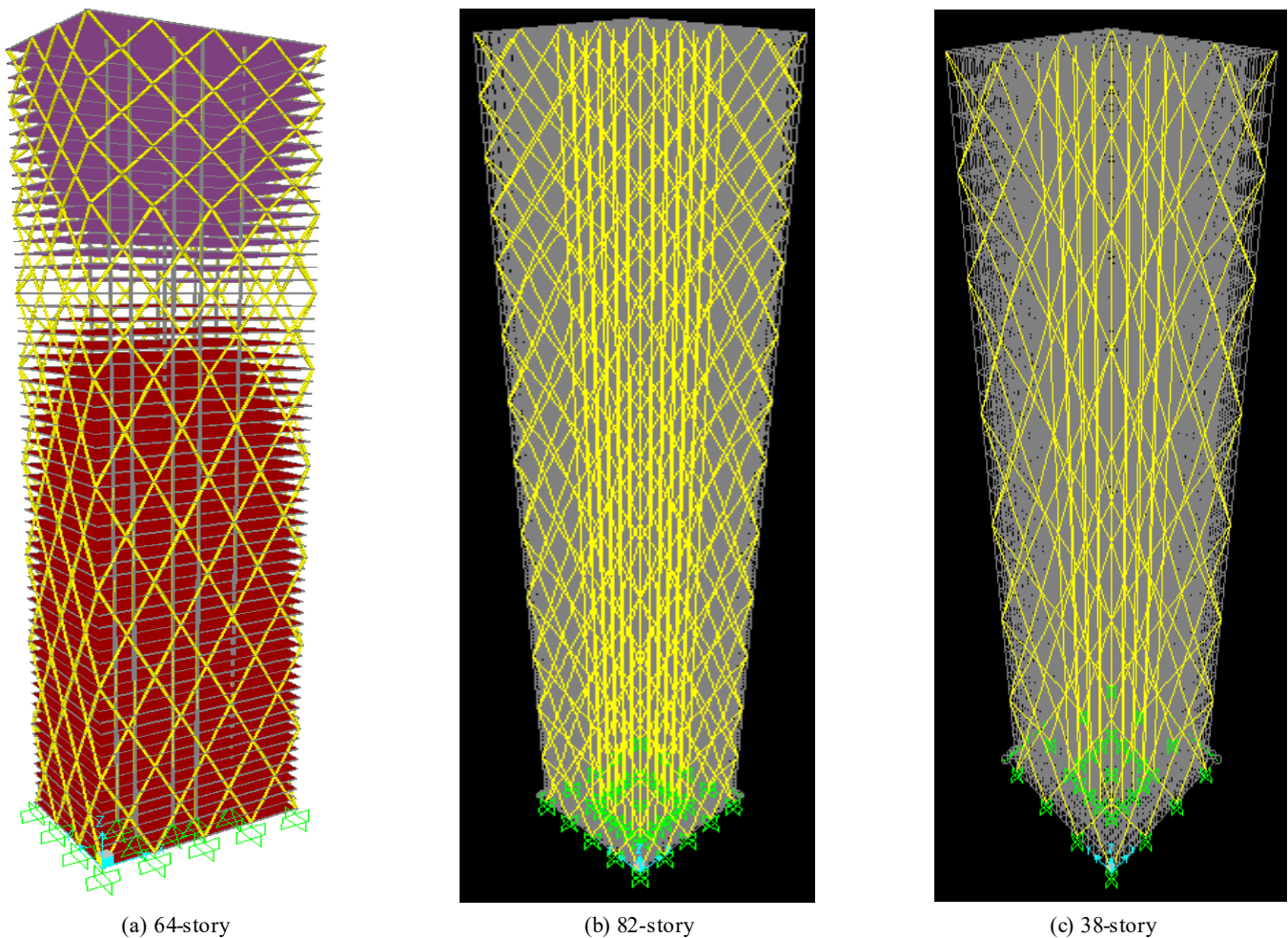


Figure 5. 3D views of the diagrid structure.

- A center-line model was established, based on the idea that diagonal braces will mostly have axial forces and, therefore, panel shear deformation will not play an important role. Even if there is some panel shear deformation, the use of a centerline length will offset this contribution.
- The connections between diagonal braces were considered as fixed.
- The foundation was modeled as rigid.
- The floor was modeled as a rigid diaphragm for all floors.
- Equivalent static wind loads (ESWL) were used for all of the three buildings in order to perform 3D static analyses.

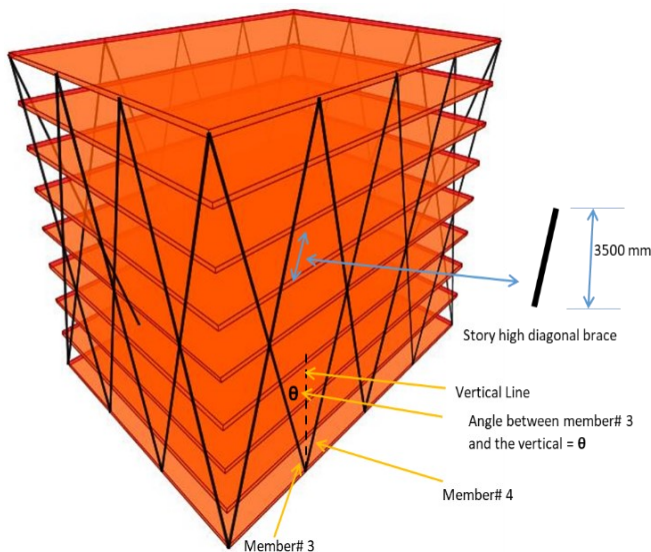


Figure 6. Story high diagonal brace.

Based on the study by Bhuiyan and Leon (2018), Table 1 presents the pipe sections used for all of the diagonals of the 64-story diagrid building. Tables 2 and 3 list the diagonal members used for 82- and 38-story buildings, respectively. Wind design of tall buildings generally does not follow a code-prescribed procedure, as this will typically result in an excessively conservative design. Typically, wind tunnel tests are used to find a more reasonable distribution of pressures for a given design (Baker, Brown & Sinn, 1998; Irwin, Breukelman, Williams & Hunter, 1998; Klemencic, Hooper & Johansson, 2008; Tingting, Wenshou & Qianjin, 2011). In this current study, wind tunnel test data were used for wind load.

The first step in this procedure was to establish a design wind speed. For that purpose, recorded wind speed data were used. To predict design speed from a set of recorded data, it was necessary to use an extreme value distribution. In this current study, the author used a Gumbel extreme value distribution to predict extreme wind velocity from a 39-year wind speed data set. Maximum annual wind speed

data sets were obtained from National Institute of Standards and Technology (NIST). After the Gumbel extreme value distribution analysis, design wind speed for a 700-year mean recurrence interval (MRI) was found to be 50.9 m/s. An MRI of 700 years was selected based on ASCE 7-22 code (ASCE, 2022).

Table 1. Member sizes for the 64-story diagrid structure.

Story	Pipe section for Long face members	Pipe section for Short face members
1 <sup>st</sup> – 8 <sup>th</sup>	750 mm dia 70 mm thickness	750 mm dia 50 mm thickness
9 <sup>th</sup> – 16 <sup>th</sup>	750 mm dia 70 mm thickness	750 mm dia 50 mm thickness
17 <sup>th</sup> – 24 <sup>th</sup>	750 mm dia 65 mm thickness	750 mm dia 50 mm thickness
25 <sup>th</sup> – 32 <sup>nd</sup>	750 mm dia 57.5 mm thickness	700 mm dia 47.5 mm thickness
33 <sup>rd</sup> – 40 <sup>th</sup>	750 mm dia 50 mm thickness	700 mm dia 40 mm thickness
41 <sup>st</sup> – 46 <sup>th</sup>	700 mm dia 45 mm thickness	650 mm dia 35 mm thickness
47 <sup>th</sup> – 52 <sup>nd</sup>	700 mm dia 45 mm thickness	650 mm dia 35 mm thickness
53 <sup>rd</sup> – 56 <sup>th</sup>	650 mm dia 40 mm thickness	600 mm dia 30 mm thickness
57 <sup>th</sup> – 60 <sup>th</sup>	650 mm dia 40 mm thickness	600 mm dia 30 mm thickness
61 <sup>st</sup> – 64 <sup>th</sup>	650 mm dia 40 mm thickness	600 mm dia 30 mm thickness

High-frequency, base-balance (HFBB) wind tunnel test data on a 6:4:24 model for urban wind conditions were obtained from the NatHaz Modeling laboratory at the University of Notre Dame (Zhou, Kijewski & Kareem, 2003). Although the prototype dimensions for the 64-story building were 52.5 m (B): 35 m (D): 224 m (H) [or 6:4:25.6 ratio], the data from NatHaz for a model 6:4:24 seemed reasonable to use. Similar test data were obtained for a 1:1:6 model (for the 82-story building) and a 1:1:4 model (for the 38-story building). Based on the procedure described in Zhou et al. (2003) and Bhuiyan (2011), equivalent static wind loads (ESWL) were calculated for all of the buildings. Table 4 shows the ESWL for the 38-story building and all of the wind load components: 1) along wind, 2) across wind, and 3) torsional components. Similar loads were calculated for the 64- and 82-story buildings. Figure 7 shows a plot of all of the story forces for all of the buildings.

Table 2. Member sizes for the 82-story diagrid structure.

Story	Pipe section	Cross-sectional area (mm <sup>2</sup> )
1 <sup>st</sup> – 8 <sup>th</sup>	800 mm dia 80 mm thickness	180955.7
9 <sup>th</sup> – 16 <sup>th</sup>	800 mm dia 80 mm thickness	180955.7
17 <sup>th</sup> – 24 <sup>th</sup>	800 mm dia 75 mm thickness	170824.1
25 <sup>th</sup> – 32 <sup>nd</sup>	750 mm dia 75 mm thickness	159043.1
33 <sup>rd</sup> – 40 <sup>th</sup>	750 mm dia 70 mm thickness	149539.8
41 <sup>st</sup> – 48 <sup>th</sup>	750 mm dia 65 mm thickness	139879.4
49 <sup>th</sup> – 54 <sup>th</sup>	750 mm dia 65 mm thickness	139879.4
55 <sup>th</sup> – 60 <sup>th</sup>	700 mm dia 60 mm thickness	120637.2
61 <sup>st</sup> – 66 <sup>th</sup>	700 mm dia 55 mm thickness	111448
67 <sup>th</sup> – 70 <sup>th</sup>	700 mm dia 55 mm thickness	111448
71 <sup>st</sup> – 74 <sup>th</sup>	650 mm dia 55 mm thickness	102808.6
75 <sup>th</sup> – 78 <sup>th</sup>	650 mm dia 50 mm thickness	94247.78
79 <sup>th</sup> – 82 <sup>nd</sup>	600 mm dia 50 mm thickness	86393.8

Table 3. Member sizes for the 38-story diagrid structure.

Story	Pipe section
1 <sup>st</sup> – 6 <sup>th</sup>	450 mm dia, 30 mm thickness
7 <sup>th</sup> – 12 <sup>th</sup>	450 mm dia, 30 mm thickness
13 <sup>th</sup> – 18 <sup>th</sup>	500 mm dia, 30 mm thickness
19 <sup>th</sup> – 24 <sup>nd</sup>	475 mm dia, 30 mm thickness
25 <sup>rd</sup> – 30 <sup>th</sup>	450 mm dia, 30 mm thickness
31 <sup>st</sup> – 34 <sup>th</sup>	425 mm dia, 25 mm thickness
35 <sup>th</sup> – 38 <sup>th</sup>	425 mm dia, 25 mm thickness

Table 4. Equivalent static wind load for the 38-story building from the HFBB wind tunnel test.

Story	Height	Along wind components	Across wind components	Torsional components
	(m)	(N)	(N)	(N-m)
38	133.0	537073	445302	3137031
37	129.5	520225	427802	3014728
36	126.0	503591	410595	2894481
35	122.5	487173	393684	2776317
34	119.0	470972	377074	2660260
33	115.5	454990	360768	2546337
32	112.0	439230	344770	2434576
31	108.5	423692	329085	2325007
30	105.0	408379	313716	2217657
29	101.5	393292	298669	2112560
28	98.0	378434	283947	2009748
27	94.5	363806	269556	1909253
26	91.0	349409	255501	1811111
25	87.5	335246	241788	1715359
24	84.0	321317	228420	1622032
23	80.5	307624	215405	1531171
22	77.0	294168	202749	1442814
21	73.5	280949	190457	1357000
20	70.0	267968	178535	1273770
19	66.5	255223	166990	1193165
18	63.0	242713	155829	1115221
17	59.5	230436	145056	1039977
16	56.0	218387	134678	967463
15	52.5	206561	124700	897707
14	49.0	194948	115127	830725
13	45.5	183537	105960	766522
12	42.0	172309	97200	705084
11	38.5	161243	88844	646370
10	35.0	150306	80884	590303
9	31.5	139457	73308	536755
8	28.0	128636	66089	485530
7	24.5	117764	59193	436331
6	21.0	106729	52561	388723
5	17.5	95367	46110	342065
4	14.0	83437	39708	295386
3	10.5	70542	33147	247135
2	7.0	55943	26045	194516
1	3.5	37840	17521	130986

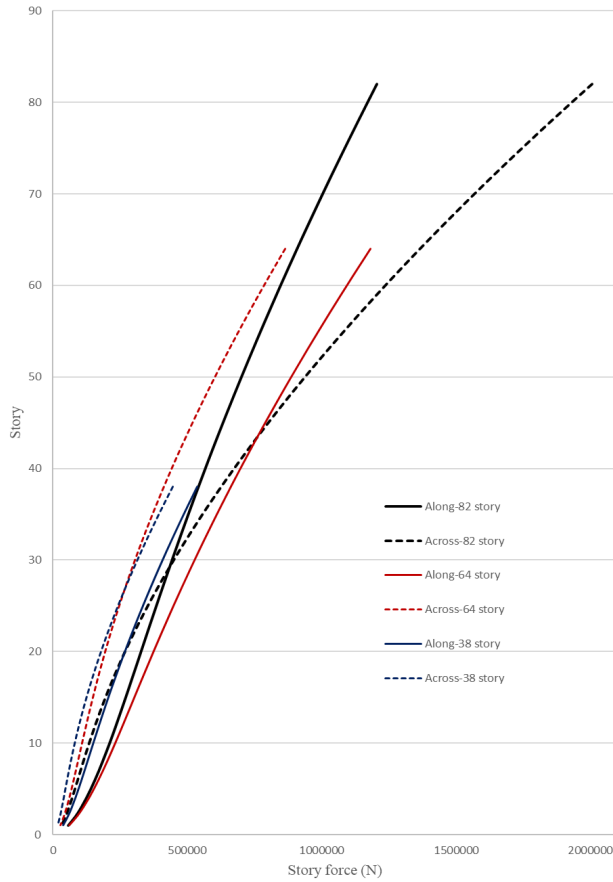


Figure 7. Story forces (wind) from the HFBB wind tunnel test.

## Results

The following is a quote by Leonard (2007).

Since diagrid structures do not have vertical elements, the shear lag effect in the bending stress distribution cannot be observed directly. To obtain the axial stresses in the longitudinal direction, the building was sectioned at the floor levels that are going to be analyzed and the vertical component of the axial stress in all diagrid elements that meet at the node of interest were summed. Care needs to be exercised when accounting for the diagrid members that meet at the corner nodes in calculating the resultant axial stress at the corner of the building. (p.25)

With the ESWL loads, elastic 3D analyses in SAP2000 were performed for all of the case study buildings. After the analyses, axial forces in each diagonal member of the buildings were extracted from SAP2000. Table 5 shows the axial forces in the diagonal members of the tension flange panel of the 82-story building. Figure 6 shows the location of member #3 and member #4—at the ground floor level and 12 m away from the corner of the building. Table 5 shows that the axial force in member #3 was 19,400,950 N and 17,200,506 N for member #4 (yellow highlighted cells). Figure 6 further shows the angle between diagonal member #3 and the vertical line as  $\theta = 23.2^\circ$ . For member #4,  $\theta$  was also  $23.2^\circ$ . Table 2 shows that the cross-sectional area of members #3 and #4 was  $180,955.7 \text{ mm}^2$ . Longitudinal axial stress at the ground floor level and 12 m away from the corner of the building was calculated as follows:

Table 5. Longitudinal axial stresses for the 82-story diagrid structure.

Tension Flange Panel - Axial Forces in "N"								
Location along the height at which Axial Stress was evaluated								
	Base (0 H)	0.1 H	0.2 H	0.29 H	0.39 H	0.49 H	0.59 H	0.66 H
0 L	23303175	19095615	16533553	14043171	11570819	9108629	6304355	5035381
0 R	19403283	12418133	9118620	6515223	4255078	2366907	1093414	765412.7
12 L	<b>19400950</b>	19451503	16907917	14090281	11320340	8577167	6885404	4677943
12 R	<b>17200506</b>	14528579	11639638	9080447	6782060	4897545	3416718	2238436
24 L	17199914	16311162	14114892	11558394	9095591	6883322	5363969	3606638
24 R	17199914	16311162	14114892	11558394	9095591	6883322	5363969	3606638
36 L	17200506	14528579	11639638	9080447	6782060	4897545	3416718	2238436
36 R	19400950	19451503	16907917	14090281	11320340	8577167	6885404	4677943
48 L	19403283	12418133	9118620	6515223	4255078	2366907	1093414	765412.7
48 R	23303175	19095615	16533553	14043171	11570819	9108629	6304355	5035381

From the Web panel

Resultant Longitudinal Stresses ( in Mpa )								
Location along the height at which Axial Stress was evaluated								
	Base (0 H)	0.1 H	0.2 H	0.29 H	0.39 H	0.49 H	0.59 H	0.66 H
0 m	217	160	138	119	97	75	49	42
12 m	<b>186</b>	173	154	134	111	89	68	50
24 m	175	166	152	134	112	90	70	52
36 m	186	173	154	134	111	89	68	50
48 m	217	160	138	119	97	75	49	42

From the Web panel

$$\text{Stress} = (\text{axial force in member \#3} + \text{axial force in member \#4}) * \cos(\theta) / (\text{cross-sectional area of the members})$$

$$= (19400950 + 17200506) * \cos(23.2^\circ) / 180955.7$$

$$= 186 \text{ MPa.}$$

Table 5 shows a stress value of 186 MPa (yellow highlighted cells). Similarly, all of the longitudinal stresses in Table 5 were calculated. Figure 8 shows a plot of these stresses along with the resultant axial stresses against the height of the building, H, on the z axis and the width of the building, B, on the x axis. Similarly, Figure 9 shows the stress distribution calculations for the web panel of the 82-story building. Now, Figures 8 and 9 can be compared with Figure 1(a), which shows the axial stress distribution for the flange and web panels with no shear lag.

Figure 8 further shows evidence of a shear lag effect, as the vertical axial stresses at the corners of the flange are higher than the middle members at the bottom part of the building (up to a height of  $z = 0.1 H$ ). A minor negative shear lag effect is evident in Figure 8 from  $z = 0.2 H$  to  $1 H$ . Figure 9 shows negligible shear lag for the web panel. Similar to the 82-structure, Table 6 shows the calculated longitudinal axial stresses for the 64-story diagrid building. Figure 10 is a plot of these stresses. In Figure 10, the resultant axial stresses were plotted against the height of the building, H, on the z axis and the width of the building, B, on the x axis. Figure 11 shows the plot of stress distribution for the web panel.

Comparing the ideal axial stress distribution for the flange panel in Figure 1(a), Figure 10 shows clear evidence of a shear lag effect, as the vertical axial stresses at the corners of the flange are higher than the middle members at the bottom part of the building (up to a height of  $z = 0.625 H$ ). The existence of negative shear lag was also evident on the top quarter of the building. Comparing the ideal axial stress distribution for web panel [see again Figure 1(a)], Figure 11 shows a negligible shear lag effect. Similar to the 82- and 64-story buildings, Figures 12 and 13 depict the longitudinal stress distribution for flange and web panels, respectively. Closer inspection of these figures indicated that shear lag effects were minor.

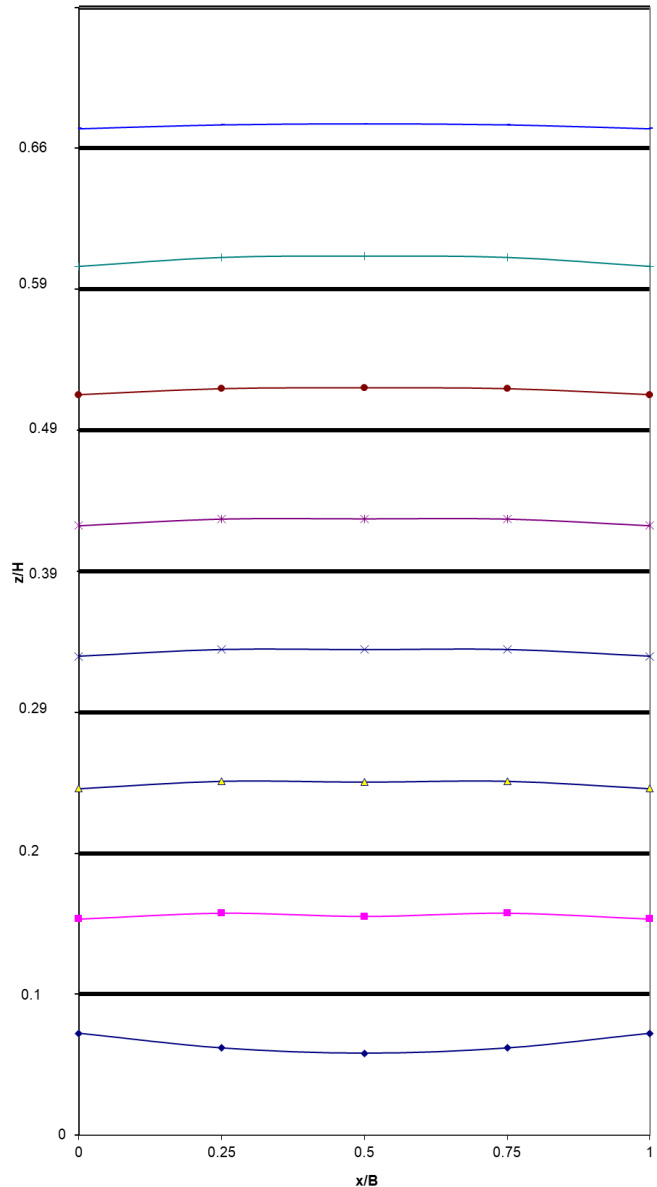


Figure 8. Axial stress distribution in the flange panel for the 82-story structure.

Table 6. Longitudinal axial stresses for the 64-story diagrid structure.

Tension Flange Panel: Resultant Longitudinal Stresses (in Mpa)

Along width		Location along the height at which Axial Stress was evaluated							
		Base (0 H)	0.125 H	0.25 H	0.375 H	0.5 H	0.625 H	0.72 H	0.81 H
0	0 m	181	136	114	92	70	47	37	3
0.25	13.12 m	126	111	85	60	39	22	65	20
0.5	26.24 m	113	104	82	59	38	22	67	23
0.75	39.36 m	126	111	85	60	39	22	65	20
1	52.48 m	181	136	114	92	70	47	37	3



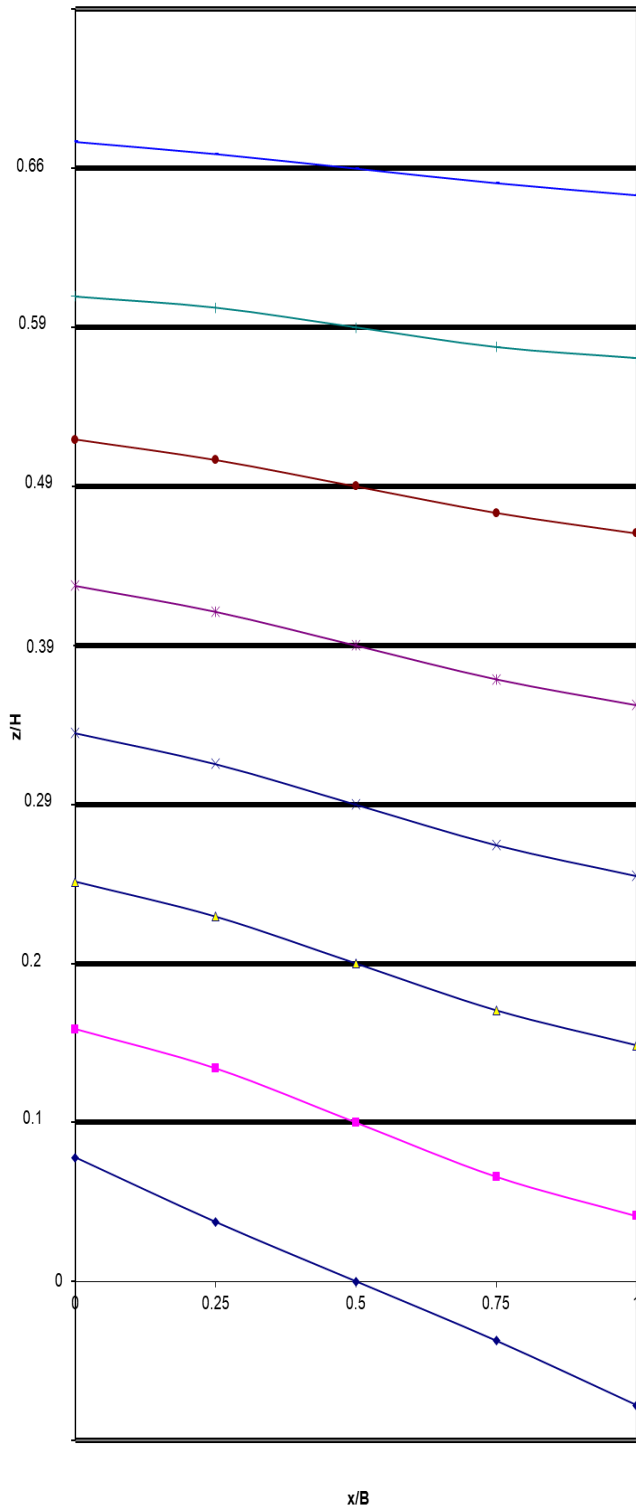


Figure 9. Axial stress distribution in the web panel for the 82-story structure.

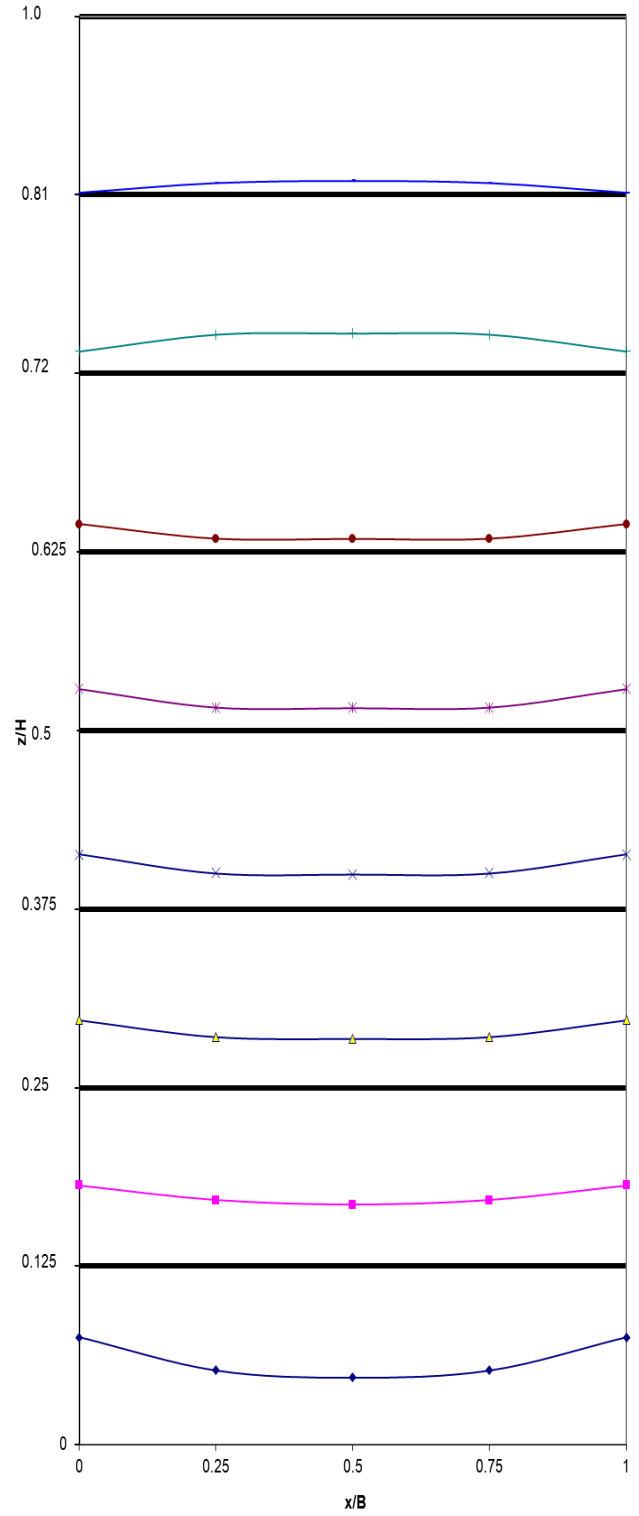


Figure 10. Axial stress distribution in the flange panel for the 64-story structure.

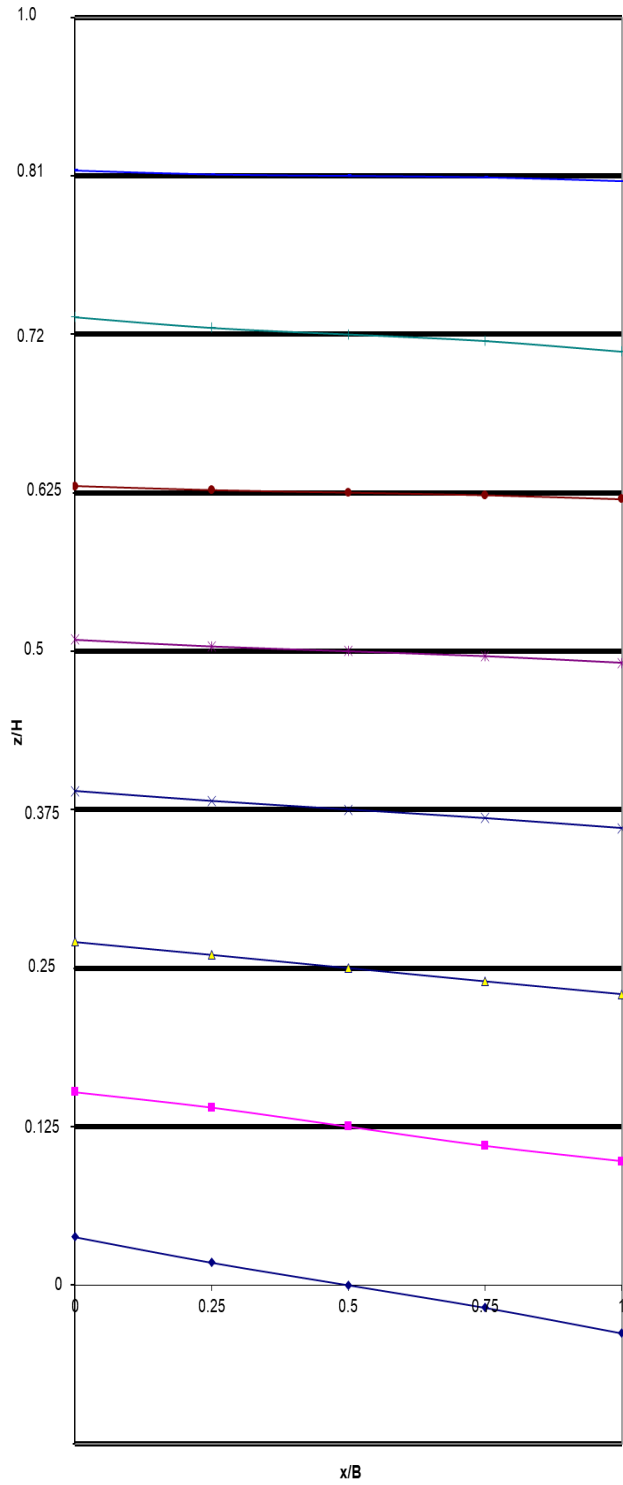


Figure 11. Axial stress distribution in the web panel for the 64-story structure.

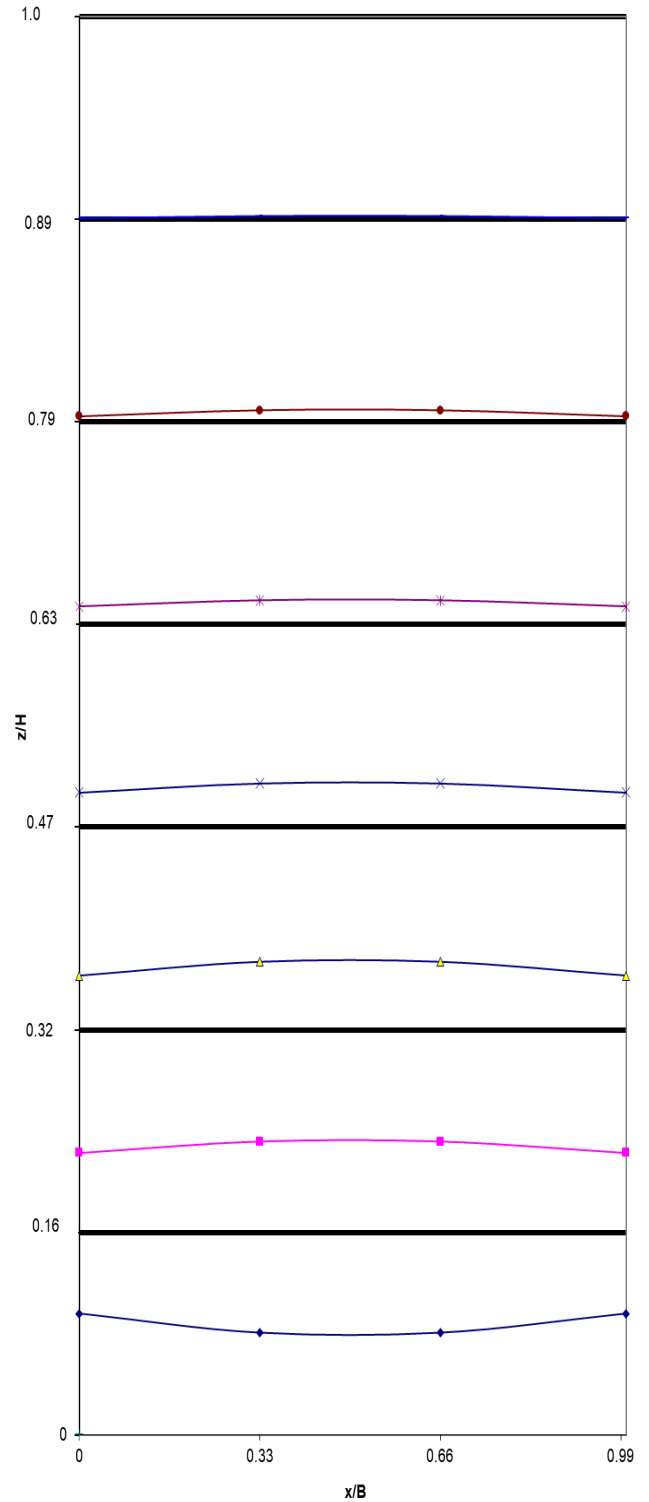


Figure 12. Axial stress distribution in the flange panel for the 38-story structure.

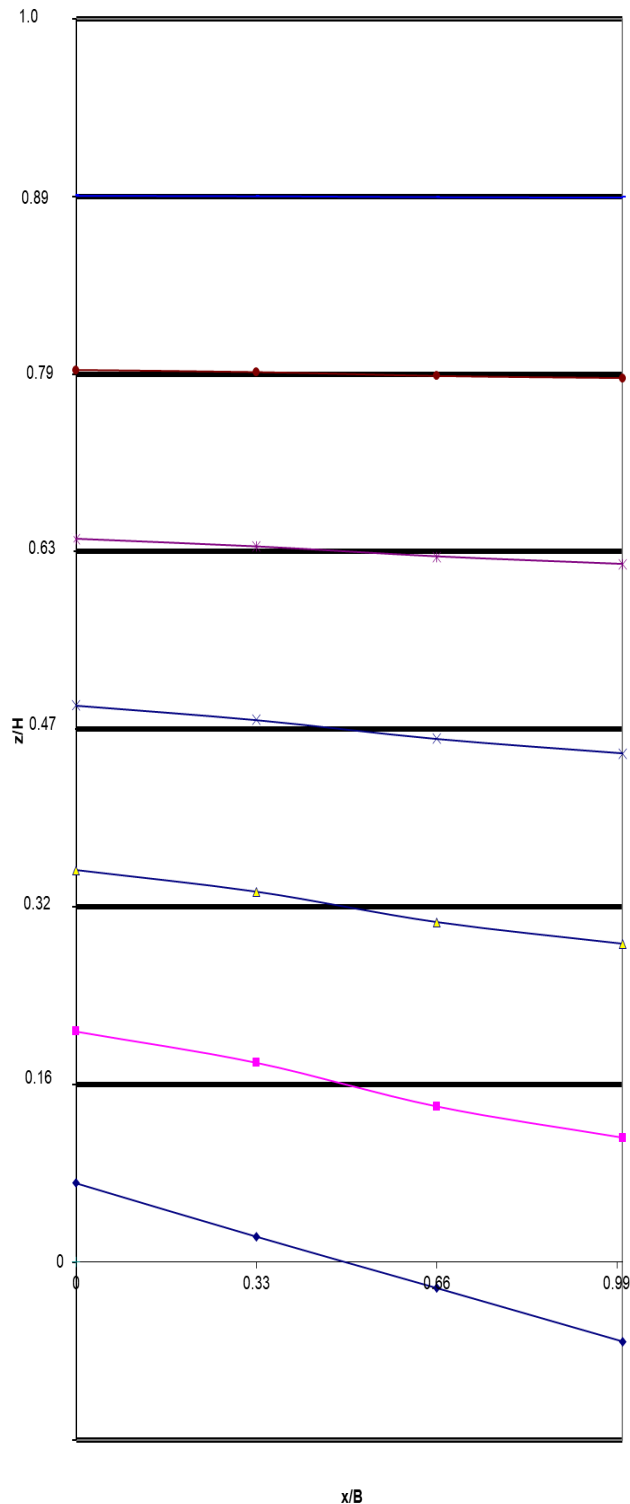


Figure 13. Axial stress distribution in the web panel for the 38-story structure.

## Conclusions

Three selected case study buildings were analyzed using SAP2000 to determine the effect of shear lag in diagrid tall buildings. Shear lag is one of the measures for evaluating the efficiency of tubular structures. For buildings with rectangular floor plans (for example, a 64-story building with a 52 m x 35.5 m floor plan), results showed evidence of shear lag in the lower floors of the structure and negative shear lag on the top quarter of the building. For square floor plan buildings (for example, 82- and 38-story buildings), results showed minor evidence of shear lag in the lower floors of the structures up to a height of approximately  $z = 0.1 H$ . Overall, the shear lag effects were minor, and thus confirmed the general notion of higher structural efficiency for diagrid structures over conventional tube buildings. To get a complete picture of the shear lag effect on diagrid structure, more studies are necessary with different width, depth, and height (W:D:H) ratios. For example, diagrid buildings with W:D:H ratios of 1:2:4, 1:2:5, 1:2:6, 1:1.5:4, 1:1.5:5, 1:1:5, etc. need to be analyzed in order to determine the extent of the shear lag effect.

## References

- ASCE (American Society of Civil Engineers). (2022). *ASCE 7-22: Minimum Design Loads for Buildings and Other Structures*. American Society of Civil Engineers, Reston, VA.
- Baker, W., Brown, C., & Sinn, R. (1998, July). *Belt wall/core interacting system for 77-story plaza Rakyat tower*. Paper presented at the Structural Engineering World Congress, San Francisco, CA, USA.
- Bhuiyan, M., & Leon, R. (2018). Preliminary Design of a Diagrid Tall Buildings. *International Journal of Modern Engineering*, 18(1), 5-14.
- Bhuiyan, M. (2011). *Response of Diagrid Tall Building to Wind and Earthquake Actions* (Unpublished doctoral dissertation). ROSE School, University of Pavia, Pavia, Italy.
- Computers and Structures, Inc. (1997). SAP2000 – Integrated Structural Analysis & Design Software [Computer software]. Computers and Structures, Inc., Berkeley, California.
- Foutch, D., & Chang, P. (1982). A Shear lag anomaly. *Journal of Structural Engineering*, 108(7), 1653-1658.
- Irwin, P., Breukelman, B., Williams, C., & Hunter, H. (1998, July). *Shaping and Orienting Tall buildings for Wind*. Paper presented at the Structural Engineering World Congress, San Francisco, CA, USA.
- Klemencic, R., Hooper, J., & Johansson, O. (2008, April). *One Rincon Hill: Raising the Bar*. Paper presented at the Structures Congress 2008: Crossing Borders, Vancouver, BC, Canada.
- Kwan, A. K. H. (1996). Shear Lag in Shear/Core Walls, *Journal of Structural Engineering*, 122(9), 1097-1104.

- 
- Lee, S., Yoo, C., & Yoon, D. (2002). Analysis of Shear Lag Anomaly in Box Girders. *Journal of Structural Engineering*, 128(11), 1379-1386.
- Leonard, J. (2007). *Investigation of Shear Lag Effect in High-rise Buildings with Diagrid System* (Unpublished master's thesis). Massachusetts Institute of Technology, Cambridge, MA.
- Moon, K., Connor, J., & Fernandez, J. (2007). Diagrid Structural systems for tall buildings: Characteristics and methodology for preliminary design. *The Structural Design of Tall and Special Buildings*, 16, 205-230.
- Tingting, L., Wenshou, Z., & Qianjin, Y. (2011). A study on vortex-induced vibration of supertall buildings in a crosswind. *The Structural Design of Tall and Special Buildings*, 20(8), 902-910.
- Zhou, Y., Kijewski, T., & Kareem, A. (2003). Aerodynamic Loads on Tall Buildings: Interactive Database. *Journal of Structural Engineering*, 129(3), 394-404.

## Biographies

**MOHAMMAD T. BHUIYAN** is an Associate Professor of Civil Engineering at West Virginia State University. He earned his BSc in Civil Engineering from Bangladesh University of Engineering and Technology, Dhaka; MSc in Earthquake Engineering jointly from Universite Joseph Fourier, France, and ROSE School, Italy; and, PhD in Earthquake Engineering from ROSE School with a joint program at Georgia Tech. His research interests include tall buildings, earthquake engineering, and soil-structure interaction. Dr. Bhuiyan may be reached at [towhid@wvstateu.edu](mailto:towhid@wvstateu.edu)

# INSTRUCTIONS FOR AUTHORS: MANUSCRIPT FORMATTING REQUIREMENTS

The INTERNATIONAL JOURNAL OF MODERN ENGINEERING is an online/print publication designed for Engineering, Engineering Technology, and Industrial Technology professionals. All submissions to this journal, submission of manuscripts, peer-reviews of submitted documents, requested editing changes, notification of acceptance or rejection, and final publication of accepted manuscripts will be handled electronically. The only exception is the submission of separate high-quality image files that are too large to send electronically.

All manuscript submissions must be prepared in Microsoft Word (.doc or .docx) and contain all figures, images and/or pictures embedded where you want them and appropriately captioned. Also included here is a summary of the formatting instructions. You should, however, review the [sample Word document](http://ijme.us/formatting_guidelines/) on our website ([http://ijme.us/formatting\\_guidelines/](http://ijme.us/formatting_guidelines/)) for details on how to correctly format your manuscript. The editorial staff reserves the right to edit and reformat any submitted document in order to meet publication standards of the journal.

The references included in the References section of your manuscript must follow APA-formatting guidelines. In order to help you, the sample Word document also includes numerous examples of how to format a variety of scenarios. Keep in mind that an incorrectly formatted manuscript will be returned to you, a delay that may cause it (if accepted) to be moved to a subsequent issue of the journal.

1. **Word Document Page Setup:** Two columns with 1/4" spacing between columns; top of page = 3/4"; bottom of page = 1" (from the top of the footer to bottom of page); left margin = 3/4"; right margin = 3/4".
2. **Paper Title:** Centered at the top of the first page with a 22-point Times New Roman (Bold), small-caps font.
3. **Page Breaks:** Do not use page breaks.
4. **Figures, Tables, and Equations:** All figures, tables, and equations must be placed immediately after the first paragraph in which they are introduced. And, each must be introduced. For example: "Figure 1 shows the operation of supercapacitors." "The speed of light can be determined using Equation 4:"

5. **More on Tables and Figures:** Center table captions above each table; center figure captions below each figure. Use 9-point Times New Roman (TNR) font. Italicize the words for table and figure, as well as their respective numbers; the remaining information in the caption is not italicized and followed by a period—e.g., "*Table 1.* Number of research universities in the state." or "*Figure 5.* Cross-sectional aerial map of the forested area."
6. **Figures with Multiple Images:** If any given figure includes multiple images, do NOT group them; they must be placed individually and have individual minor captions using, "(a)" "(b)" etc. Again, use 9-point TNR.
7. **Equations:** Each equation must be numbered, placed in numerical order within the document, and introduced—as noted in item #4.
8. **Tables, Graphs, and Flowcharts:** All tables, graphs, and flowcharts must be created directly in Word; tables must be enclosed on all sides. The use of color and/or highlighting is acceptable and encouraged, if it provides clarity for the reader.
9. **Textboxes:** Do not use text boxes anywhere in the document. For example, table/figure captions must be regular text and not attached in any way to their tables or images.
10. **Body Fonts:** Use 10-point TNR for body text throughout (1/8" paragraph indentation); indent all new paragraphs as per the images shown below; do not use tabs anywhere in the document; 9-point TNR for author names/affiliations under the paper title; 16-point TNR for major section titles; 14-point TNR for minor section titles.



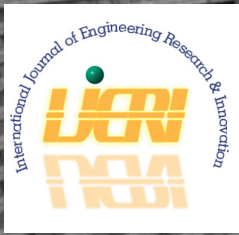
11. **Personal Pronouns:** Do not use personal pronouns (e.g., "we" "our" etc.).
12. **Section Numbering:** Do not use section numbering of any kind.
13. **Headers and Footers:** Do not use either.

- 
14. **References in the Abstract:** Do NOT include any references in the Abstract.
  15. **In-Text Referencing:** For the first occurrence of a given reference, list all authors—last names only—up to seven (7); if more than seven, use “et al.” after the seventh author. For a second citation of the same reference—assuming that it has three or more authors—add “et al.” after the third author. Again, see the *sample Word document* and the *formatting guide for references* for specifics.
  16. **More on In-Text References:** If you include a reference on any table, figure, or equation that was not created or originally published by one or more authors on your manuscript, you may not republish it without the expressed, written consent of the publishing author(s). The same holds true for name-brand products.
  17. **End-of-Document References Section:** List all references in alphabetical order using the last name of the first author—last name first, followed by a comma and the author’s initials. Do not use retrieval dates for websites.
  18. **Author Biographies:** Include biographies and current email addresses for each author at the end of the document.
  19. **Page Limit:** Manuscripts should not be more than 15 pages (single-spaced, 2-column format, 10-point TNR font).
  20. **Page Numbering:** Do not use page numbers.
  21. **Publication Charges:** Manuscripts accepted for publication are subject to mandatory publication charges.
  22. **Copyright Agreement:** A copyright transfer agreement form must be signed by all authors on a given manuscript and submitted by the corresponding author before that manuscript will be published. Two versions of the form will be sent with your manuscript’s acceptance email.
  23. **Submissions:** All manuscripts and required files and forms must be submitted electronically to Dr. Philip D. Weinsier, manuscript editor, at [philipw@bgsu.edu](mailto:philipw@bgsu.edu).
  24. **Published Deadlines:** Manuscripts may be submitted at any time during the year, irrespective of published deadlines, and the editor will automatically have your manuscript reviewed for the next-available issue of the journal. Published deadlines are intended as “target” dates for submitting new manuscripts as well as revised documents. Assuming that all other submission conditions have been met, and that there is space available in the associated issue, your manuscript will be published in that issue if the submission process—including payment of publication fees—has been completed by the posted deadline for that issue.

Missing a deadline generally only means that your manuscript may be held for a subsequent issue of the journal. However, conditions exist under which a given manuscript may be rejected. Always check with the editor to be sure. Also, if you do not complete the submission process (including all required revisions) within 12 months of the original submission of your manuscript, your manuscript may be rejected or it may have to begin the entire review process anew.

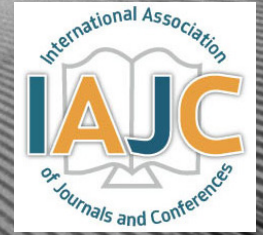
Only one form is required. Do not submit both forms!

The form named “paper” must be hand-signed by each author. The other form, “electronic,” does not require hand signatures and may be filled out by the corresponding author, as long as he/she receives written permission from all authors to have him/her sign on their behalf.



[www.ijeri.org](http://www.ijeri.org)

Print ISSN: 2152-4157  
Online ISSN: 2152-4165



[www.iajc.org](http://www.iajc.org)

## INTERNATIONAL JOURNAL OF ENGINEERING RESEARCH AND INNOVATION

### **ABOUT IJERI:**

- IJERI is the second official journal of the International Association of Journals and Conferences (IAJC).
- IJERI is a high-quality, independent journal steered by a distinguished board of directors and supported by an international review board representing many well-known universities, colleges, and corporations in the U.S. and abroad.
- IJERI has an impact factor of **1.58**, placing it among an elite group of most-cited engineering journals worldwide.

### **OTHER IAJC JOURNALS:**

- The International Journal of Modern Engineering (IJME)  
For more information visit [www.ijme.us](http://www.ijme.us)
- The Technology Interface International Journal (TIIJ)  
For more information visit [www.tiij.org](http://www.tiij.org)

### **IJERI SUBMISSIONS:**

- Manuscripts should be sent electronically to the manuscript editor, Dr. Philip Weinsier, at [philipw@bgsu.edu](mailto:philipw@bgsu.edu).

For submission guidelines visit  
[www.ijeri.org/submissions](http://www.ijeri.org/submissions)

### **TO JOIN THE REVIEW BOARD:**

- Contact the chair of the International Review Board, Dr. Philip Weinsier, at [philipw@bgsu.edu](mailto:philipw@bgsu.edu).

For more information visit  
[www.ijeri.org/editorial](http://www.ijeri.org/editorial)

### **INDEXING ORGANIZATIONS:**

- IJERI is currently indexed by 16 agencies. For a complete listing, please visit us at [www.ijeri.org](http://www.ijeri.org).

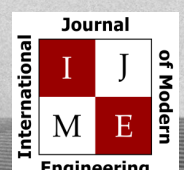
### **Contact us:**

**Mark Rajai, Ph.D.**

Editor-in-Chief  
California State University-Northridge  
College of Engineering and Computer Science  
Room: JD 4510  
Northridge, CA 91330  
Office: (818) 677-5003  
Email: [mrajai@csun.edu](mailto:mrajai@csun.edu)



[www.tiij.org](http://www.tiij.org)



[www.ijme.us](http://www.ijme.us)

# THE LEADING JOURNAL OF ENGINEERING, APPLIED SCIENCE AND TECHNOLOGY

**The latest impact factor (IF) calculation (Google Scholar method) for IJME of 3.0 moves it even higher in its march towards the top 10 engineering journals.**

**IJME IS THE OFFICAL AND FLAGSHIP JOURNAL OF THE  
INTERNATIONAL ASSOCIATION OF JOURNALS AND CONFERENCE (IAJC)**

[www.iajc.org](http://www.iajc.org)



The International Journal of Modern Engineering (IJME) is a highly-selective, peer-reviewed journal covering topics that appeal to a broad readership of various branches of engineering and related technologies. IJME is steered by the IAJC distinguished board of directors and is supported by an international review board consisting of prominent individuals representing many well-known universities, colleges, and corporations in the United States and abroad.

## **IJME Contact Information**

**General questions or inquiries about sponsorship of the journal should be directed to:**

**Mark Rajai, Ph.D.**

**Editor-in-Chief**

**Office: (818) 677-5003**

**Email: [editor@ijme.us](mailto:editor@ijme.us)**

**Department of Manufacturing Systems Engineering & Management**

**California State University-Northridge**

**1811 Nordhoff St.**

**Northridge, CA 91330**